Nucleotide-Dependent Preferential Localization of Ras in Model Membranes with Lipid Raft Nanodomains

Anna Shishina
Marquette University

NUCLEOTIDE-DEPENDENT PREFERENTIAL LOCALIZATION OF RAS IN MODEL MEMBRANES WITH LIPID RAFT NANODOMAINS

by

Anna Shishina, B.Sc., M.Sc.

A Dissertation submitted to the Faculty of the Graduate School,
Marquette University,
in Partial Fulfillment of the Requirements for
the Degree of Doctor of Philosophy

Milwaukee, Wisconsin

December 2017

ABSTRACT

NUCLEOTIDE-DEPENDENT PREFERENTIAL LOCALIZATION OF RAS IN MODEL MEMBRANES WITH LIPID RAFT NANODOMAINS

Anna Shishina, B.Sc., M.Sc.

Marquette University, December 2017

Membrane proteins constitute a third of all proteins in the cell and more than 50% of drug targets. However, the analysis of membrane proteins has many challenges owing to their partially hydrophobic surfaces, flexibility and lack of stability.

One example of an essential membrane protein is Ras superfamily. Ras is a small monomeric GTPase involved in regulation of cell growth, proliferation and differentiation. Therefore, Ras and its effectors are among the most important targets for cancer therapy. A detailed knowledge of the processes occurring during signal propagation via Ras might help to elucidate the mechanisms of the involved signal cascades.

The preparation of lipid-modified Ras proteins and their study in the presence of the lipid membrane mimic is the subject of this work. Here we investigate the Ras interaction with lipids in isolation from a possible modulation by other cellular membrane proteins. In our study we focus on a property of Ras that it does not act as an ordinary membrane protein, which stays anchored at the same lipid domain throughout its lifetime. Instead, Ras is capable of moving between raft and disordered lipid domains during its functional cycle.

It is suggested that Ras binds to some membrane proteins, and thus changes its localization. We have demonstrated that Ras molecule directly recognizes lipid domains, and its binding affinity depends on the activation state of Ras. The results of this work contribute to the further elucidation of the mechanisms of tumorogenesis and may provide new starting points for further developments in cancer therapy.

ACKNOWLEDGMENTS

Anna Shishina, B.Sc., M.Sc.

First of all, I would like to thank Dr. Evgueni Kovrigin for having accepted me in his group as a PhD student. These 5 years were a great and unforgettable journey for me. I would like to thank Dr. Kovrigin for his lessons of science, critical thinking, motivation and support. Working under his supervision was greatly valued experience for me.

Second, I thank my committee members Dr. Rajendra Rathore, Dr. James Kincaid and Dr. James Gardinier for their guidance and support during this project. I deeply appreciate the fact Dr. Rathore allowed me to work in his group and I was able to learn a lot from him. I would also like to thank Professor Yuri Sebyakin, my B.Sc and M.Sc. adviser, for motivating me to work in the field of biological membranes and pursue doctoral studies.

I would like to thank my current group members Azamat and Sara for helpful discussions and support. Special thanks go to Liza, who guided me through the mutagenesis and protein expression experiments, I was so grateful to learn from her.

I want to acknowledge all the Professors in the Chemistry and Biology departments who contributed to my academic progress at Marquette University. Also thanks to Dr. Sheng Cai and Mark Bartelt for the technical support, and Lori Callaghan and Paul Dion for administrative work and management. I would also like to extend my thanks to the whole Marquette community for the welcoming and warm atmosphere here.

I would also like to thank the Arthur J. Schmitt Foundation for the financial support and motivation. This scholarship gave me an opportunity to focus on my project and to meet many bright and inspirational people.

Biggest thank you to my parents for giving me the opportunity to obtain a university degree, entering the field of science and providing the necessary love and support.

TABLE OF CONTENTS

LIST OF TABLES

LIST OF SCHEMES

LIST OF FIGURES

1. Introduction

1.1 Ras Superfamily Proteins

Among variety of biomolecules, proteins play a crucial role performing a number of vital cellular functions including: enzymatic catalysis, structural scaffolding, signaling and transport.

Ras superfamily was first described more than forty years ago and recognized as oncogenic protein in rats (*1*). Currently, Ras is one of key targets for cancer treatment being responsible for 20-30% of human cancers while being a sole cancer driver for particular cancer types. For example, pancreatic cancer cells have 90% of mutated Ras genes (*2*).

Ras studies started with observation that certain sarcoma retroviruses cause tumors formation in rats. In two types of retroviruses, Harvey and Kirsten discovered the genes for the corresponding oncoproteins: *H*-Ras (Harvey) and *K*-Ras (Kirsten). *N*-Ras (neuroblastoma) was discovered in 1983 in human neuroblastoma cells (*3*). By the sequence homology Ras proteins belong to the so-called small G-proteins family, which is a sub-class of G-proteins (*4*). The Ras superfamily is the most examined and it is divided into six subfamilies: Ras, Rab, Ran, Rho, Rad und Arf families (Figure 1-1).

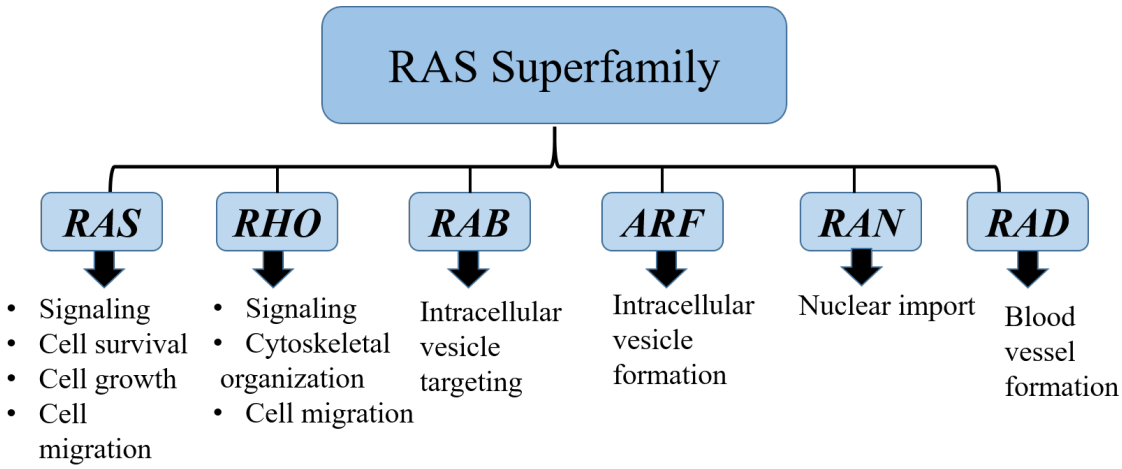

Figure 1-1 Ras superfamily of GTP-binding proteins with their functions

Small G-proteins act as regulators in all important biological functions, such as transmembrane signal transduction (Ras), cytoskeleton organization (Rho), gene expression (Ras, Rho), intracellular vesicle transport (Rab, Arf) and microtubule organization (Ran) (*5*). Because of the cancer relevance, we focused this study on Ras to advance understanding the Ras signaling and protein-lipid interactions.

1.1.1 Ras Structure

Proteins in Ras family share a common structural organization. The *N*-terminal G domain (c.a. 166 amino acids) binds guanosine nucleotides and has size about 20 kDa. It contains a six-stranded beta sheets and five alpha helices (Figure 1-2). The *N*-terminal G domain is linked with an unstructured *C*-terminal hypervariable region, HVR, usually consisted of 22-23 amino acids.

The G domain is responsible for nucleotide binding and contains five G motifs:

- G1 motif or P-loop that binds the beta phosphate of GDP and GTP;
- G2 motif or Switch I, including the Threonine-35 that binds the terminal phosphate of GTP and the divalent magnesium ion in the active site. T35 makes no contacts with GDP;
- G3 motif or Switch II, including the Aspartate-57 and Glutamine-61 residues that activate a catalytic water molecule for hydrolysis of GTP to GDP;
- G4 motif providing specific interaction with the guanine base;
- G5 motif including alanine-146, which is specific for guanine (rather than adenine) recognition (*6*).

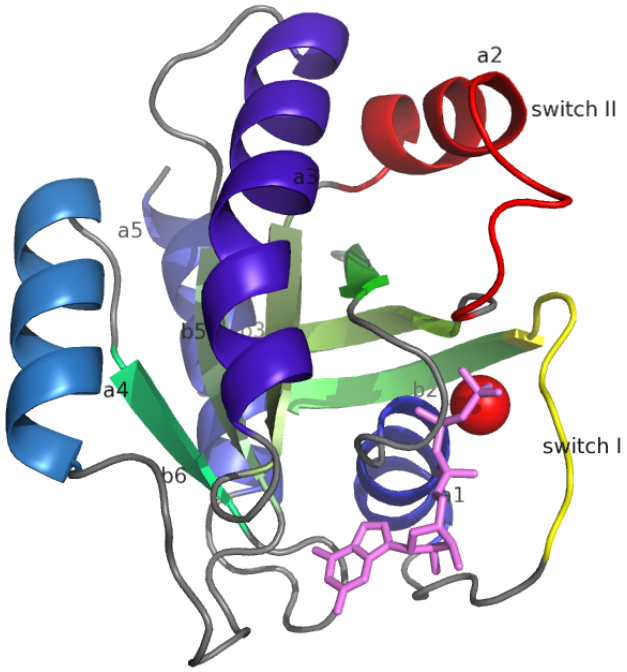

Figure 1-2 Schematic representation of Ras GTPase. *H*-Ras G-domain is 166 amino acids long with six beta sheets (b1-b6) and five helices (a1-a5). The GTP*Mg^{2+} ligand represented as magenta sticks and a red sphere, respectively

The switch motifs (G2 and G3) are flexible and undergo conformational change upon activation by GTP. This change in the conformation leads to differential affinity to effectors and constitutes the basic functionality of Ras as a molecular switch.

1.1.2 Molecular Switch

While the hydrolysis of ATP is used as an energy source for metabolic processes in the cells, GTP appears to be the primary molecule for the regulation of guanine nucleotide binding proteins (GNBP) including Ras. A universal feature of all GNBP proteins is the presence of two different conformational states: the active GTP-bound state and inactive GDP-bound state. Therefore, the GNBPs are often described as molecular switches (Figure 1-3).

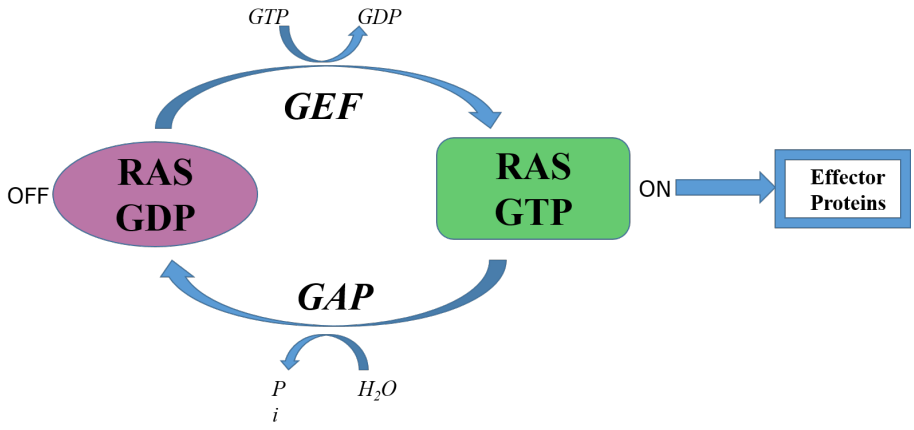

Figure 1-3 Ras conformational switch between active and inactive states is driven by the action of GAP and GEF factors

An extracellular signal activates GEF that stimulates the dissociation of GDP from the GDP-bound Ras and binding of GTP, leading to the conformational change of the switches (effector binding region). The effector-binding affinity of this region

increases ~100 fold, effectors are bound and activated, which propagates extracellular signal into the cell.

The signaling cascade is shut down when the Ras-GTP is converted to Ras GDP by the action of the GTPase activating protein (GAP). Thus, one cycle of activation and inactivation achieved. The rate-limiting step of the GDP/GTP exchange reaction is the dissociation of GDP from the GDP-bound form. This reaction is extremely slow and therefore stimulated by a regulator, named GEF (guanine nucleotide exchange factor). GTP cleavage is also intrinsically slow and accelerated by proteins (*7*).

The oncogenic mutations in Ras interrupt the cycle by the GAP-induced GTPase activation (*8*). Thus, unlike normal Ras, mutant proteins remain constitutively in the active GTP-bound form and continuously transmit signals, which ultimately lead to uncontrolled cellular growth and division.

1.1.3 Post-Translational Modification

Post-translational modification refers to the further processing of protein after the ribosomal synthesis as a way to develop the biologically active state. Examples of modifications are glycosylation, lipidation, acetylation, methylation, hydroxylation, and phosphorylation (*9*).

Each type of modification gives proteins distinct membrane properties. In particular, affinities, lipidation increases the hydrophobicity of a protein and endows it with affinity for membranes. An example of lipid-modified, membrane-anchored proteins are the Ras GTPase.

S-isoprenylation (Far, GerGer) n=1, 2

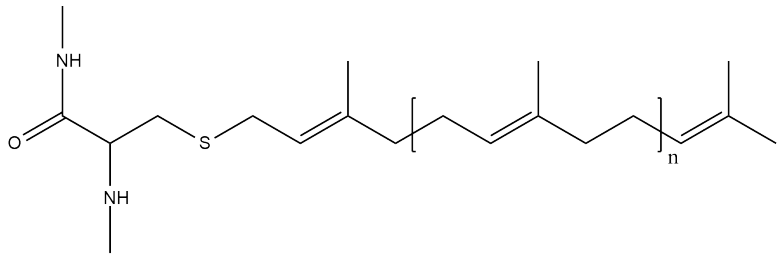

S-palmitoylation (Pal)

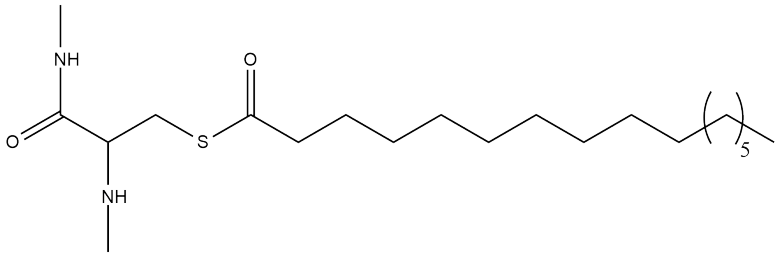

N-myristoylation (Myr) n=1
N-palmitoylation (Pal) n=2

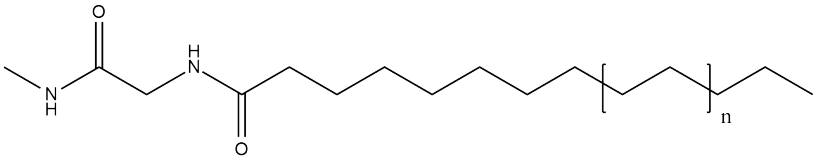

Figure 1-4 Types of hydrophobic site chains introduced by post-translational modification of membrane-binding proteins

The examples of membrane attachment anchors include:

- An *isoprenoid group* contains 15 (in farnesyl, Far) or 20 (in geranylgeranyl, GerGer) carbon atoms attached to a cysteine residue at the *C*-terminus via a thioether linkage. The carboxyl group of the cysteine may also be methylated
- A *palmitic acid* is a 16-carbon saturated fatty acid. It is attached to a cysteine residue via a thioester linkage

- A *myristic acid* is 14-carbon, saturated fatty acid, which is attached to a glycine residue at the N-terminus via an amide linkage.

Ras proteins are biologically active only when they are located on the inner side of the plasma membrane. For this purpose, the proteins undergo a series of posttranslational modifications (*10*). When Ras does not have these modifications it is located in the cytosol and is inactive. The part of hypervariable domain responsible for the membrane connection is the C-terminal **CaaX** motif, where **C** is a cysteine, **a** is aliphatic amino acid and X is any amino acid. The CaaX is a recognition sequence for farnesyl or geranyl geranyl transferase (FTase), which adds corresponding modifications near *C*-terminus. In case if farnesyl residue is added, farnesylpyrophosphate (FPP) is used as a source (Figure 1-5). After prenylation, the aaX tripeptide removed by a protease and the free cysteine esterified by a methyltransferase proteocytosolic carboxymethyltransferase (pcCMT).

All Ras proteins have farnesylated cysteine methyl ether at their *C*-terminus. From this point, further paths of the isoforms run differently: K-Ras4B has a polybasic stretch near the *C*-terminus, which induces electrostatic interaction with the positively charged membrane surface and the other isoforms receive one or more palmitoyl chains through action of palmitoyltransferase (PalTase). Figure 1-5 illustrates this processing on the example of the *N*-Ras protein.

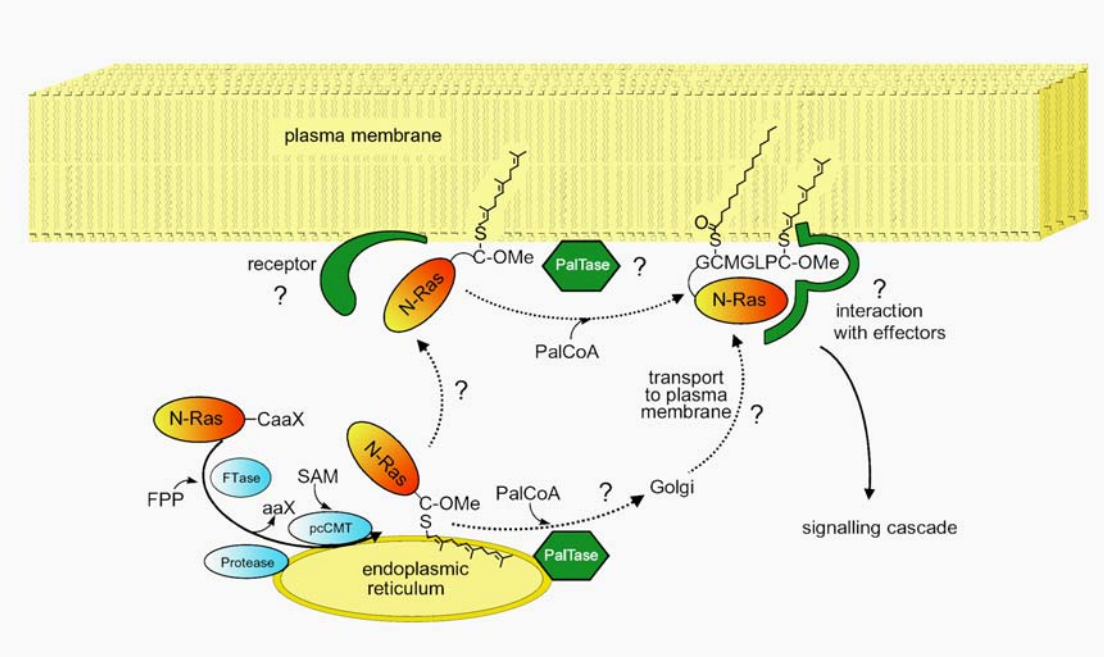

Figure 1-5 Schematic representation of post translational modification of *N*-Ras protein (*11*)

1.2 Biological Membranes

The living cell is surrounded by a lipid membrane, which are semi-permeable barriers with the primary function of separating the intracellular contents and the environment. The lipid membrane is involved in containment and separation, signal transmission, as well as the transport of ions and molecules.

1.2.1 Membrane Lipids: Structure and Properties

The lipids are a major component of biological membranes. Membrane lipids are very diverse: any specific membrane may comprise more than one hundred different types of lipid molecules.

1.2.1.1 Types of Membrane Lipids

Phospholipids - is the most abundant class of lipids in membranes. A molecule has four components: fatty acids, a glycerol moiety to which the fatty acids are attached, a phosphate, and a polar component (Figure 1-6). One of the hydroxyl groups of glycerol is associated with a polar group containing phosphate, and the other two - with hydrophobic residues. The fatty acid components provide hydrophobic properties, whereas the remainder of the molecule is hydrophilic facing the solution. In nature, different fatty acids (long-chain carboxylic acids) are bound to the glycerol via the ester bond. The alkyl radicals always have an even chain length due to specificity of the biosynthetic pathway. In addition to their alkyl chain length, the lipids also differ in the number of double bonds in the alkyl group (unsaturated fatty acids). The presence of double bonds reduces the melting temperature of the lipids, which allows the membrane to remain fluid at normal conditions. The alkyl chains are linked to the glycerol via relatively unstable ester bonds. In nature, the bond can be easily hydrolyzed of re-formed. In this way, cells are able to adapt their lipid membranes to the changing conditions of their environment as well as during their life cycle.

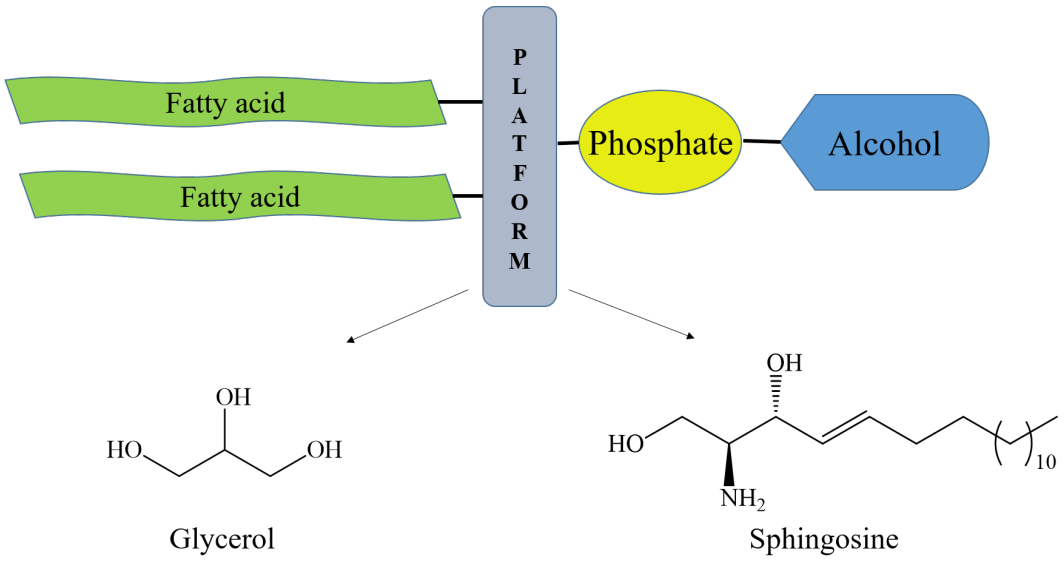

Figure 1-6 Schematic structure of a phospholipid

Based on the type of the platform lipids are classified in two main classes: phosphispingolipids (based on sphingosine) and phosphoglycerides (based on glycerol).

Phospholipids derived from glycerol are called phosphoglycerides (Figure 1-7).

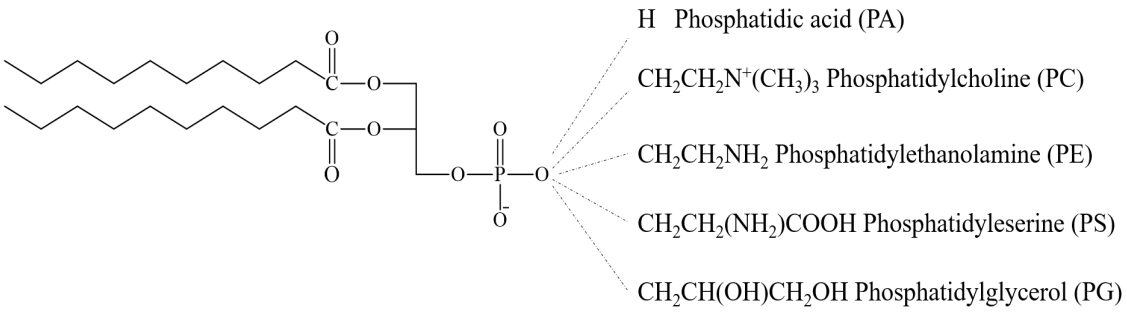

Figure 1-7 Structures of different phosphoglycerides

Phosphatidic acid is the simplest representative of phosphoglycerides and a precursor in the biosynthesis of other phospholipids. *Phosphatidylcholine (PC)* is a major cell membrane component of higher plants and animals. A bacterial cell does not contain PC. Phosphatidylcholine also plays a significant role in membrane-mediated cell

signaling. *Phosphatidylethanolamine* is one of the main components of the bacterial cells membranes. *Phosphatidylserine* plays a key role in cell cycle signaling, and works as a regulator of the activity of several membrane-bound enzymes. *Phosphatidylinositol* is a minor component on the cytosolic side of eukaryotic cell membranes.

Phosphatidylglycerol is the major component of bacterial membranes (70% total) (*12*). *Glycolipids* are lipids containing carbohydrates. Their role is to provide energy and serve as markers for cellular recognition. *Sterols* are neutral lipids, which are present in plants, animals and bacteria. Most abundant example of sterols is *cholesterol* (Figure 1-8).

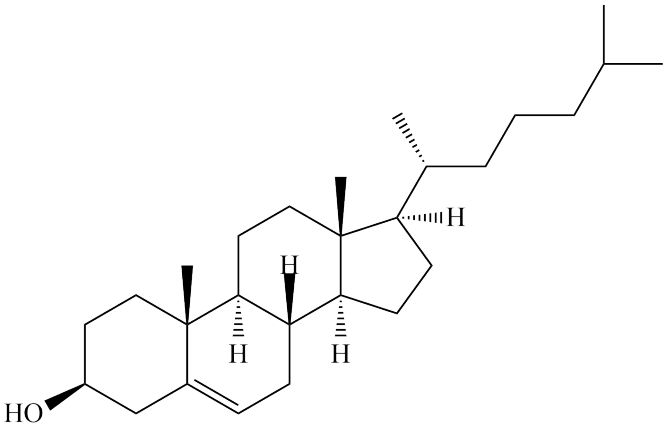

Figure 1-8 Structure of cholesterol

Cholesterol is an essential structural component of animal membranes and is required to maintain both membrane structural integrity and fluidity. In addition, it serves as a precursor for the biosynthesis of steroid hormones, bile acids, and vitamins.

1.2.1.2 Lipid Phases

In the presence of water, lipids self-assemble in a form of lipid bilayers. Depending on the lipid type, the temperature and the water content, phospholipids can form different phases. At low temperatures, lipids have chains ordered and organized into the membrane plane in a hexagonal lattice. Above a characteristic temperature that order is disrupted and the lipids transition into a more fluid phase. The phase below this melting point (T_m) referred as gel phase and the one above the melting point as a fluid or liquid crystalline phase (*13*). The melting temperatures of saturated chains of saturated C18-phospholipids are well above room temperature while in natural membranes with unsaturated fatty acids melting temperatures may be less than 0°C.

Solid-ordered phase is also referred to as a gel phase (Lβ). In the Lβ phase, the hydrocarbons are stiff, fully extended and regularly oriented on a two-dimensional lattice. They can rotate slowly (on a time scale of 100 ns) in this phase along their longitudinal axis, but show almost no lateral diffusion. Above a certain temperature or water content, the hydrocarbons produce a transition from the Lβ to a liquid phase, the Lα phase (*14*). This phase is characterized by a high lateral diffusion of the lipids and a lower degree of order of the hydrocarbon chains. Therefore, it is also referred to as a liquid-disordered (Ld) phase.

A particular case of the lipid phases in biomembranes is the liquid-ordered (Lo) phase (raft phase). On the one hand, this is characterized by a high degree of order of the hydrocarbon chains (similar to the Lβ phase); on the other hand the lipids show a high lateral diffusion (similar to the Ld phase) within the Lo phase (*15*). In cellular membranes cholesterol is tightly packed in the Lo phase between the carbohydrate chains of the

glycerophospho- and (glyco-) sphingolipids, forcing them to a higher order (*16*). In model membranes, this interaction can lead to microscopically distinguishable Ld / Lo phases. The Lo phase is rich in saturated glycerophospholipids or sphingolipids and cholesterol in such membranes, whereas the Ld phase is rich in unsaturated glycerophospholipids.

1.2.2 The Structure of Biological Membranes

1.2.2.1 The Fluid Mosaic Model of Membrane Structure

The present idea of the structure of cell membranes has been proposed by Singer and Nicolson in 1972 (*17*). They presented the fluid mosaic model, which resulted from the idea of a moving lipid bilayer. The lipids with hydrophobic hydrocarbon chains and hydrophilic head groups accumulate through hydrophobic interactions of the alkyl chains and form the lamellar double-layer structure by self-organization. Within the individual lipid layers, the lipids can move freely and the membrane thus behaves as a two-dimensional liquid. Movement of the lipids from one membrane sheet into another, the so-called flip-flop, is possible; but the kinetics of this process is slow. The integral membrane proteins (e.g., receptors and ion channels) penetrate the bilayer and are laterally mobile within the membrane. These membrane proteins form a link between the cell interior and the environment.

The membrane bilayer itself has a total thickness of about 40-50 Å. One layer consists of 15 Å-length alkyl chains and 5 Å hydrophilic head groups (Figure 1-9).

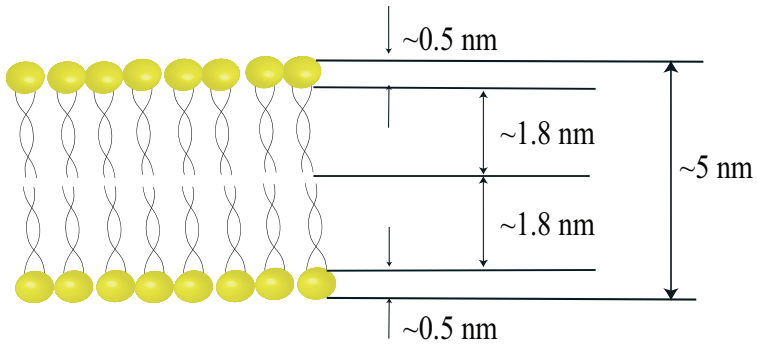

Figure 1-9 Dimensions of the lipid bilayer

1.2.2.2 Asymmetry in Membranes

Most cell membranes are asymmetric, i.e. the outer and inner side of the membrane differs in composition. This asymmetry involves both protein and lipid components:

- Asymmetry of proteins in biological membranes determined by their biogenesis
- Lipid asymmetry is a relative: usually the outer and the inner monolayer composed of same lipid types, but the concentration of lipids in each side varies.

Transmembrane distribution of lipids in membranes is defined by their biogenesis, and influenced by the outer media and inner cell conditions.

1.2.2.3 Subdomains in Membranes

After discovery of the liquid ordered phase, the fluid mosaic model of the membrane was revised (*18*). Rafts and caveolae domains have a capacity to selectively include or exclude proteins and thus alter protein/protein or protein/lipid guided

interactions (Figure 1-10). The size of the microdomains is different depending on cell type ranging is from 50 to 700 nm (*19*).

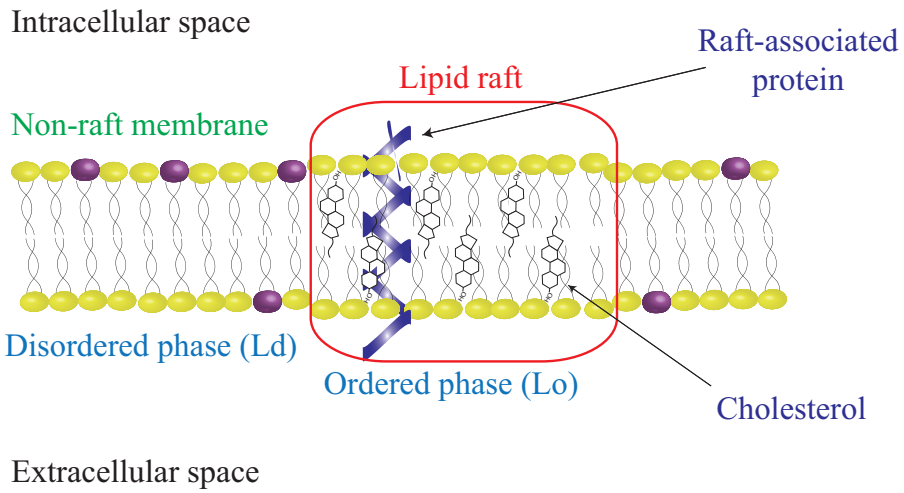

Figure 1-10 Schematic representation of lipid raft and proteins in a membrane

Lipid rafts and caveolae are specialized regions of the membrane thought to serve important biological functions. In particular, they provide a scaffold for organizing signaling protein complexes (*20*). The lipid composition of rafts and caveolae provides a unique membrane microenvironment rich in cholesterol and sphingomyelin, which create a liquid-ordered (Lo) phase domain promoting aggregation of signaling components.

Presently, membrane rafts are defined as combinations of glycosphingolipids and ordered assemblies of specific proteins, in which the metastable resting state activated by specific lipid–lipid, protein–lipid, and protein–protein interactions (*21*). It has been proposed that lipid rafts serve to collect proteins when needed for signal transduction.

1.2.2.4 Lipid Raft Dynamics

There are a number of challenges associated with studying of lipid rafts in living cells. Natural lipid rafts are quite small ranging from 10–200 nm, which is below the resolution limit of an optical microscope. Thus, lipid rafts are difficult to visualize and observe in vivo and in vitro. Using advanced laboratory methods and imaging techniques, such as fluorescence quenching, fluorescence microscopy, electron microscopy, X-ray diffraction and small-angle neutron scattering lipid rafts were detected in living cellular membranes (*22*). It became evident that the lipid rafts are dynamic and do not remain intact for a long time.

It is believed that formation of membrane domains is induced by molecular interactions between proteins and lipids. One remarkable example of this phenomenon is an induction of raft-like domains by a NAP-22 protein.

NAP-22 is a myristoylated protein found in neurons (*23*). From fluorescence microscopy studies, it is known that NAP-22 partitions into low-density fraction of neuronal membranes, suggesting it's affinity to rafts. It specifically interacts only with cholesterol-containing liposomes (*24*).

Atomic force microscopy (AFM) is one of a few imaging techniques with sufficient resolution to observe rafts. A tremendous advantage over electron microscopy is its temperature and physiological aqueous conditions. Because of the different packing of the Lo and Ld phases, these membrane domains have different thicknesses and detectable by AFM. Figure 1-11 schematically represents a lipid rafts protruding from a bilayer. On the right is the AFM image of protein associated with lipid rafts (*25*). Red

"islands" is a lipid raft emerging from the black background (disordered bilayer) and the tall peaks are protein molecules.

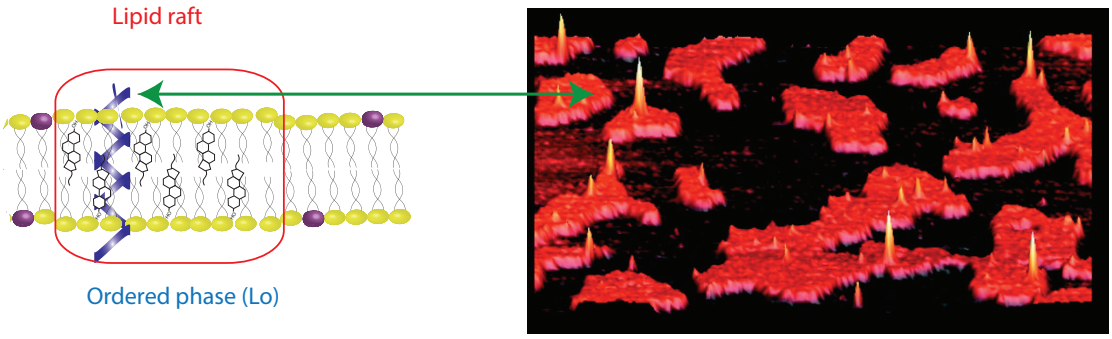

Figure 1-11 Lipid bilayer with rafts (red islands) and associated protein (peaks) (*26*)

Epand and colleagues studied specificity for cholesterol binding properties of NAP-22 by differential scanning calorimetry (DSC) and atomic force microscopy (AFM) (*27*). AFM revealed a significant change in the surface of a supported bilayer upon addition of NAP-22. Prior to the addition of the protein, the bilayer looked like a smooth structure with uniform thickness. Addition of NAP-22 resulted in the rapid formation of localized raised bilayer domains (Figure 1-12).

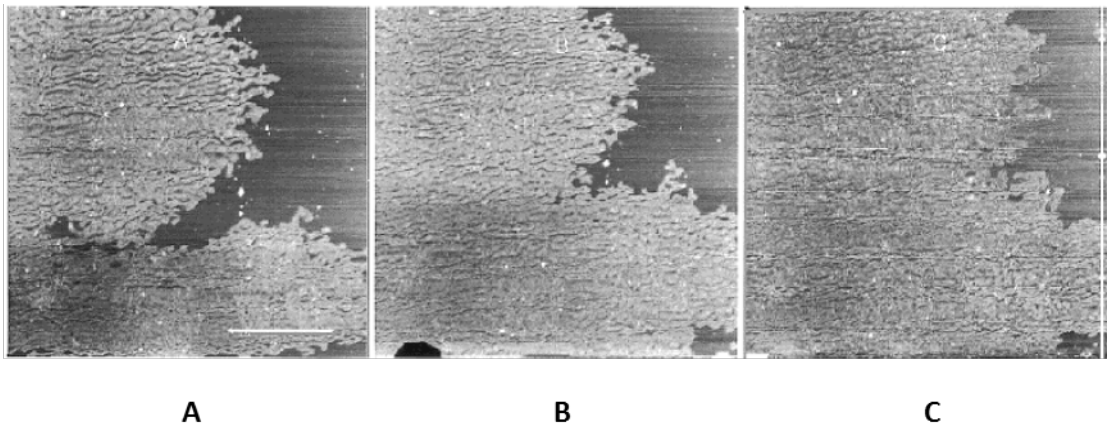

Figure 1-12 AFM height images of bilayer with cholesterol in the presence of NAP-22 taken 10 (A), 15 (B), and 20 min (C) after the addition of protein (*27*)

Remarkably, addition of the protein solution caused a rearrangement of the lipid bilayer without any destruction. These results clearly confirmed that NAP-22 induces the formation of cholesterol-rich domains in lipid membranes, which may be revealing organizing role of integral membrane proteins in a lateral lipid bilayer structure.

1.2.3 Model Lipid Bilayers

In contrast to the natural biological membranes, the term "model membrane" is intended to describe artificial lipid bilayers, which help to understand and imitate the structure, properties and functions of membranes. To date, model membranes developed for the construction of membrane models including black lipid membranes (BLM), supported bilayers, lipid bicelles, lipid vesicles and most recent development of phospholipid bilayer nanodiscs (Figure 1-13) (*28*), (*29*), (*30*). Some of these models will be discussed below.

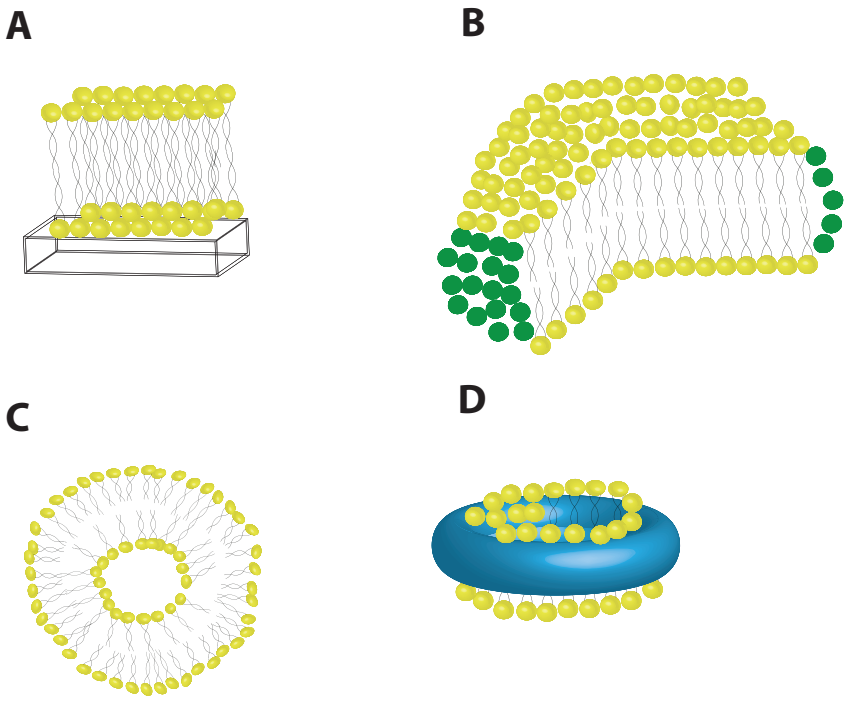

Figure 1-13 Examples of lipid assemblies: (A) supported lipid bilayer, (B) lipid bicelle, (C) lipid vesicle, (D) nanodisc. Drawing not to scale

1.2.3.1 Lipid Structures in Water. LUV and MLV

The lipids are amphiphilic substances, which are poorly soluble in both polar and nonpolar solvents. The presence of both hydrophilic and hydrophobic parts in the lipid molecule drives these compounds to form aggregates in the presence of water. The most energetically favorable state of a hydrated lipid is a monolayer at the interface between polar and nonpolar environment or a bilayer with two hydrophilic surfaces and hydrophobic interior (Figure 1-13).

The driving force behind of the lipid aggregates formation in aqueous media is hydrophobic effect (*31*). The basic principle is that hydrocarbon chains of fatty acids distort hydrogen bonds in water and, therefore, tend to self-associate. On the other hand,

lipid polar domains tend to interact with water and therefore stable in an aqueous environment (*32*).

The final shape of lipid structures in solution is defined not only by thermodynamic parameters but also by the structure of lipid molecules. There are three possible types of supramolecular structural organizations (phases) of lipids in aqueous media (Figure 1-14).

Depending on the volume ratio of the head groups and non-polar chains, all lipids divided into three groups: inverted cones, cylinders and cones. Repulsive forces between close head groups and tendency of fatty acids to self-associate defines the overall structure. Lipids with relatively close volumes of polar and non-polar parts tend to a form bilayer or lamellar structure, whereas other types of lipids form nonlamellar micellar and cubic phases. This ability of lipids referred to as *lipid polymorphism* (*33*).

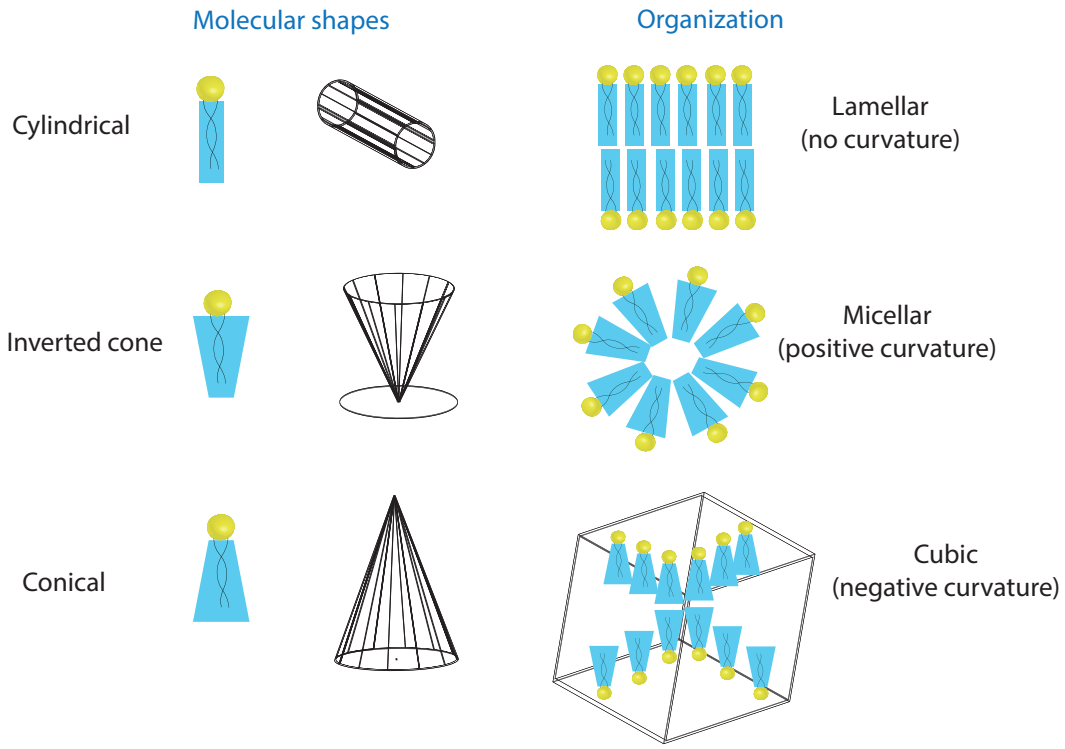

Figure 1-14 Lipid polymorphism: depending on the relative sizes of hydrophobic and hydrophilic parts lipids can form different lipid structures

If the lipids are placed in an aqueous environment, their molecules form aggregates - micelles, in which the polar heads of the lipids facing outward and nonpolar hydrocarbon chains hidden inside. In nonpolar medium micelles turned inside out, to form inverted micelles (Figure 1-15).

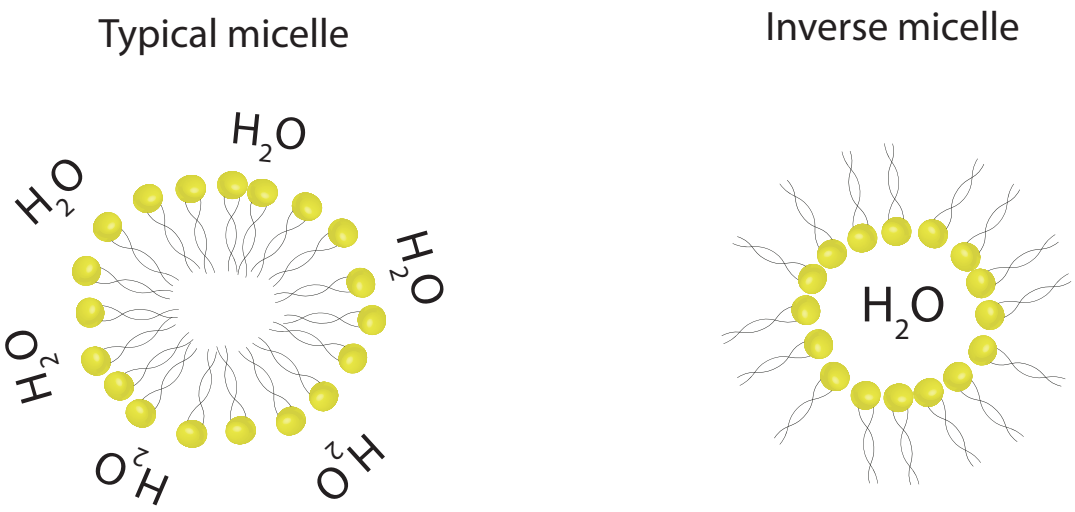

Figure 1-15 Lipid micelles in water (typical micelle) and non-polar solvents (inverse micelle)

When the concentration of lipids in water increases, the micelles eventually stick together and form a bilayer. Natural lipids have extremely low critical micelle concentration (CMC): 10^{-10} M. The thickness of the lipid bilayer is determined by the length of the hydrocarbon chains and usually around 4-5 nm, but it depends on the packing density of the lipid molecules in the bilayer.

With further increase of lipid concentration bilayers stratifying each other to form multilamellar lipid structures. Gentle stirring induces the formation of spherical particles – liposomes (Figure 1-16).

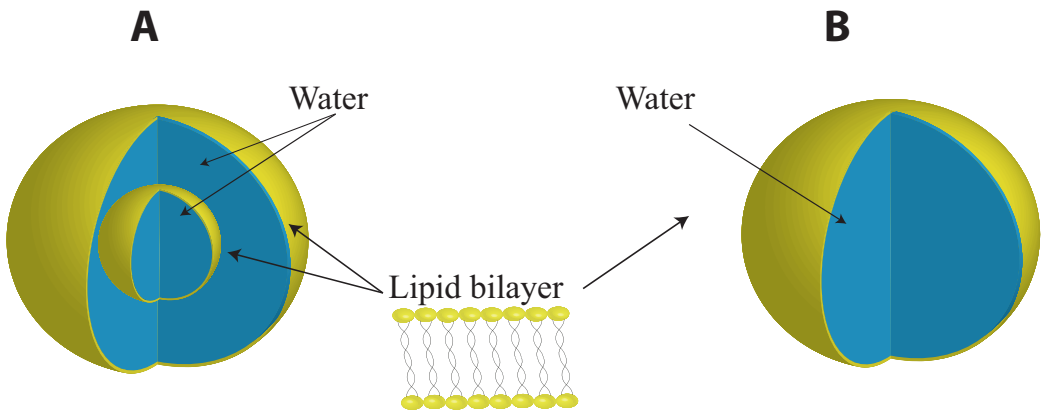

Figure 1-16 Schematic structure of liposomes: (A) multilamellar vesicles, MLV; (B) small or large unilamellar vesicles, SUV and LUV

Liposomes, typically, consist of a series of bilayers separated by water; the distance between the layers is 15-20 Å, liposome diameter range is 5-50 microns. Such liposomes, consisting of numerous bilayers, are known as multilamellar vesicles (MLVs). By gentle swirling of MLV, individual spheres are able to detach to form large unilamellar vesicles (LUVs). Small unilamellar liposomes (SUVs) can be obtained by ultra-sonication of MLVs. Another technique, which allows obtaining LUVs of the uniform size, is extrusion. In this method the lipid mixture is passed through the membrane of a specific pore size, which forces MLV to redistribute and form smaller LUV (*34*).

1.2.3.2 Supported Lipid Bilayers (SLB)

Due to their spherical geometry of LUVs and MLVs, only very few characterization methods and measurement methods are available. The range of different analytical methods is significantly greater on planar substrate-supported systems, in particular if this is a metallic or semiconducting substrate or an optically transparent

substrate. By means of Langmuir-Blodgett transfer (LB transfer) it is possible to transfer a lipid monolayer to hydrophilic substrates such as glass or surface-oxidized silicon(*35*). The second molecular layer can subsequently be applied, for example, via Langmuir-Schäfer transfer (*36*). For this purpose, the substrate with the first monolayer is immersed horizontally into the lipid monolayer pre-oriented at the water / air interface. A further method of completing the membrane is vesicle fusion (*37*). In this method, the first monolayer is also applied by an LB transfer, and the substrate is then transferred to a freshly prepared liposomal solution (Figure 1-17). The second monolayer then forms spontaneously. With this method, lipid bilayers can also be obtained directly, without the previous LB transfer of a monolayer.

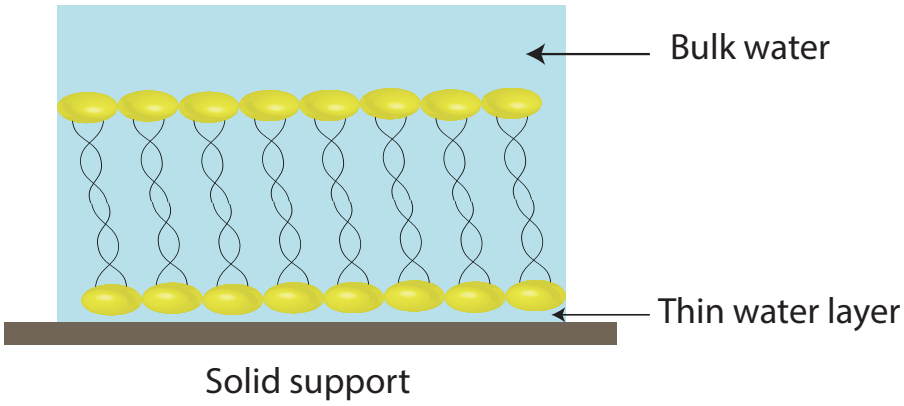

Figure 1-17 Supported lipid membrane on thin water film

The supported lipid bilayers do not directly contact the hydrophilic substrate. Instead, a very thin water pad separates a hydrophilic head groups from the substrate surface. The resulting water reservoir is very thin approx. 5 - 20 Å allowing allows lateral diffusion of the lipids in the lower membrane half (*38*), (*39*). Supported lipid bilayers

were successfully used for incorporation and analysis of small membrane proteins (*40*), (*41*).

1.2.3.3 Nanodiscs

Recently, another type of membrane mimics received a wide usage – lipid nanodiscs. The nanodiscs consist of a piece of bilayer surrounded by an amphipathic protein belt (MSP) shielding hydrophilic side of a bilayer from aqueous solution (*42*). For the reconstitution of different sized discs specifically tailored for different membrane proteins (*43*), (*44*).

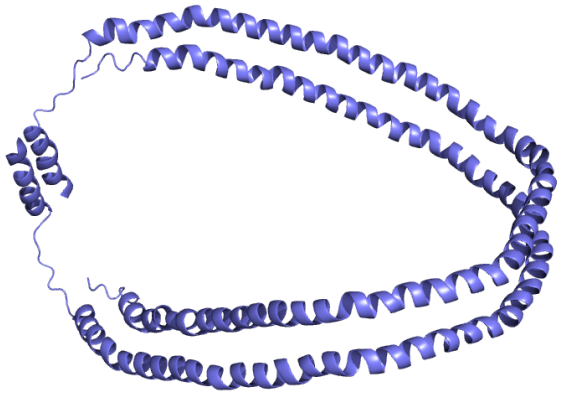

Figure 1-18 Structure of Apo-A1 used for nanodisc preparation

MSPs are alpha helical proteins derived from the apolipoprotein A-1 (ApoA1), which is the primary component of high-density lipoprotein particles (*43*) (Figure 1-18). A typical MSP1 is a truncated Apo-A1 fused to an N-terminal histidine tag by a linker containing a protease site for easy removal of the His tag. By changing the number of amphipathic helices of Apo-A1, the MSP sequence can be varied which allows for the

preparation of nanodiscs with different sizes, from 5 to 12 nm (*45*), (*46*). Formation of nanodiscs is spontaneous self-assembly process initiated by detergent removal from a lipid solution. Nano discs are more stable than lipid vesicles at low concentrations, which makes them a particularly useful for structural studies of membrane proteins (*47*), (*48*).

1.3 Bioorganic Synthesis of Ras Homologs

Synthetic peptides and proteins are among the most important tools in chemical and biomedical research areas. Introduction of solid-phase peptide synthesis by Merrifield in 1963, who synthesized the nonapeptide bradykinin within a few days revolutionized the field (*49*). This technique allowed for production of proteins and peptides, which cannot be expressed in cells or difficult to isolate. The progress in solid state peptide synthesis continues today with development of new resins, protective groups and coupling reagents for production of functionalized.

1.3.1 Principles of Solid Phase Synthesis

The solid phase synthesis uses the polymeric reactive carrier, which functionalized to attach other substrates (Figure 1-19). Because of the presence of inert solid support, large excess of reactants may be used, driving reactions to completion. The reagent excess is easily removed by washing the resin with an appropriate solvent. In the beginning the substrates were applied directly to the polystyrene supports, but later the linker systems between the polystyrene resin and the functional group were introduced, which allows cleaving the final product off the resin under a variety of conditions (*50*).

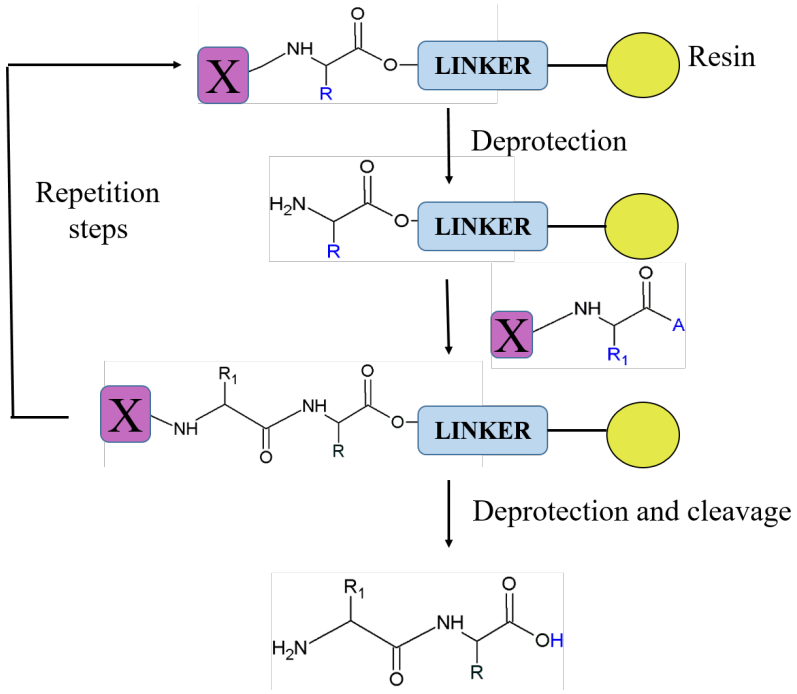

Figure 1-19 Principle of solid phase synthesis of peptides (X = protecting group; A=amino acid)

The linker is bifunctional: one end of the linker is used to attach the molecule to be synthesized; this bond should be easily cleaved under special conditions (e.g., silyl ethers, esters). The other part is connected to the polymeric matrix via a stable bond (for example ether, amide).

Some of available linkers are in fact, based on protective groups and therefore inherit a rough classification based on their cleavage conditions (Figure 1-20).

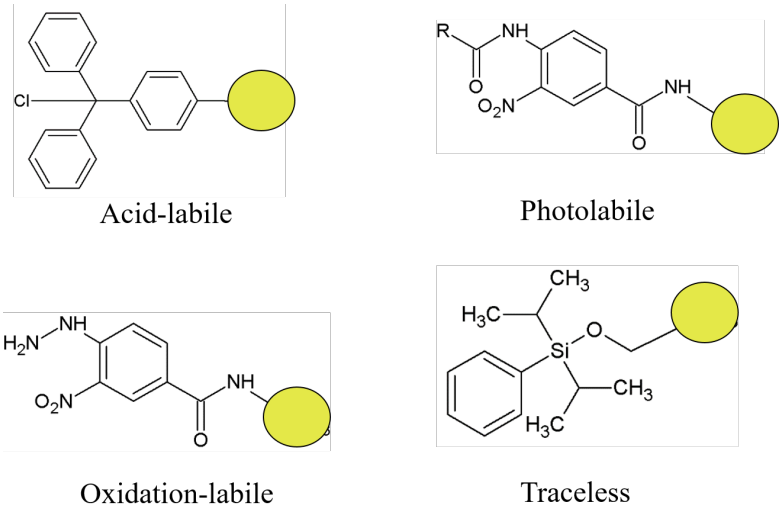

Figure 1-20 Types of linkers used in solid-phase synthesis

In order to obtain a peptide on a solid phase, there is a need for so-called coupling agents in order to increase the reactivity of molecules to be coupled.

1.3.2 Synthesis of Lipidated Peptides

The synthesis of lipidated peptides is challenging because of the presence of multiple active groups and labile ester bonds in proteins. Introduction of hydrophobic side chains leads to a completely different behavior of lipopeptides in solution compared to non-lipidated peptides. Therefore, ether precipitation that is normally used for the purification of peptides is useless here. In addition, instability of the lipid groups leads to other limitations. For example, thioester linkage is not stable towards nucleophiles, and isoprenyl residues are sensitive to acids and unstable to reductive conditions (Figure 1-21). Furthermore, in the case of Ras proteins *N*-terminal carboxyl group should have methyl ester form.

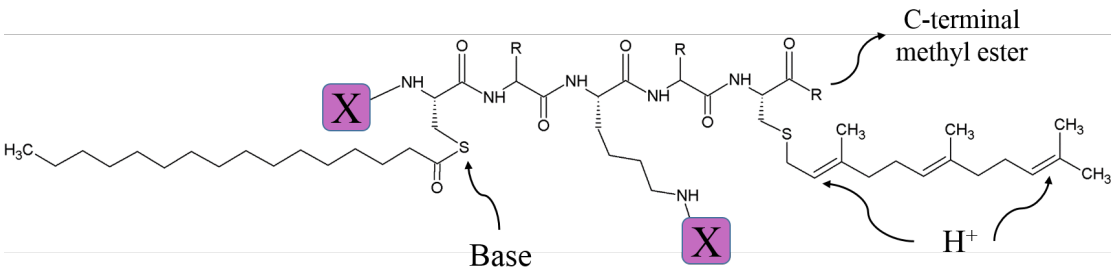

Figure 1-21 Acid-base sensitivity of lipid groups in Ras lipopeptides (X=protection group)

There are two strategies for synthesis of modified peptides: the modification can be introduced either by coupling modules or by subsequent modification of the selectively deprotected peptide. First strategy implies to use pre-lipidated building blocks that are coupled during the synthesis on the solid phase. Second approach utilizes unmodified peptide that receives palmitoyl and the farnesyl residues on the solid phase (*51*), (*52*).

1.3.3 Modular Approach for Semi-Synthetic Ras Proteins

The modular approach for production of semi-synthetic proteins combines organic synthesis of lipopeptides and expression of the remaining part of Ras-protein. A great advantage of such approach is that one can introduce novel properties (e.g., fluorescent labels) without affecting the protein core. Effective ligation strategy is a key for producing peptide and protein conjugate faithfully mimicking natural lipoproteins. There are three possibilities to generate artificial lipopeptide-protein conjugates with Ras: in vivo farnesylation, maleimidocaproyl linkage and native chemical ligation (Figure 1-22).

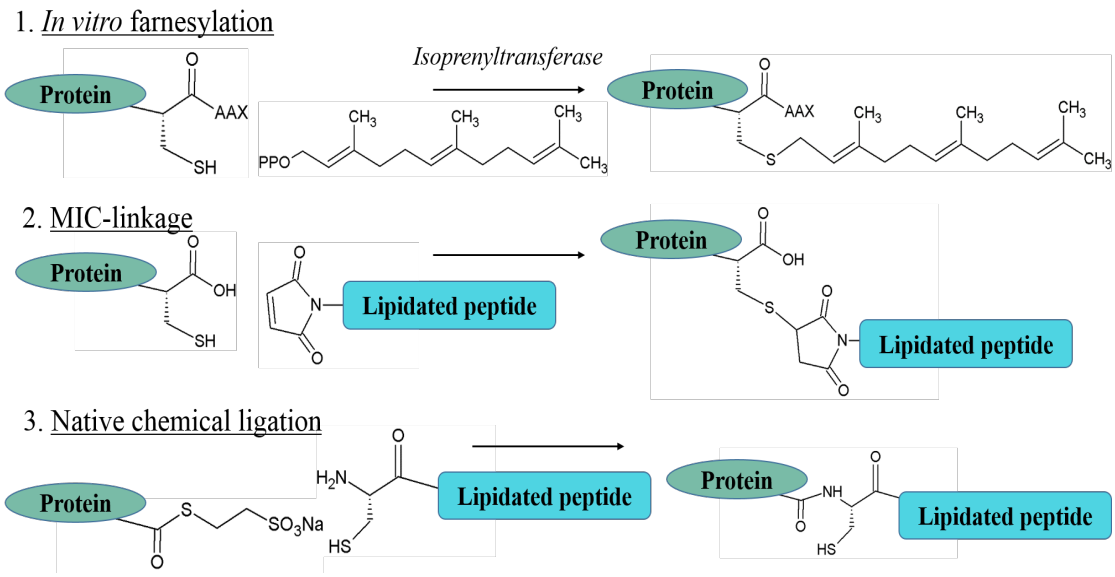

Figure 1-22 Strategies for the synthesis of artificial protein conjugates

First, modified lipids can be introduced via enzymes. Thus, Ras proteins can be modified *in vitro* using the farnesyltransferase (*53*). However, this is not a general approach for the synthesis of lipoproteins, for example, the palmitoyl residue cannot be introduced enzymatically. In a second approach, synthesized lipopeptides are attached to truncated proteins with the aid of a maleimidocaproyl (MIC)-linkers. The third approach uses the principle of native chemical ligation, where lipopeptides coupled with constructs obtained from the overexpressed protein. The latter two methods will be discussed in the following subsections.

1.3.4 Coupling of Lipopeptides via the MIC-Linker

In this method, a terminal maleimidocaproyl group is coupled to the lipopeptide. MIC is a thiol-specific electrophilic group that reacts selectively with the *N*-terminal thiol of cysteine of the truncated Ras protein (Scheme 1-1) (*54*), (*55*). The reaction performed

in a buffer system; the reaction products are purified by detergent extraction and chromatography. By this method, a number of Ras proteins with various lipidation motifs were synthesized in multi-milligram quantities and high purity (*56)*.

The main disadvantage of this method is that the bond between protein and peptide is non-native introducing an artificial spacer of ~ 2 Å. However, protein-peptide conjugates with such unnatural linker were shown to preserve their biological function as a molecular switch in signal transduction *in vivo* (*56, 57*).

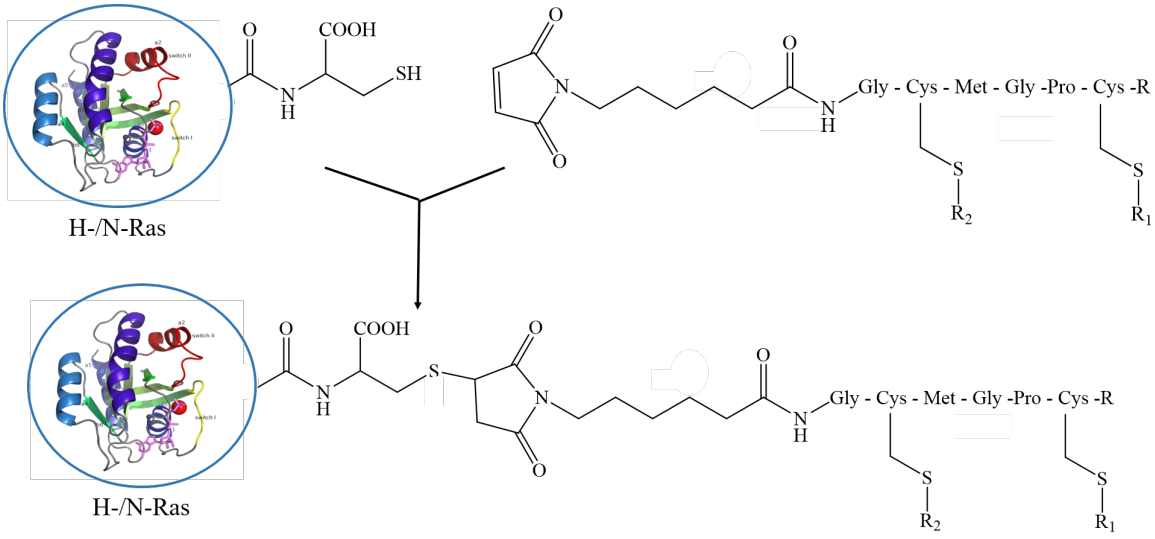

Scheme 1-1 Creation of full-length lipidated Ras protein through MIC-ligation

1.3.5 Native Chemical Ligation

Along with the artificial MIC ligation, a completely natural, ideally suited to protein synthesis technique called *native chemical ligation* was developed in the Kent laboratory in 1994 (*58*). This method takes advantages of biochemical reactions involving interactions of carboxyl and thiol groups and *S,N*-acyl rearrangement.

1.3.5.1 Principle of Native Chemical Ligation

This strategy involves the chemoselective reaction that occurs between a peptide containing an *N*-terminal cysteine residue and a second peptide containing thioester group (Figure 1-23) (*59*).

The initial transthioesterification reaction is followed by a spontaneous intramolecular *S,N*-acyl shift to generate amide bond between two fragments.

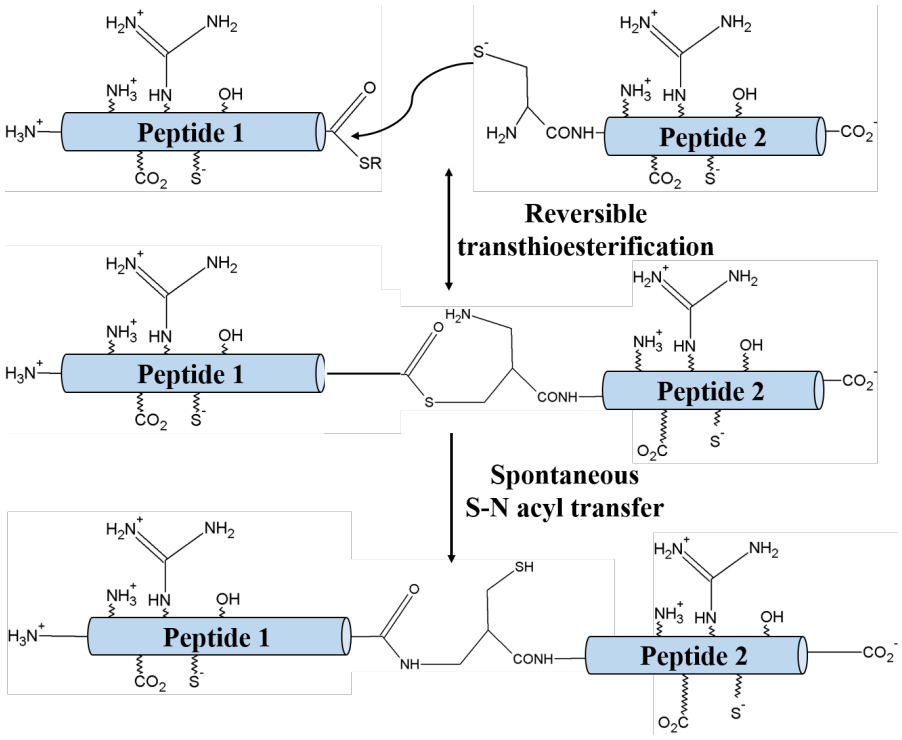

Figure 1-23 Schematic principle of native chemical ligation (*11*)

The only requirement of this technique is that the peptide fragments contains the necessary reactive groups, either cysteine or thioester.

1.3.5.2 Protein Splicing and Expressed Protein Ligation

In analogy with well-known process of mRNA splicing, in which introns are removed and exons are joined, another form of proteins post-translational modification was discovered in 1990, called the *protein-splicing* (*60*), (*61*). It is an intramolecular reaction of a particular protein in which an internal protein segment is released and *C*-terminus and *N*-terminus can be joined. Chemical ligation of this kind using recombinant *C*-terminal thioesters known as *expressed protein ligation*.

The Expressed protein ligation (EPL) or Intein-mediated Protein Ligation (IPL) is broadly applicable *in vitro* method for the chemoselective addition of modified peptides to recombinant proteins (*62*). This technology enables to introduce a number of modifications and unnatural amino acids into final proteins.

Based on the studies of the mechanism of protein splicing New England Biolabs developed a novel protein purification system that allows recombinant proteins to be purified without affinity tag - IMPACT (Intein-Mediated Purification with an Affinity Chitin-binding Tag). The IMPACT permits expression of target proteins carrying an intein-chitin binding domain (intein-CBD) tag for one-step purification using a chitin resin (Figure 1-24) (*63*). The advantages of this method were used for *in vitro* synthesis of two Ras-type proteins (*64*).

The Ras moiety was expressed with an intein and with a chitin-binding domain for easy purification (Figure 1-24). Then by analogy with protein splicing, intein cleavage induced by addition of mercaptoethanesulfonic acid sodium salt (MESNA) (*65*). The resulting protein, activated via a thioester, was attacked in a native chemical ligation reaction by the thiol group of the *N*-terminal cysteine of the lipidated peptide. Finally,

spontaneous *S,N*-acyl rearrangement generates the native peptide bond between the protein and peptide.

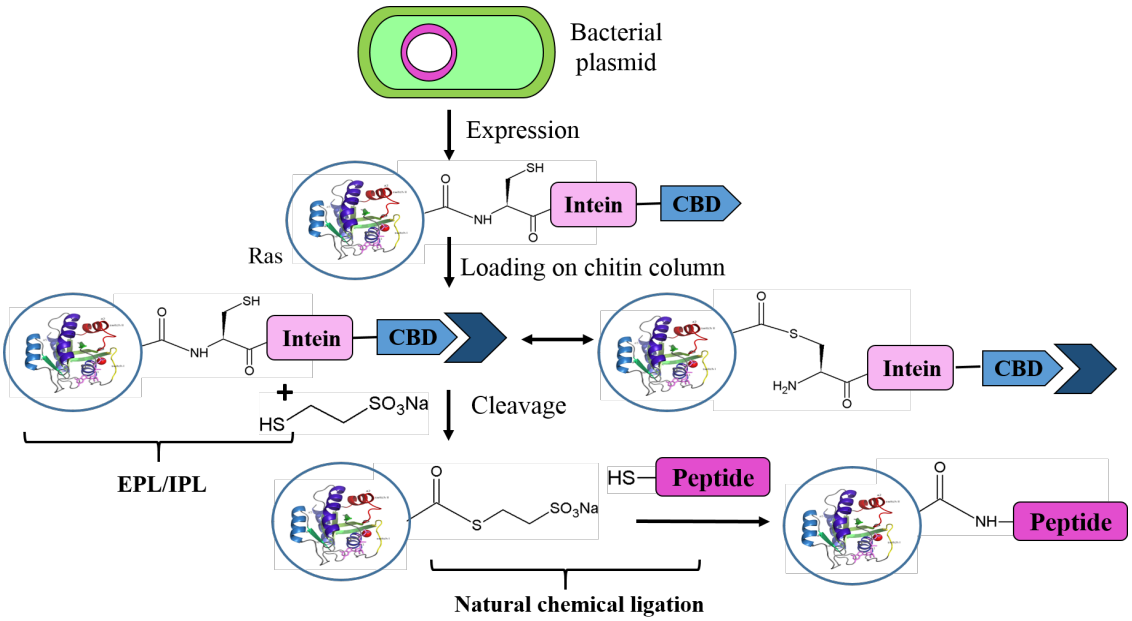

Figure 1-24 Schematic principle of expressed protein ligation (*11*)

Activity of the obtained semisynthetic *H*-Ras/*K*-Ras lipoproteins was confirmed via an interaction assay with the catalytic domain of the guanine-nucleotide-exchange factor SOS (*66*).

1.4 Semisynthetic Ras as a Tool in Biology

1.4.1 Interaction of Lipidated Ras Peptides with Membrane Models

Understanding of behaviour of lipid-modified protein in a membrane requires knowledge of contributions from the lipidated peptide. The modular synthetic approach provides an ability to incorporate various labels (fluorescent, EPR, etc.) almost in any

position of lipidated peptide allowing application of NMR, FTIR and small angle neutron diffraction spectroscopy among other techniques.

Huster and co-workers characterized the dynamic distribution of the simplest system - doubly lipidated *N*-Ras heptapeptide (Figure 1-25) by Fourier-transform infrared, solid-state NMR spectroscopy, and neutron diffraction (*67*).

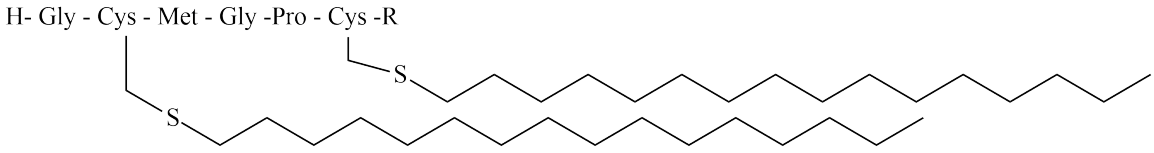

Figure 1-25 Double lipidated *N*-Ras heptapeptide (*67*)

The neutron scattering study revealed complete insertion of lipopeptide anchors into the hydrophobic matrix of the membrane. Hydrophobic side chains of leucine, cysteine and methionine delivered additional contributions to membrane incorporation, while the peptide backbone was located in the interphase between lipid and buffer. These conclusions were supported by FTIR measurements as phase transition temperatures of lipid and peptide were at exactly the same temperature (*67*). The order parameters calculated separately for peptide and lipid chains revealed that peptide acyl chains are inserted with much lower order parameters compared to the lipid acyl chains: the longer 16:0 peptide anchors slightly shrink to match the length of the phospholipid 14:0 chains (Figure 1-26).

Vogel and used ^{2}H NMR to explore the mechanism of insertion of lipidated Ras into membranes. The lipid chains revealed large order parameters suggesting that the lipid modifications are highly dynamic and flexible in the membrane (*68*).

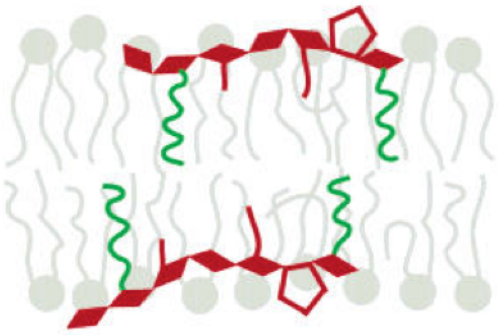

Figure 1-26 The membrane insertion of the lipid-modified peptide (*68*)

Tagging proteins with fluorescent probes provides a tool to study them by microscopy and fluorescence techniques, such as Förster resonance energy transfer, fluorescence correlation spectroscopy and fluorescence polarization.

A study by Janosch and coworkers represents a preliminary data collected for lipidated peptides bearing fluorescent dyes (*69*). The group used two-photon excitation fluorescence spectroscopy on giant unilamellar vesicles (GUVs) with incorporated BODIPY–labeled peptide. *N*-Rh-DPPE lipid was used as a marker of the Ld phase.

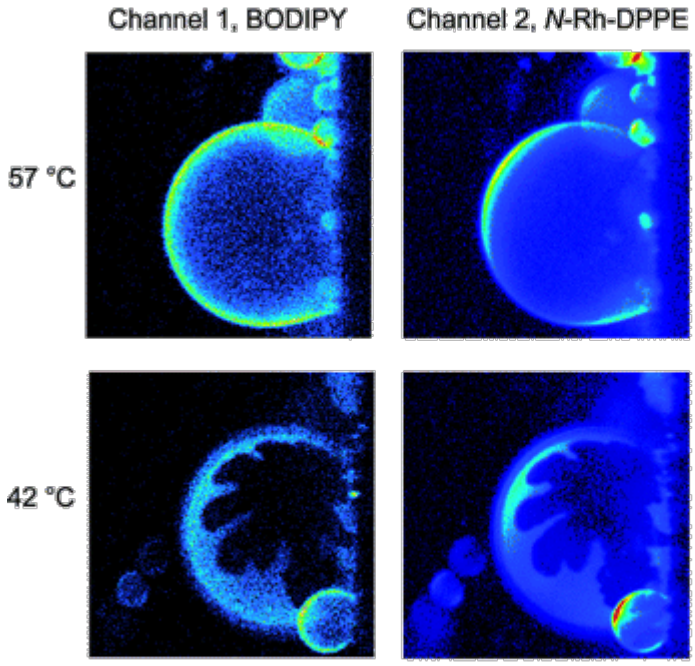

Figure 1-27 Two-photon excitation fluorescence intensity images of GUV with incorporated BODIPY-labeled peptide (*69*)

Addition of the fluorescently labeled Ras peptide to the GUV led to a phase separation, which was explained by the high affinity of the lipidated peptide to a liquid-ordered environment (Figure 1-27). The size of peptide-containing domains decreased upon decreasing temperature and peptide aggregation occurred at low temperature.

Authors found difficulty to explain the clustering of lipopeptides. The two possible reasons are the tendency of lipid anchors to self-aggregation or the fact that the BODIPY molecules form dimers, which prevail at low temperatures and higher concentrations.

1.4.2 Studies of Full-Length Lipidated Ras Proteins

The lipid modification of membrane-associated proteins determines the localization in rafts domains of the plasma membrane. Variety of *G*-proteins, thought to be localized in lipid rafts (*70*). The presence of myristoyl or palmitoyl also leads to a preferred rafts localization, as was found for α-subunits of heterotrimeric G proteins (*71*). The insertion of saturated lipid anchor in the tightly packed lipid rafts structures appears to be energetically favored. However, cholesterol-modified proteins, such as transmembrane proteins show enrichment in rafts structures. In that case, probably amino acids near the transmembrane helix play a critical role (*72*). Prenylated proteins, such as proteins with a farnesyl or geranyl-geranyl anchors found outside of rafts domains (*73*). The storage of bulky, branched structure of unsaturated isoprenyl chains is energetically unflavored in tightly packed rafts.

A number of studies were done to investigate the structural dynamics of membrane association of full-length lipidated Ras proteins. However, only a few techniques are applicable to these studies. For instance, X-ray crystallography methods are not applicable due to poor solubility of lipidated protein. Solution NMR also fails because the samples are too large to tumble with a short correlation time, which gives very broad signals. However, magic-angle spinning (MAS) NMR was successfully applied to those systems (*74*).

1.4.2.1 NMR Studies

Recently, Huster et al. showed that MAS NMR of bilayer bound lipopeptides provide ability to determine a structural model of semi-selectively labeled *N*-Ras protein bound to DMPC membranes (*75*). The obtained chemical shifts provided the input parameters for the structural calculations in program package TALOS (*76*). TALOS is a database program, which contains chemical shift information from proteins of the known X-ray structure. On this basis, the backbone torsion angles may be calculated from the structure and sequence similarities, which gave the first model of full-length lipidated *N*-Ras protein inserted in DMPC (Figure 1-28) in complete agreement with previous FTIR study (*67*).

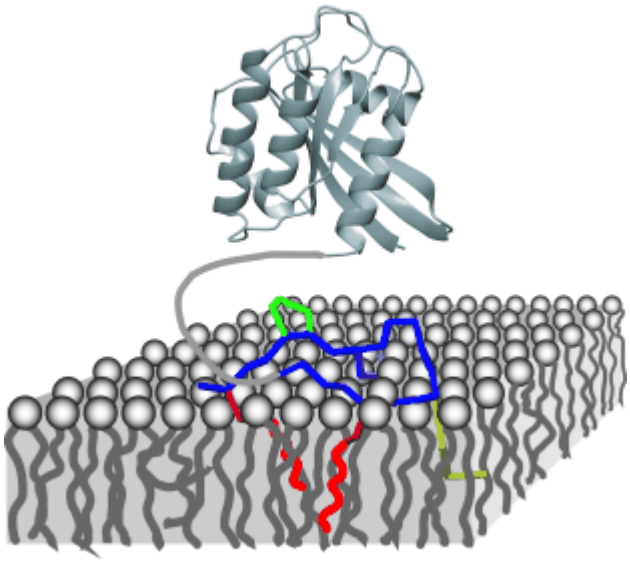

Figure 1-28 Structural model of the membrane-bound *C* terminus of lipid modified *N*-Ras protein (*75*)

1.4.2.2 IRRAS Study of Lipid–Protein Interaction

To reveal how different Ras isoforms interacts with lipid membrane a number of experiments were performed, with lipid monolayers using infrared reflection absorption spectroscopy (IRRAS) (*77, 78*) as well as X-ray diffraction (*79*).

Among a wide variety of membrane models lipid monolayers at the air/water interface (Langmuir films) are the simplest experimental models for biophysical studies of lipid-protein interactions. They provide several practical advantages from an experimental viewpoint: aqueous environment with conditions closed to the nature ones, easily controlled composition, temperature, pH etc., small quantities are required for experiments.

In the mid 1980's Dluhy and colleagues showed that IR spectroscopy may be applied to the lipid films with acquiring molecular structure information (*80*). The technique was called IR infrared reflection-absorption spectroscopy (IRRAS). It is based on the phenomenon that when mid-IR radiation strikes monolayers films, and around 6% of the light is reflected from the molecular constituents of the surface. Depending on optical properties of the irradiated interface, it is possible to get a set of IRRAS intensities and determine the orientation of ordered structural elements (e.g., lipid chains, protein secondary structures, etc.) (*81*).

Meister et al. used this technique to access the influence of Ras lipidation motif to membrane interaction. Group examined two variations of protein: native farnesylated and hexadecylated (HD/Far-*N*-Ras) and a doubly-hexadecylated (HD/HD-*N*-Ras) (Figure 1-29) (*77, 78*). Langmuir monolayers with lipid composition POPC/BSM/Chol (2:1:1) were used as a model of rafts.

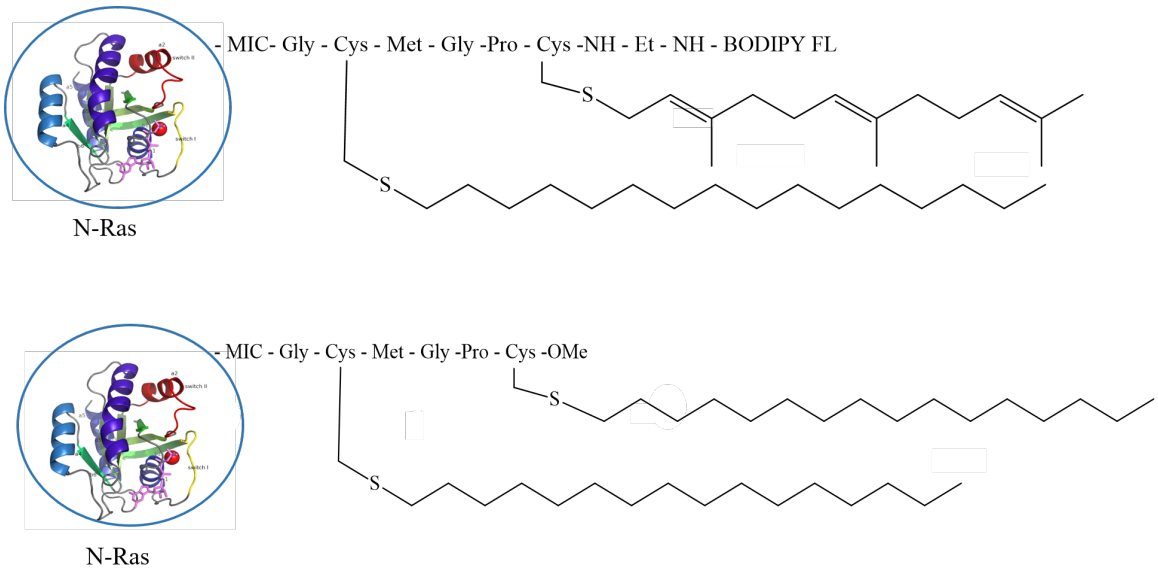

Figure 1-29 Structures of Ras constructs (*77*)

The process of fusing constructs with monolayer was investigated upon changing lateral pressure. It was found that the insertion of HD/Far Ras takes place only at low lateral pressure of 10 mN/m, whereas HD/HD *N*-Ras inserted at higher pressure (30 mN/m). Upon elevated pressure farnesylated/hexadecylated protein was desorbed from the lipid, whereas the doubly hexadecylated protein remains incorporated, indicating a higher affinity. These results confirmed an idea that short unsaturated had lower affinity toward liquid-ordered phases. Authors also concluded that farnesylation alone is insufficient for anchoring the protein in the plasma membrane (*82*).

1.4.2.3 Preferential Localization of Ras Isoforms

The involvement of the membrane microdomains domains to Ras-dependent signaling has been investigated in number of publication discussed further. Different studies produced somewhat controversial results about sub membrane localization for

different Ras isoforms. Current view is that farnesylated only *K*-Ras function outside of rafts, whereas palmitoylated *H*-Ras and *N*-Ras localized in raft domains (Figure 1-30).

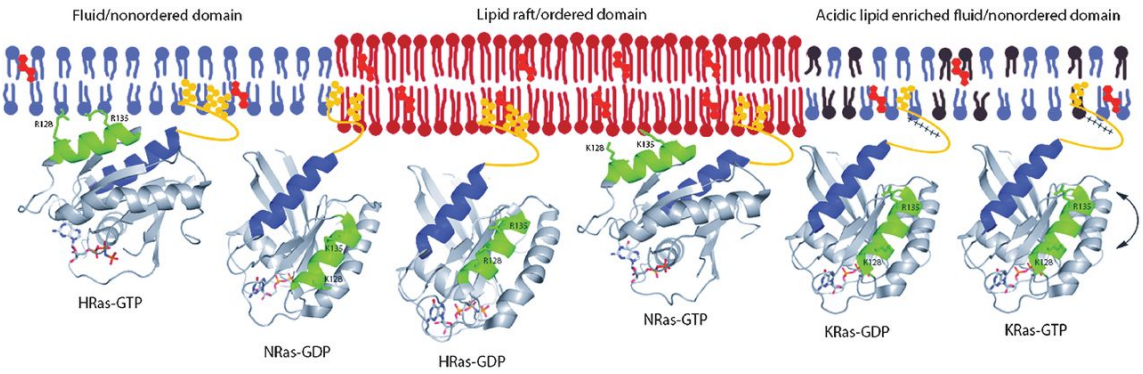

Figure 1-30 Membrane localization of Ras isoforms (*82*)

The explanation is that long chains of saturated fatty acids, such as palmitoyl, fit well into the ordered lipid structure of rafts whereas the kinked structure of prenyl moieties disfavors raft localization (*73*).

Prior et al. in their studies postulated that *H*-Ras in the GDP-bound state localized in lipid rafts, whereas GTP-state predominantly found outside of rafts structures. On the contrast, *K*-Ras protein localized predominantly in non-rafts fractions regardless of the bound nucleotide (*83*).

In addition to biochemical studies, there is biophysical evidence of localization of Ras proteins in distinct lipid domains. In electron microscopic studies on cell membranes, the inactive *H*-Ras distributed between rafts domains and cholesterol-independent microdomains was shown, while *K*-Ras and *H*-Ras predominantly localized in cholesterol-enriched domains (*19*). In fluorescence recovery after photo bleaching (FRAP) experiments it was shown that *H*-Ras, in contrast to *K*-Ras, is localized in rafts structures, while the mutants *H*-RasG12V and *K*-RasG12V associate with cholesterol domains (*84*).

In the last few years, researches received completely controversial results regarding Ras isoforms localization. Thus, Alexander Vogel's group investigated partitioning of *N*-Ras between liquid ordered and liquid disordered phases of model membranes (*85*). Several lipid mixtures composed of cholesterol, saturated, and unsaturated phospholipids were used to create lipid raft model systems:

- PSM/POPC/Chol – mixture with two coexisting phases. The presence palmitoyl-sphingomyelin (PSM), which is associated with the Lo phase, gives ability to mimic natural rafts. The POPC (1-palmitoyl-2-oleoyl-sn-glycero-3-phosphocholine) is enriched in the Ld phase;
- DPPC/POPC/Chol - PSM was replaced by another saturated lipid DPPC (1,2-dipalmitoyl-sn-glycero3-phosphocholine).

Interactions of *N*-Ras solution with model systems were visualized by Atomic Force Microscopy (AFM). In AFM a tiny cantilever with a sharp tip is scanned across a surface (Figure 1-31) (*86*). The interaction between the surface and the tip cause the cantilever to bend and the bending is monitored using a laser beam. In this way nanometer changes in height can be measured and used to generate a three-dimensional image of surface.

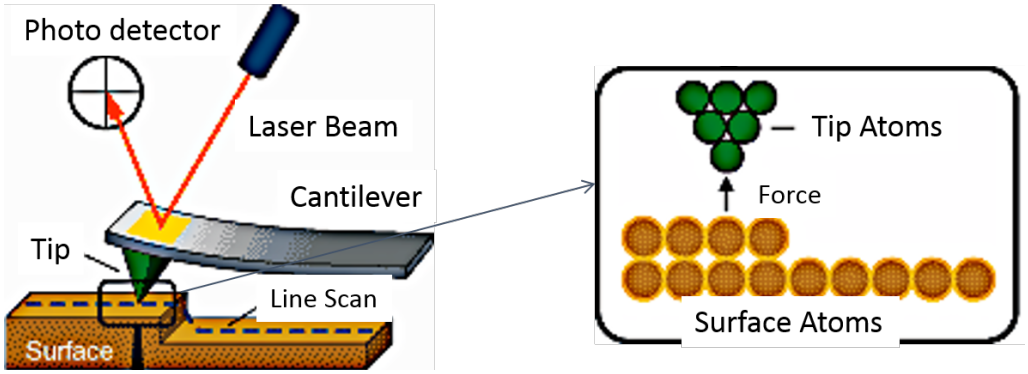

Figure 1-31 Schematic principle of atomic force microscopy (*87*)

Because of the different properties of the Lo and Ld phases membrane domains has different height they detectable by AFM. It also works in aqueous conditions necessary for natural lipids behavior and became the widely used method for visualization of proteins raft-complexes. Figure 1-32 shows the corresponding AFM images of *N*-Ras incorporated in a mixture that comprises Ld and Lo domains.

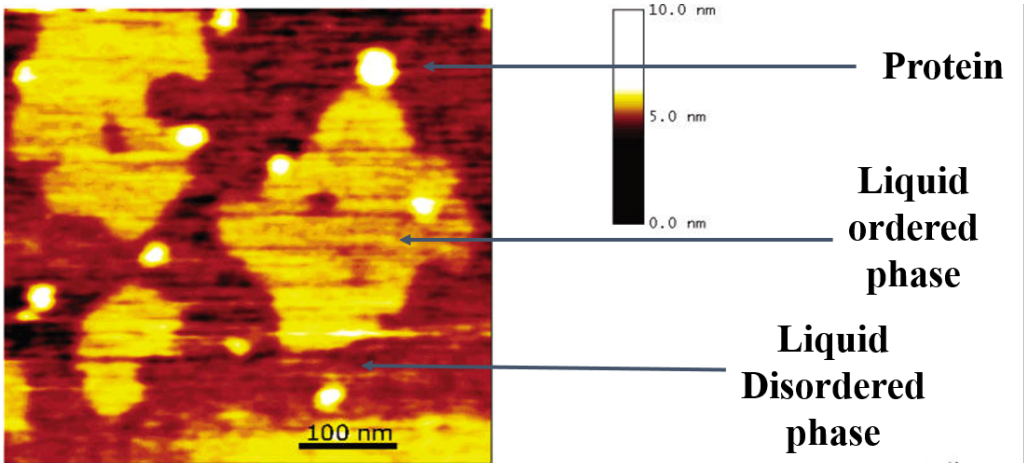

Figure 1-32 AFM image of N-Ras in GUV particles and concomitant section profile of the AFM image (*88*)

The results of study were in complete disagreement with the theoretical predictions. The proteins was excluded from both Lo and Ld domains and distributed on the boundary of phases (Figure 1-33) regardless of lipid composition.

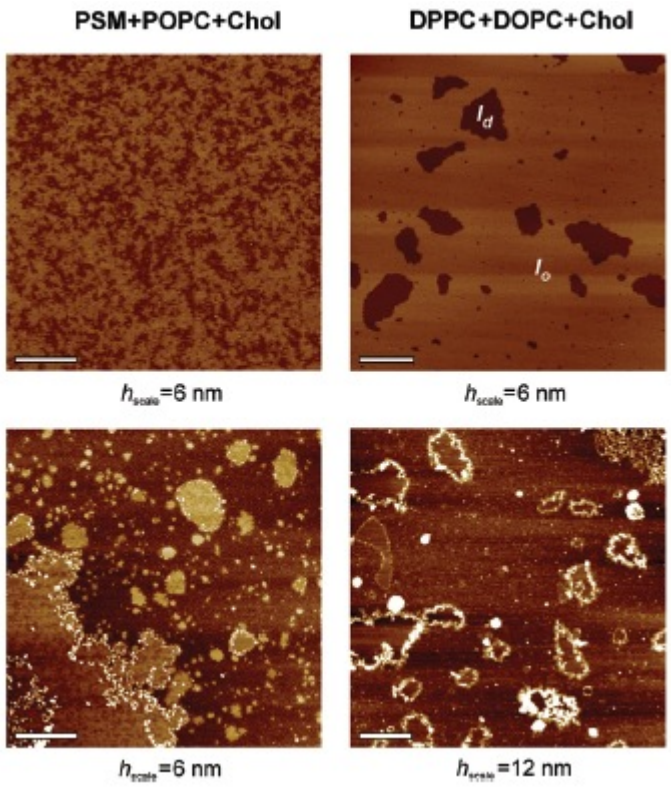

Figure 1-33 AFM images of lipid bilayers before (upper images) and after (lower images) addition of *N*-Ras (*85*)

These results demonstrated that membrane-partitioning behavior of Ras proteins is a very complex and may be influenced by a number of factors. Protein association with lipid micro domains was also influenced by membrane composition. One example of this correlation was described by Nicolini et al (*88*). BODIPY labeled and completely lipidated (hexadecylated and farnesylated) *N*-Ras protein incorporated into GUV (Figure 1-34) was observed by two-photon excitation fluorescence. The results similar to those one with lipidated peptide were obtained: protein binds preferentially to the liquid-disordered domains.

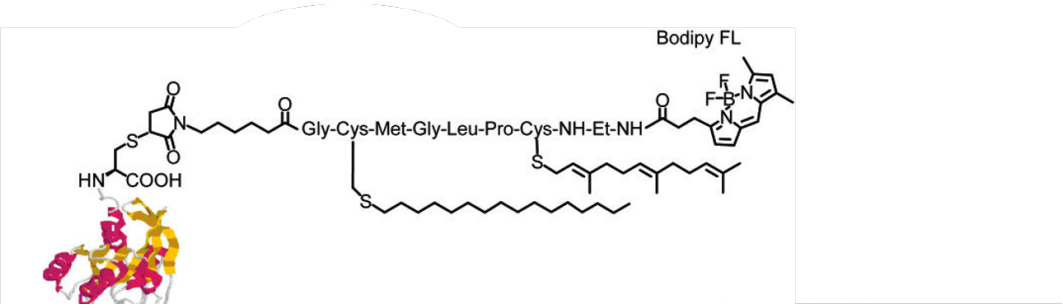

Figure 1-34 BODIPY-labeled fully lipidated *N*-Ras protein (*88*)

By use of image analysis, the partitioning of the lipidated protein in the various domains was analyzed. The final AFM results indicated that *N*-Ras spontaneously inserts into raft mixtures and preferentially into liquid-disordered domains, with a large contribution of the lipidated peptide residing in the boundary.

Werkmüller et al. used time resolved fluorescence anisotropy to study the mobility of full-length *K*-Ras4B with a BODIPY label in the protein core upon binding with a membrane (*89*). Binding to various model-membrane systems, including pure-fluid, liquid-ordered and (Lo/Ld) heterogeneous charged and an uncharged model membrane was analyzed (Figure 1-35).

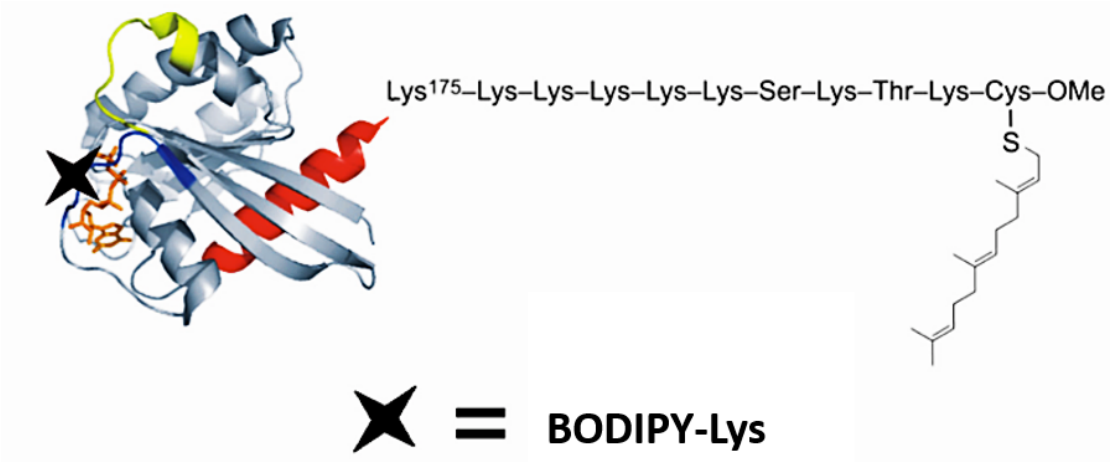

Figure 1-35 Full-length *K*-Ras4B with a BODIPY label in *G*-domain (*89*)

Upon incorporation of negatively charged phosphatidylglycerol lipids into the membrane the protein rotational mobility significantly decreased, suggesting electrostatic interactions between HVR and bilayer play a great role upon membrane binding.

In summary, the lipid anchors in the hypervariable region may target Ras isoforms to specific domains of the plasma membrane. Reliable models for investigation of Ras-membrane interactions are required along with the labels compatible with plasma membrane and do not influencing protein activity. Incompatibility of chosen membrane model with the system under study may lead to unpredictable effects.

1.5 FRET Technique for Studying Lipid Domains

Generally, the experiments involving membrane proteins and lipid membrane domains have limitations due to the size of the objects: they are too small for light microscopy to be visualized. Fluorescence techniques came to aid for these purposes. One example, Förster resonance energy transfer (FRET) technique, will be discussed below.

More than 60 years ago, Theodor Förster described the resonance transfer of optical excitation energy via dipole-dipole interaction (*90*). The mechanism of FRET involves a donor fluorophore in an excited electronic state, which may transfer its excitation energy to a nearby acceptor chromophore in a non-radiative fashion. A pair of molecules that interact in such a manner that FRET occurs is referred to as a donor-acceptor pair.

1.5.1 FRET Principle

In the process of FRET, initially a donor fluorophore absorbs the energy due to the excitation of incident light and transfer the excitation energy to a nearby chromophore, the acceptor, which subsequently emits the energy:

$$D + h\upsilon \rightarrow D^*$$

$$D^* + A \rightarrow D + A^*$$

$$A^* \rightarrow A + h\upsilon,$$

where D=donor, A=acceptor

Figure 1-36 is a Jablonski's diagram illustrating the coupled transitions involved between the donor emission and acceptor absorbance in FRET. In presence of suitable acceptor, the donor fluorophore can transfer its excited state energy directly to the acceptor without emitting a photon.

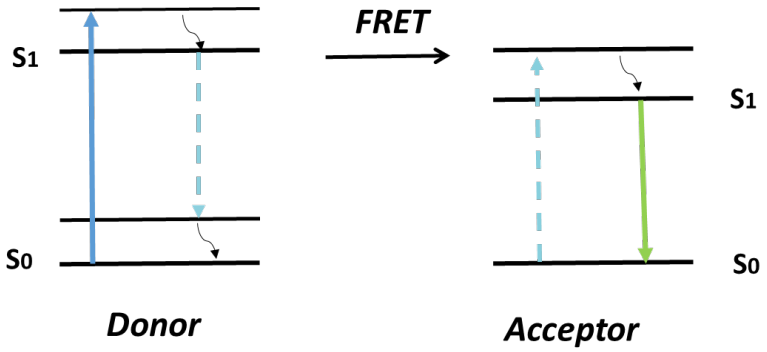

Figure 1-36 Jablonski diagram illustrating the FRET process (*91*)

A few criteria must be satisfied in order for FRET to occur:

- The fluorescence emission spectrum of the donor molecule must overlap the absorption or excitation spectrum of the acceptor chromophore (Figure 1-37). The degree of overlap is referred to as spectral overlap integral;
- The two fluorophores (donor and acceptor) must be in the close proximity to each other (the distance is between 1 to 10 nanometers);
- The fluorescence lifetime of the donor molecule must be of sufficient duration to allow the FRET to occur (*92*).

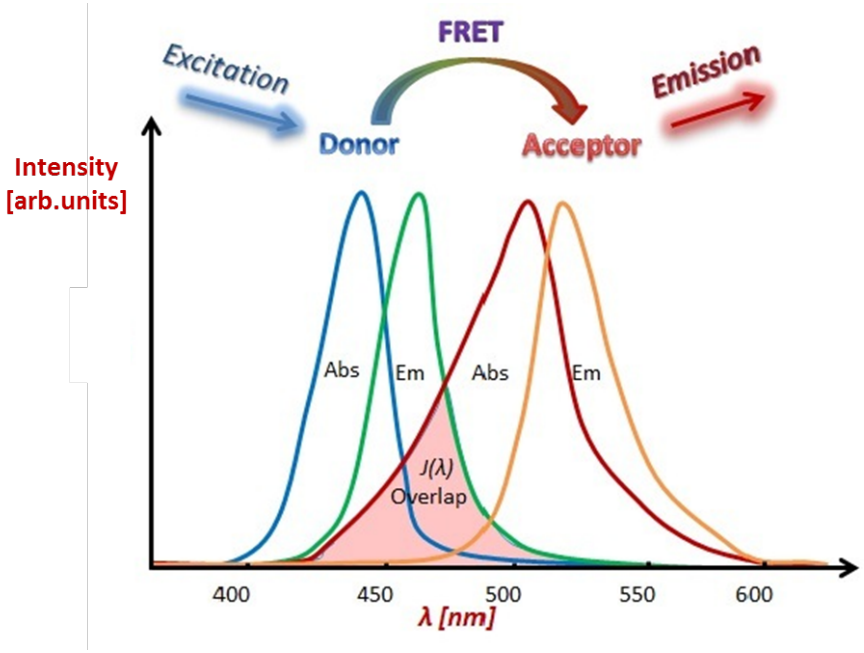

Figure 1-37 Absorption and emission spectra of an ideal FRET pair. Adapted from www.olympusmicro.com.

The efficiency of this energy transfer (E_{FRET}) is inversely proportional to the sixth power of the distance between donor and acceptor (r) making FRET extremely sensitive to small distances:

$$E_{FRET} = \frac{R_0^6}{R_0^6 + r^6}$$

where R_0 is the Förster radius at which 50% of donor excitation energy is transferred to the acceptor (*93*). The Förster radius (R_0) depends on the fluorescence quantum yield of the donor in the absence of acceptor (f_d), the refractive index of the solution (η), the dipole angular orientation of each molecule (K^2) and the spectral overlap integral of the donor-acceptor pair (J) and is given by

$$R_0 = 9.78 \times 10^3 \times (\eta^{-4} \times f_d \times J)^{1/6}$$

One way of measuring the energy transfer efficiency is a steady state measurement of the relative average donor fluorescence intensities in the presence and absence of the acceptor. However, it requires the concentrations of donor and acceptor fluorophores to identical, which may be difficult to achieve in practice.

1.5.2 Determination of FRET from Lifetime Data

Another way to estimate FRET efficiency is to measure a fraction of photons absorbed by the donor that are transferred to the acceptor:

$$E_{FRET} = 1 - \frac{\tau_{DA}}{\tau_D}$$

where τ_{DA} is the donor lifetime in the presence of the acceptor and τ_D is the donor lifetime in the absence of the acceptor. Lifetime measurements allow removing requirement of equal concentration and makes data more comparable.

Function I (t) describes the intensity as a function of the time t, with I_0 as the intensity at the time t = o and τ as the average lifetime of an electron in the first excited state before it returns to the basic state by emitting a photon. This is referred to as the

fluorescence lifetime, the time at which the total intensity drops to 1/e of the initial intensity:

$$I(t) = I_0 e^{-t/\tau}$$

If a mono-exponential decay is not sufficient to adequately describe the data, the equation for multi-exponential decays can be extended:

$$I(t) = I_0 * \sum_n A_n e^{-t/\tau_n}$$

In this equation the A_n represents the relative amplitude of the respective function to the total component, I_0 is the initial intensity of the fluorescence, and τ_n is the lifetime of the respective exponential component.

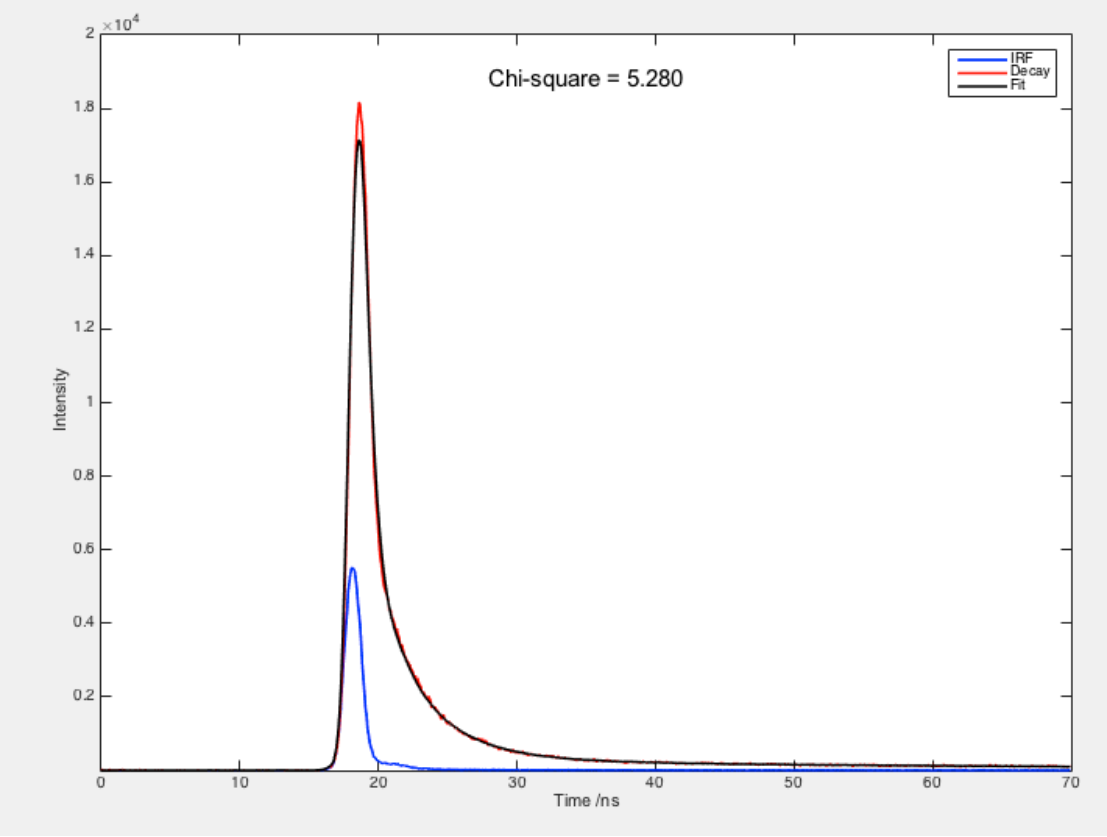

Figure 1-38 Intensity distribution over the arrival times of single photons in an experiment for the lifetime determination. Blue curve is an instrument response function (IRF), red curve is a sample decay function, and black curve is a fitted function

Experimental detection of the fluorescence lifetime is performed by means of the so-called time correlated single photon counting (TCSPC) according to the start-stop method. A pulsed excitation light source is used - a laser or LED with a suitable wavelength - which supplies the start signal for the measurement. The incident photon defines the stop signal, the time between start and stop is measured. After repeating the measurement several times, a histogram is obtained from the distribution of the arrival times of a photon (Figure 1-38).

The fluorescence lifetime can be determined by means of an exponential approximation over the available measured data. It should be noted that the laser pulse has a certain width. This is generally an order of magnitude lower than the fluorescence lifetime but nevertheless long enough to excite molecules after some of the molecules have already returned to the ground state. This leads to a shift of the decay curve R (t) to longer times. The actual fluorescence decay curve F (t) is mixed with the pulse responses of the laser and detector L (t). This shift can be subsequently corrected from the signal. For this purpose, the measured signal R (t) is considered and divided into two possible components: the time profile of the laser including detector L (t) and the actual fluorescence signal of the dye F (t). The time profile of the pulse response of the laser and detector is determined with a scattering solution without fluorescent dyes. The two signal components are linked by a convolution (*91*).

$$R(t) = L(t) * F(t)$$

$$R(t) = \int_0^t L(t^*)F(t - t^*)dt^*$$

The unfolding of the two functions follows a non-differentiable mathematical model. Therefore it has to be solved numerically and the least-squares-fit method is used

as an approximation method. In this case, a measurement signal Rg (t) is generated or estimated. This signal is then compared with the measured signal and the deviation between the two is determined. The comparison takes place via the following rule:

$$\chi^2 = \sum_{i=1}^{n} g_i \, (R(t) - \, R_g(t))^2$$

χ^2 is the measure of the quality of the estimate and g_i is a weighting factor for the quality of the approximation 1 / Ri (t). The process is repeated until χ^2 is between 0.9 and 1.2.

In summary, FRET depends upon the extent of spectral overlap between the donor-acceptor pair, the quantum yield of the donor, the relative orientation of the donor-acceptor and the distance separating the donor and acceptor. As a result, FRET is often referred to as a "spectroscopic ruler", and can be used for a variety of studies, for example, protein-protein interactions, conformational changes of a protein or proteolytic processes.

1.5.3 FRET for Measurement of Size of Membrane Domains

Due to the hydrophobic nature of membrane proteins application of classical approaches is far more challenging than for soluble proteins (*94*). Only a few techniques can be applied, including FRET (*95*) and AFM (*96*). FRET technique is unique among these examples, as it is non-invasive and very sensitive to small concentrations. This is an especially relevant consideration for nanodomains, where even small perturbations might tip the delicate balance of interaction energies and cause significant artifacts in size measurements. This technique can be applied to any molecular system for which a fluorescent derivative can be produced.

Being the native-like component of the plasma membrane of cells, fluorescently labeled lipids are well suited as membrane probes. Depending on the length and saturation of the acyl chains such lipid analogues localize in different lipid domains and called lipid domain markers (*97*). As mentioned above, lipid domains, which coexist in a phospholipid membrane, have different biophysical properties. For example, NBD-DPPE can be used to discriminate liquid ordered domains. In contrast, head group labeled N-rhodamine-DOPE (Rhod-DOPE) shows disordered domain partitioning.

Measuring FRET between two fluorescent membrane probes allows estimation of the membrane domains size. For these experiments, the bilayer is labeled with two membrane probes—with a known preferential enrichment in a certain lipid environment, which forms an adequate FRET-pair (Figure 1-39).

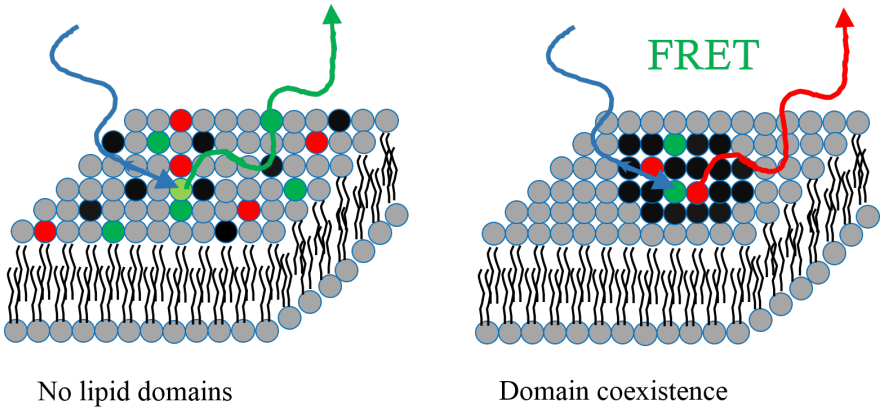

Figure 1-39 Schematic representation of FRET in lipid membrane domains. Left – no lipid domains are present. Right – donor and acceptor located in the same lipid domain, high FRET is observed

As mentioned above, the cellular lipid domains are small on the order of a few nm. Recent studies have shown that in model membranes with realistic plasma membrane lipid compositions, i.e., sphingomyelin/1-palmitoyl,2-oleoyl

phosphatidylcholine/cholesterol (SM/POPC/Cholesterol), Lo domains can produce small domains(*98*). In this case, Lo domains cannot be identified by FRET pairs having a large (~50 Å) donor-acceptor interaction radius (Ro), but may be detected using FRET pairs and short-range quenchers with small (12–25 Å) interaction range (*99*).

One example represented by work of P. Pathak and E. London (*98*). Group used FRET between fluorescent lipids to examine the composition- and temperature-dependent phase behavior of SM/POPC/Cholesterol. FRET is sensitive to changes in the distribution of donor/acceptor distances that accompany phase separation (*100*). Briefly, when a single phase is present, probes are distributed in the bilayer such that FRET efficiency varies only slightly. Relative to this baseline behavior, FRET efficiency changes dramatically upon appearing of regions of phase coexistence, depending on the relative partitioning behavior of the dyes. FRET efficiency is increased in composition regions where both probes prefer the same phase, and reduced where probes prefer different phases (*101*). In this particular work the Ld-preferring probe, Rhod-DOPE (Ld-probe) was used along with NBD-DPPE and DPH, which exhibit significant affinity to ordered domains (*102*).

Figure 1-40 represents the melting profiles of two lipid mixtures: mixture A produced Lo domains due to the presence of sphingomyelin; mixture B represents a fluid homogeneous bilayer (in the absence of sphingomyelin). The emission of the donor was measured through the temperature range for the samples with (F sample) or without acceptors (F_0 samples). Then the ratio of F/F_o was calculated and plotted versus the temperature of the sample.

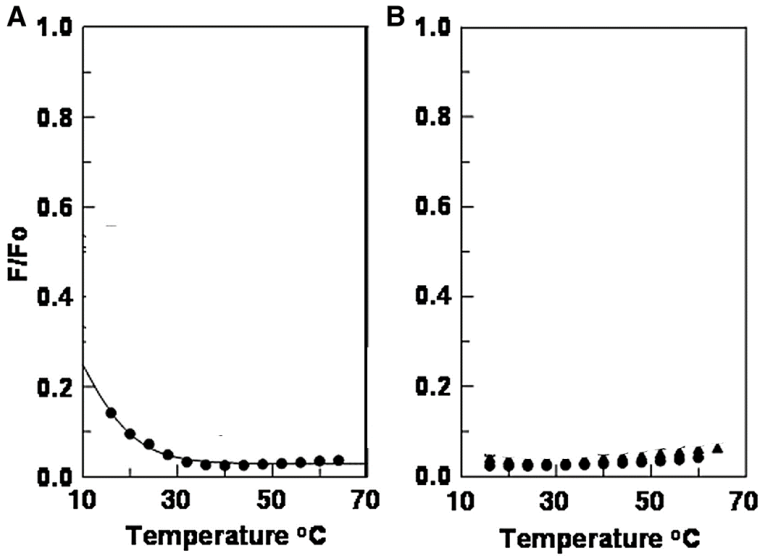

Figure 1-40 Detection of ordered domains by FRET pair NBD/Rhodamine (A) 1:1:1 SM/POPC/cholesterol (raft-containing lipid mixture shows change in FRET upon heating); (B) 2:1 POPC/cholesterol (homogeneous bilayer, no change in FRET) (*98*)

In POPC/Chol vesicles, which lack SM and form homogeneous bilayers FRET was very strong at all temperatures (Figure 1-40, B). In a lipid mixture containing SM lipid domains were detected at low temperature, as shown by the weaker FRET (higher F/F_0) below 30°C (Figure 1-40, A). It is clearly visible that the bilayer becomes homogeneous at a midpoint temperature (melting point) around 32°C, as all Lo domains are gone or small enough to be detected.

FRET ratio changes more dramatically for DPH/Rhodamine FRET pair, which has a shorter Forster distance of 36 Å comparing with NBD/Rhodamine radius of 50 Å (Figure 1-41).

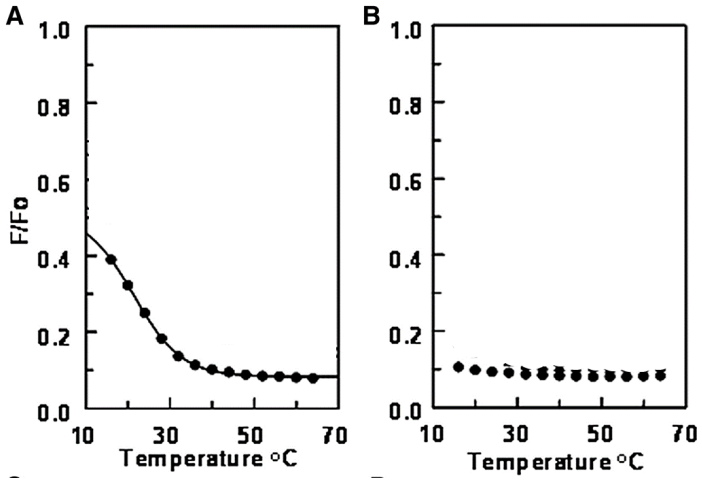

Figure 1-41 Detection of ordered domains by FRET pair DPH/Rhodamine (A) 1:1:1 SM/POPC/cholesterol raft-containing lipid mixture shows change in FRET upon heating), or (B) 2:1 POPC/cholesterol (homogeneous bilayer, no change in FRET) (*98*)

The smaller Lo domains were detected in SM/POPC/Chol at lower temperatures. Using multiple FRET pairs Pathak and London roughly estimated nanodomains size. The limitation of this experiment arises from the size of the domains. Strong protection of a donor inside a domain from acceptor outside the domain requires a Lo domain radius greater than R_0. Therefore, FRET cannot detect domains when domain radius is less than R_0.

In summary, membrane raft size measurements are crucial to understanding the stability and functionality of rafts in cells. The methods, which involve accurately measured raft size, are proposed to identify the interaction mechanism of membrane-coupled proteins.

2. Results and Discussion

The aim of this work was to determine a mechanism by which Ras proteins in different functional state prefer distinct lipid domains. The hypothesis behind this aim is that native partitioning of Ras is determined by concerted interactions of the *G*-domain, *C*-terminal tail and lipid anchors with the membrane domains. To test this hypothesis, we evaluated partitioning of *H*- and *N*-Ras lipoprotein mimics in lipid raft mixtures via FRET to lipid domain markers and assessed the distribution of Ras lipopeptides on lipid raft boundary.

The workflow of this project is schematically represented on Figure 2-1. For creation a model of study – Ras-LUV complex we had to produce and characterize both the protein and a membrane mimic. The membrane mimic (LUV) was characterized by FRET using fluorescence intensity and lifetime-based approaches. In addition, control experiments were performed to analyze interactions of non-lipidated proteins and lipidated peptides with LUV. To create the full-length lipidated protein we performed expression of Ras-181 construct, synthesis of lipidated peptides and coupling reactions.

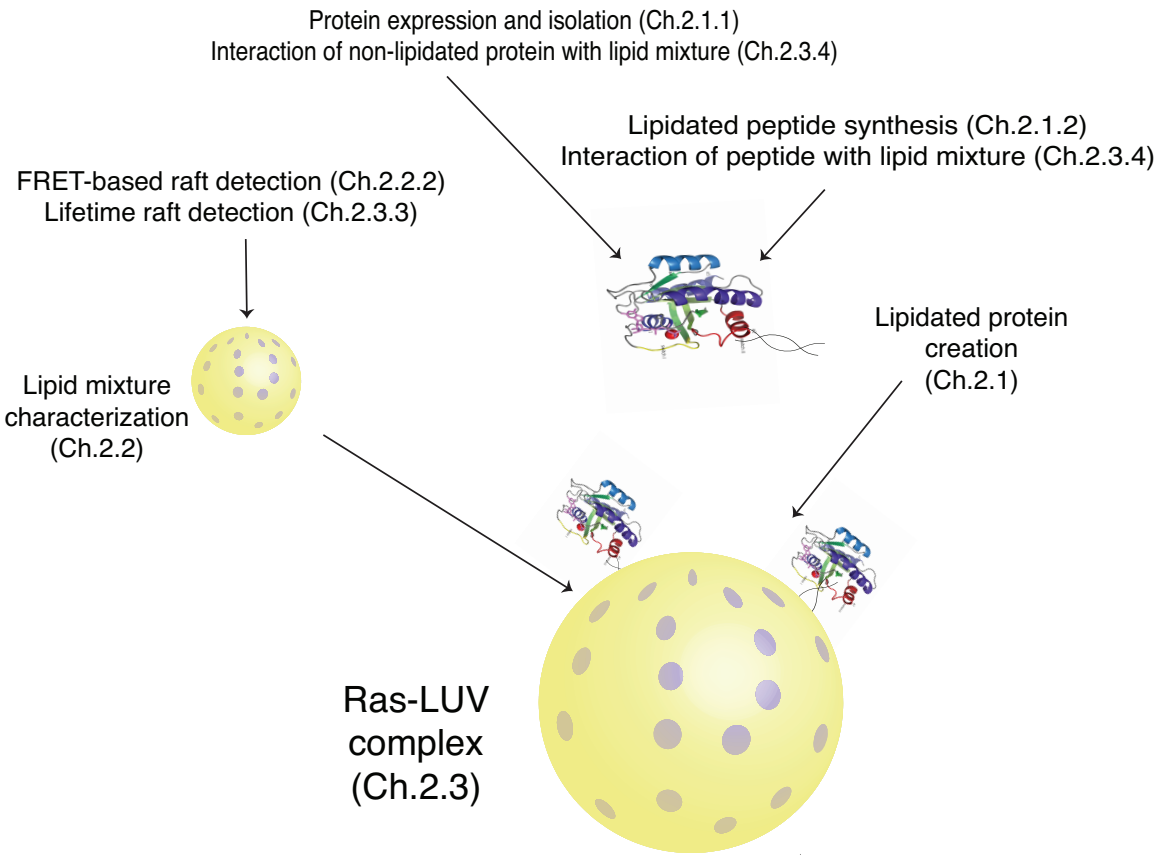

Figure 2-1 Schematic workflow of the project. Number in parenthesis indicates the corresponding chapter of the thesis

In this work, we used recombinant protein expression and chemical synthesis to create lipoprotein mimics and study their mechanism of interaction with the phospholipid membrane. To evaluate partitioning of *H*- and *N*-Ras lipoprotein mimics in lipid raft mixtures via FRET to lipid domain we divided the protein in multiple blocks (Figure 2-2).

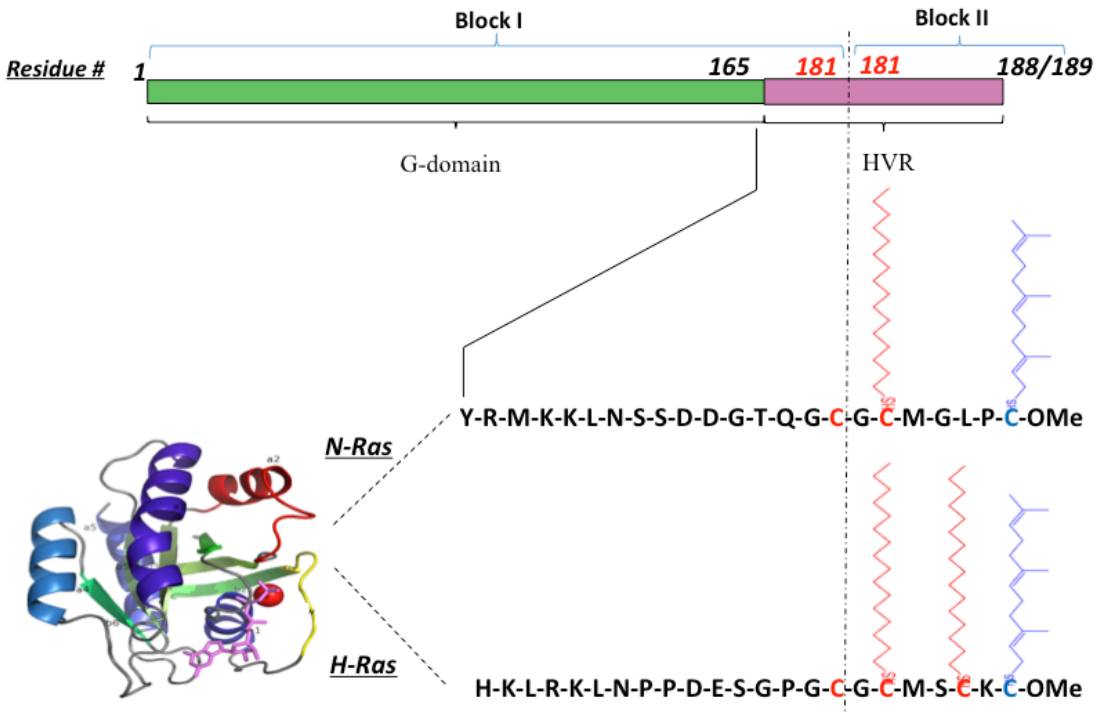

Figure 2-2 Schematic representations of Ras protein blocks used in the experiments: block I is Ras G-domain, block II is lipidated peptide

1. G-domain-containing block I, obtained by bacterial expression using recombinant gene constructs;
2. Labeled lipidated peptides (block II), synthesized by organic chemistry methods.

Using these building blocks, we were able to create three types of constructs:

A. Lipidated peptides lacking *G*-domain
B. *G*-domain lacking membrane-targeting region
C. Semisynthetic full-length protein containing both *G*-domain and lipidated *C*-terminus.

Partitioning of proteins in lipid nanodomains was detected by FRET between the protein construct and lipid domain markers. FRET technique requires having a pair of fluorophores in the sample of interest as well as in lipids serving as markers of lipid

nanodomains. To be able to analyze partitioning of all three constructs, the fluorescent labels have to be introduced in either block I or II.

2.1 Making Lipidated Full-Length Ras Proteins

2.1.1 *G*-Domain-Containing Block I

Taking advantage from the presence of the nucleotide in Ras-binding site, the block I can be labeled by the fluorescent analog of the nucleotide. The fluorescent nucleotide was introduced by the nucleotide exchange reaction, which is driven by large excess of the labeled nucleotide. For the reaction, we used the following truncated proteins constructs:

- *N*-Ras C118S-181
- *H*-Ras C118S -181

2.1.1.1 Expression and Purification of N-Ras C118S-181

The truncation of the *N*-Ras cDNA was achieved by standard PCR methods. Thus, a stop codon was inserted into position 182 of the *N*-Ras cDNA and the resulting PCR product was cloned into an E. coli expression vector (pET43.1b expression vector). Protein expression in the E. coli strain was then carried out, the cells were disrupted and the protein was purified by means of ion exchange chromatography and gel filtration. The expression route is schematically represented on Figure 2-3.

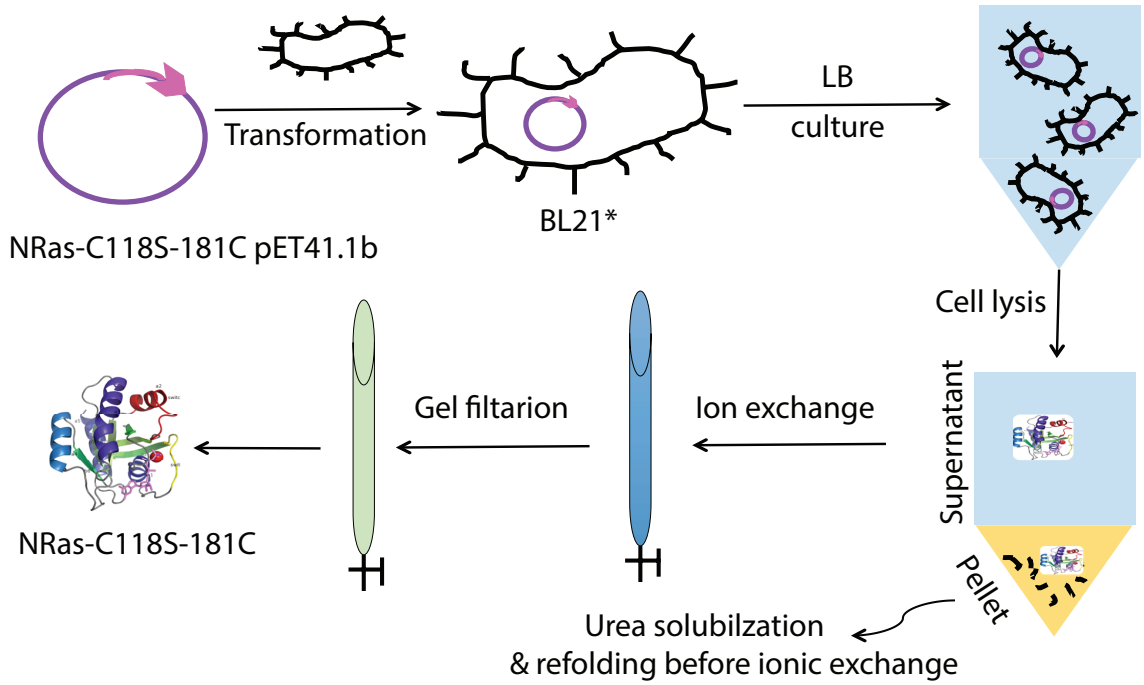

Figure 2-3 Expression and isolation route for *N*-RasC118S-181 construct

We observed a low expression level for the constructs *N*-RasC118S-181 and *N*-RasC118S-181 compared to the short versions Ras-166. One of the reasons is that the protein was split between two fractions. Lysis supernatant and pellet (lanes 6 and 8,Figure 2-4) approximately in 1:1 ratio.

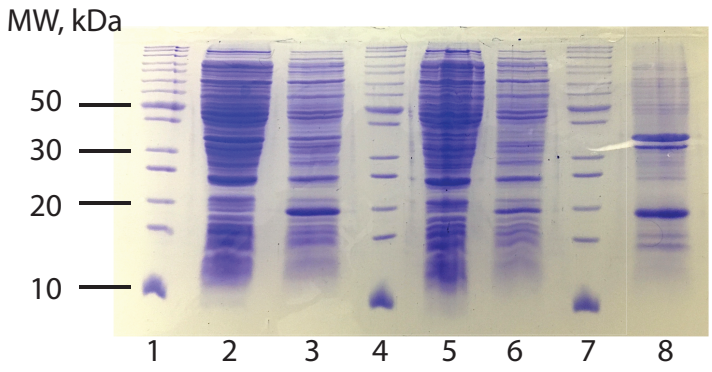

Figure 2-4 SDS-Page analysis of expression and purification of *N*-RasC118S-181 protein. Lanes as follows: 1, 4, 7 – protein ladder; 2 – lysis total without induction; 3 – lysis total after induction with IPTG, 5 – lysis supernatant without induction; 6 – lysis supernatant after induction with IPTG; 8 – urea solubilization

However, we purified and analyzed both fractions. The protein originated from the pellet portion had a superior purity comparing to the supernatant portion (Figure 2-5).

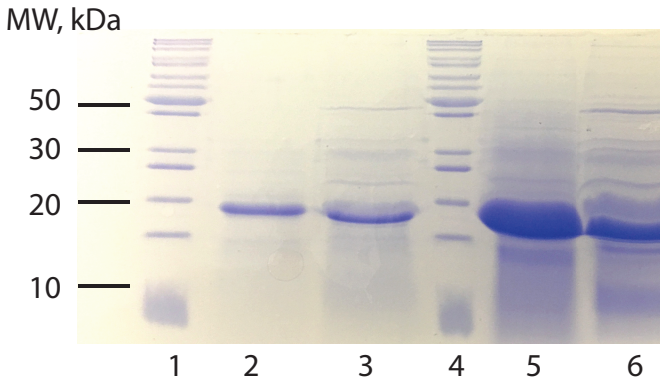

Figure 2-5 SDS analysis of purification of *N*-RasC118S-181 protein. Comparison of fractions originated from lysis supernatant and pellet portions. Lanes as follows: 1, 4 – protein ladder; 2 - pellet fraction; 3 – lysis supernatant fraction; 5 – pellet fraction (overload); 6 – lysis supernatant fraction (overload)

MALDI TOF analysis revealed identical molecular weight of the purified fractions, but we decided to use only pellet protein in coupling reaction. The total yield of the protein originated from the pellet portion was about 2 mg/ 1L of culture media. *H*-Ras was expressed similar way. The total yield for slightly higher, about 4 mg/ 1L of culture media (see Materials and methods for details).

2.1.2 Synthesis of Lipidated Peptides

To study in molecular detail the parameters that determine the selective localization of Ras in plasma membrane we used both labeled and unlabeled lipopeptides. Their synthesis is complicated by the pronounced chemical lability of these compounds. The methods for synthesis and purification were based of solid-phase technique. Using described strategy (*103*), we obtained several compounds:

- Mant-labeled *N*-Ras peptide;
- Mant-labeled *H*-Ras peptide;
- unlabeled *N*-Ras peptide;
- unlabeled *H*-Ras peptide;
- MIC-coupled *N*-Ras peptide;
- MIC-coupled *H*-Ras peptide.

Flexible solid phase approach allows generation of labeled and unlabeled lipidated peptides in one synthetic round. Scheme 2-1 represents the routes for different lipidated peptides based on *N*-Ras *C*-terminal sequence. After introduction of lipid anchors the peptide is elongated according to the amino acid sequence of desired protein. At the last stage, the resin bearing lipidated peptide is split into three portions and each portion is modified by suitable acid derivative. Coupling with mant-acid yields fluorescently labeled peptides. The addition of maleimidocaproyl acid (MIC-acid) leads to the formation of compound, which can be coupled with block I to obtain full-length semi-synthetic protein. Upon capping the amino group with inactive pivalic anhydride the non-fluorescent peptide is produced, which used for experiments on lipid raft size alteration.

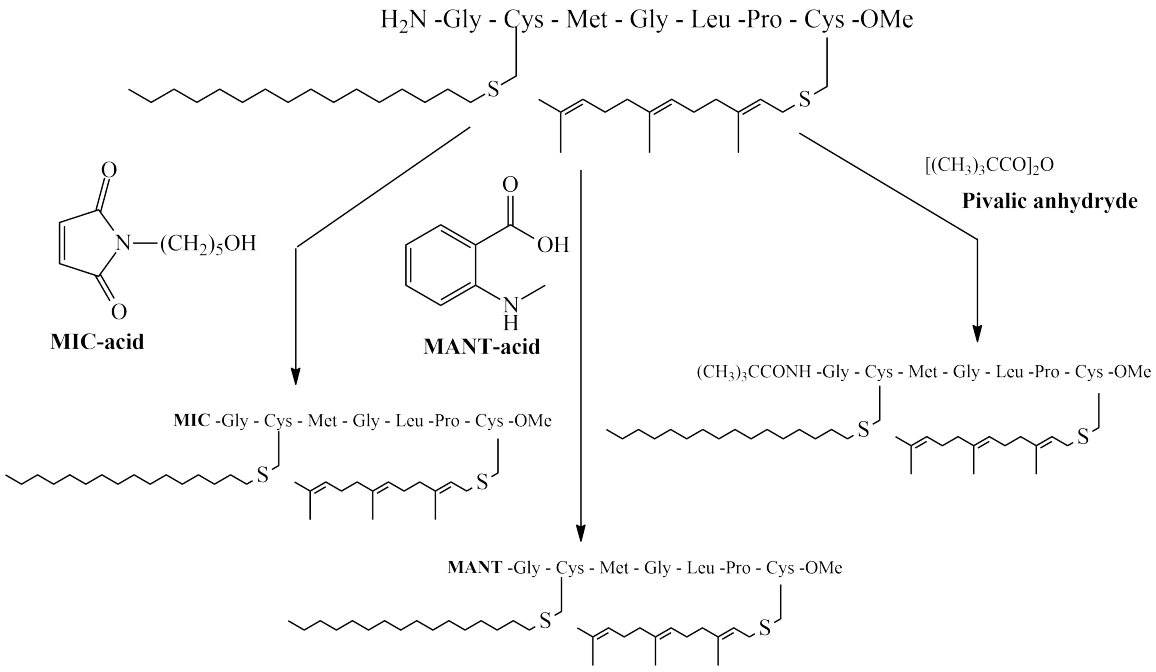

Scheme 2-1 Synthesis of *N*-Ras lipidated peptides

2.1.2.1 Lipidated Peptides for Biophysical Studies with Model Membranes

This part of the work describes the synthesis of lipidated *N*-Ras proteins for biophysical studies on model membranes using fluorescence spectroscopy. The human *N*-Ras protein consists of 186 amino acids and is doubly lipidated at the *C*-terminal hypervariable region: Cys181 is esterified with a palmitic acid and a farnesyl residue is bound to the terminal Cys186 as a thioether. The terminal carboxyl group is protected as a methyl ester (Figure 2-6). The *H*-Ras isoform has additional varieties in hypervariable region: Cys181 and Cys184 are palmitoylated and Cys186 is farnesylated (Figure 2-7).

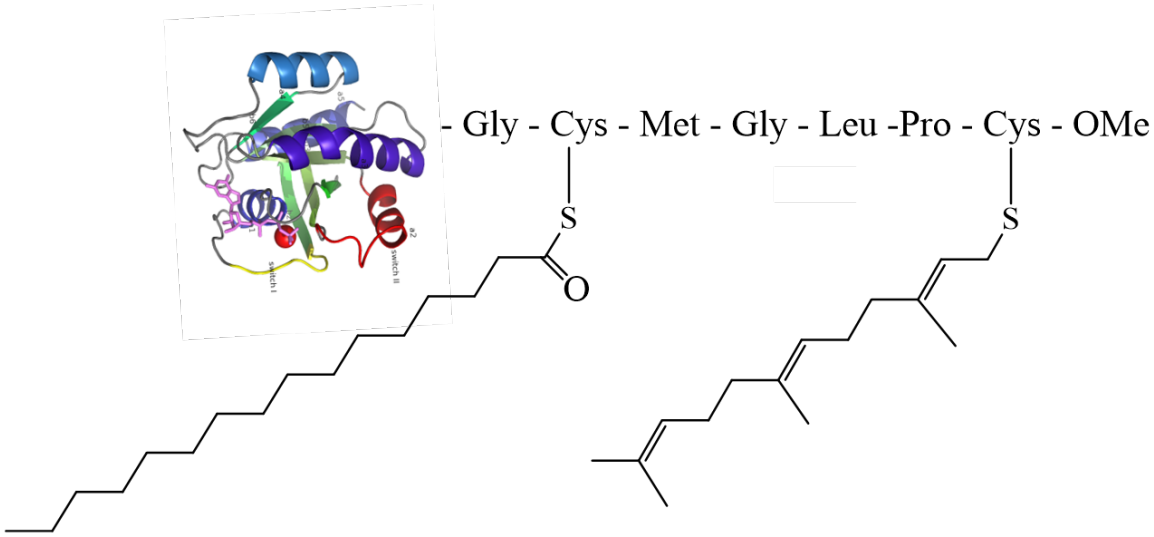

Figure 2-6 Lipidated human *N*-Ras protein. Drawing not to scale

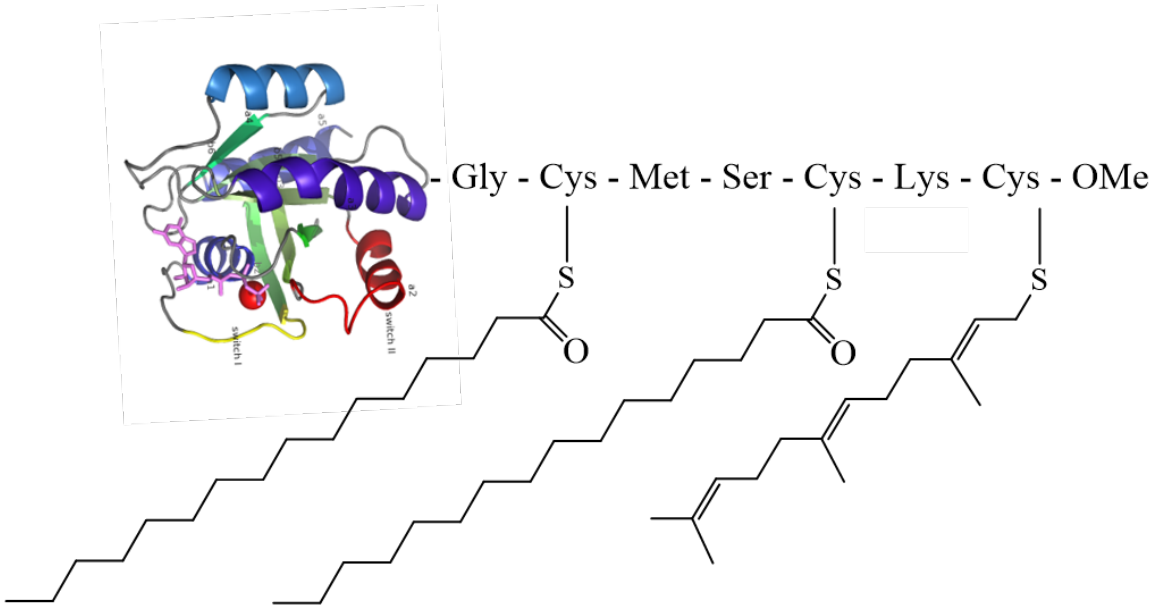

Figure 2-7 Lipidated human *H*-Ras protein. Drawing not to scale

The synthetic route for creation of lipidated proteins must meet the following requirements:

- The strategy should allow introduction of lipid anchors and fluorescent labels

- The linker between the *C*-terminal tail and truncated Ras protein should not affect the biological activity of the protein
- The coupling reaction should proceed with high yields and irreversibly; it should not lead to protein denaturation.

Based on the work of H. Waldmann and colleagues in which lipidated and fluorescently labeled Ras proteins were successfully prepared, we used the same strategy for creation of fully lipidated proteins (*56, 104, 105*). In this approach a *C*-terminal lipidated peptide is synthesized by solid-phase synthesis and coupled to bacterially overexpressed *C*-terminally truncated Ras protein. The maleimidocaproyl (MIC) coupling serves to link the synthetic peptide to the shortened Ras protein (*106*).

The fluorescent label was introduced to *N*-terminal part of the lipopeptide (Mant-peptide). It was shown previously that the peptide backbone for membrane bound *N*-Ras peptides resides outside of the membrane, while the lipid side chains are embedded into the phospholipid layer (*67*). Therefore, such placement of fluorophore ensures that the label does not interact with the membrane, in contrast to a fluorophore introduced into the side chain of amino acids.

Due to the number of limitations related to the instability of lipidated cysteine, the correct choice of the resin linker is crucial. Not so many linkers are suitable in this case. Therefore it is important to choose suitable protective groups and linker. Due to acid-sensitivity of isoprenoid group high concentrations of acid should be avoided, therefore acid-assisted release of the peptide from the solid support is not possible. In addition, the desired peptide has to be methylated at the *C*-terminus, not so many linkers are suitable in

this case. The Fmoc-4-hydrazinobenzoyl linker was chosen for peptide synthesis since it allows direct access to the methyl ester after cleavage (*107*).

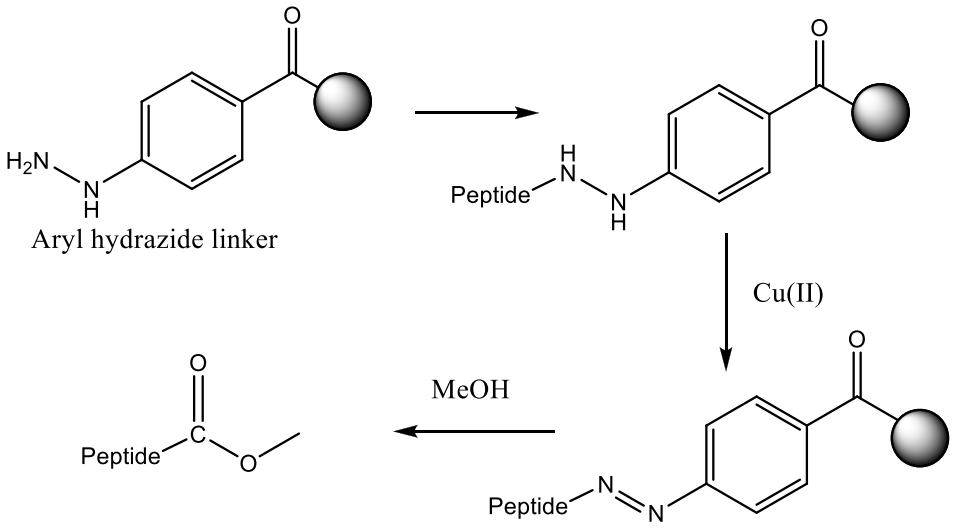

Scheme 2-2 Synthesis of lipidated peptides using the hydrazide linker

The first step is the oxidation of the hydrazine to hydrazide, and then, methanol is used as a nucleophile to release the peptide with a *C*-terminal methyl ester (Scheme 2-2). The only drawback of the hydrazide linker is that it requires the use of degassed solvents and reagents to avoid oxidation before the release of the peptide, which would result in lower yields. The 9-fluorenylmethoxycarbonyl (Fmoc) group was selected as the amine protective group since it can be cleaved under mild basic conditions.

The palmitoyl group is highly reactive towards a nucleophilic attack, and once deprotected, the palmitoyl group can easily undergo an S- to N-acyl shift (Scheme 2-3). Specific methods are required for coupling as well as for the *N*-terminal Fmoc deprotection in order to minimize the formation of side products.

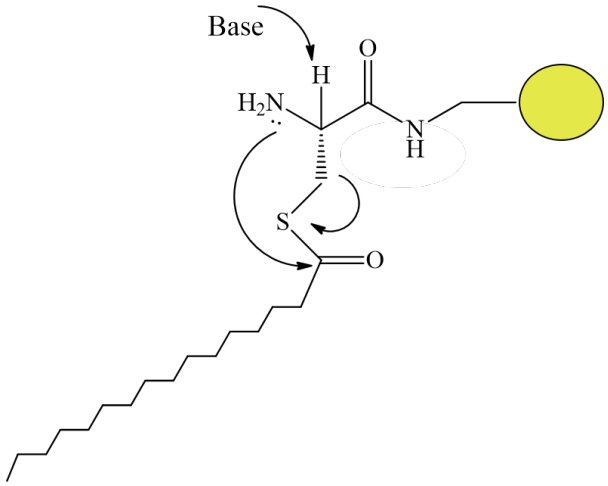

Scheme 2-3 *S,N*-acyl shift scheme

To minimize the possibility off side product formation and avoid difficulties upon handling the lipidated peptide, the palmitoyl group was replaced by its non-hydrolyzable analog hexadecyl lipid chain.

Before starting the synthesis of the lipidated peptides on solid phase, it was necessary to prepare the Fmoc-protected cysteines equipped with the different lipid modifications. The Fmoc protected *N*-fluorenylmethoxycarbonyl-*S*-farnesyl-*L*-cysteine (FmocCys(Far)OH) and *N*-fluorenylmethoxycarbonyl-*S*-hexadecyl-*L*-cysteine (FmocCys(HD)OH) were prepared in solution in good yields after optimization of the syntheses (See Materials and methods for details).

The synthesis with FmocCys(Far)OH was based on the alkylation of the thiol group of the cysteine according to Brown (*108*). In this case, the prenyl chloride in alkaline NH_3/MeOH media was attached to the cysteine. On the second stage, Fmoc-OSu in the presence of triethlyamine in dichloromethane gave the desired Fmoc-protected farnesylated cysteine (Scheme 2-4).

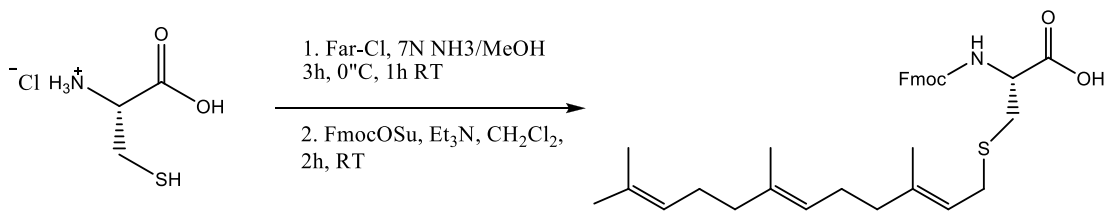

Scheme 2-4 Synthesis of FmocCys(Far)OH

For the synthesis of FmocCys(Pal)OH the SH-protected derivative FmocCys(Trt)OH was used as a starting point. First, the trityl group was removed with 1% TFA in the presence of triethylsilane. The reaction with palmitoyl chloride in the presence of trimethylamine gave palmitoylated cysteine (Scheme 2-5).

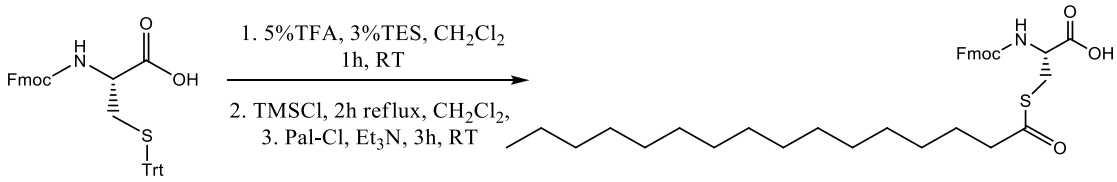

Scheme 2-5 Synthesis of FmocCys(Pal)OH

The FmocCys(HD)OH was obtained by applying a thiol-ene reaction to the deprotected thiol and 1-hexadecene using 2,2'-azobis(2-methylpropionitrile) (AIBN) as a radical initiator Scheme 2-6 (*109*).

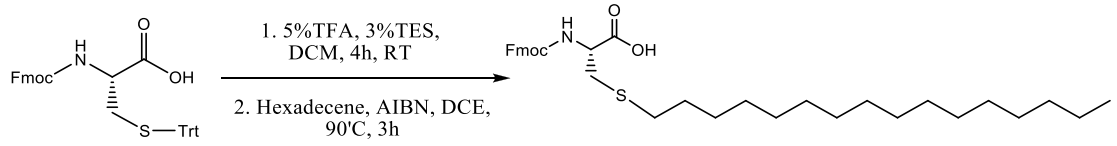

Scheme 2-6 Synthesis of FmocCys(HD)OH

In order to suppress the racemization 2,4,6-trimethylpyridine was used as the base. In each case, 4 equivalents of HBTU / HOBT / TMP were used for the attachment of

cysteine derivatives. The Fmoc groups were cleaved with 20% piperidine in DMF, the chain extension was carried out with activation with HBTU and HOBt. Lipidated building blocks were coupled with HBTU/HOBt and steirically hindered trimethylpyridine (TMP) in DCM/DMF (1:1) to avoid racemization (*110*). The coupling times were extended due to the bulkiness of the lipid residues: five hours for coupling of FmocCys(Far)OH and overnight coupling for FmocCys(HD)OH attachment.

To facilitate the isolation of the final product after each coupling capping procedure was used after each coupling step. To prevent acylation of the nitrogen atoms on hydrazide linker during the capping step the sterically hindered pivalic anhydride was used (*106*). After the hexapeptide was prepared, the terminal amine was deprotected and the polymer-bound peptide was extended with maleimidocaproic acid (MIC-OH) or *N*-methylanthranilic acid (mant-acid). The cleavage of the product from the resin with $Cu(OAc)_2$ in dichloromethane yield the peptides (Scheme 2-7). Same strategy was applied for creation of H-Ras peptides. The presence of Serine and Lysine residues introduced addition challenge. To ensure the side chain active groups of those residues won't be involved into side reactions we used protected derivatives FmocSer(Trt)OH and FmocLys(Mtt)OH. Both Trt and Mtt protective groups can be cleaved under mild conditions with 1% TFA in DCM leaving isoprenyl group intact (Scheme 2-8).

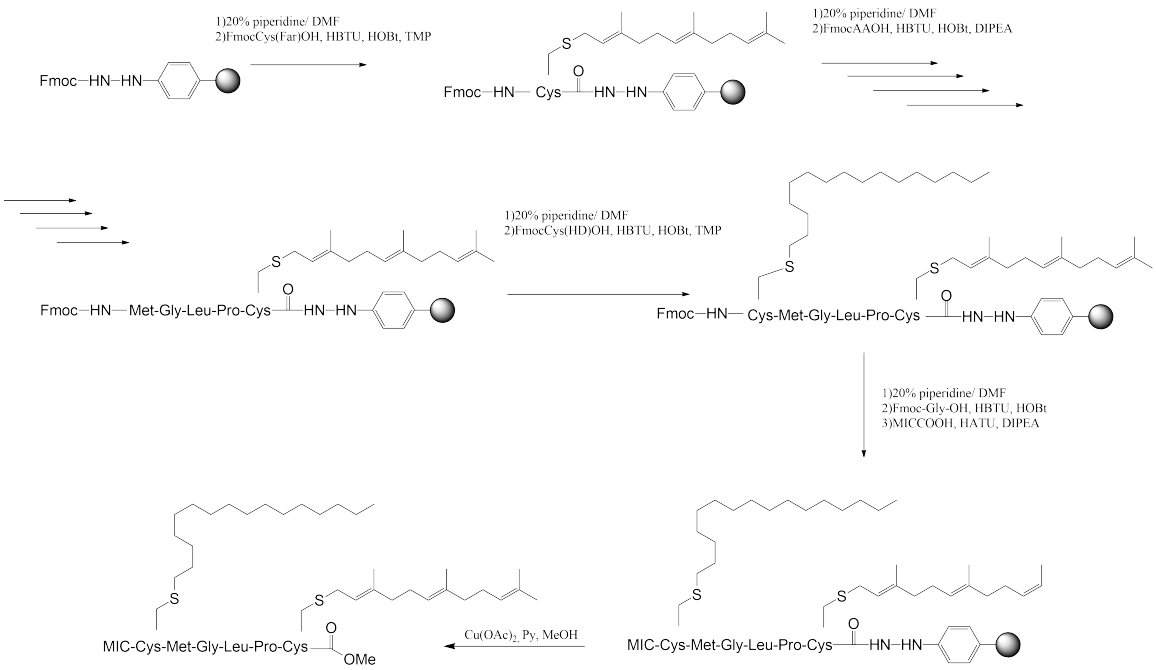

Scheme 2-7 Synthetic scheme for the *N*-Ras peptides

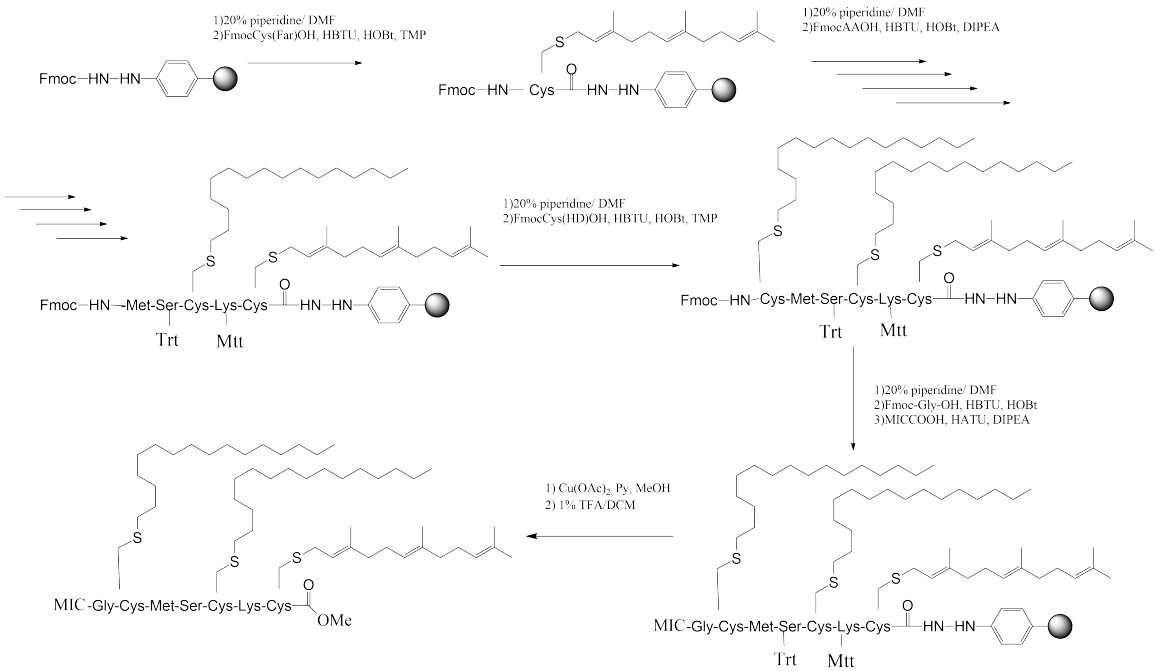

Scheme 2-8 Synthetic scheme for the *H*-Ras peptides

2.1.3 Coupling Reaction

Overexpressed truncated Ras proteins were coupled to *C*-terminal Ras peptides via a maleimidocaproyl linker. The protein polypeptide ends with a free cysteine, which attacks the *N*-terminal maleimidocaproyl group of the lipopeptide in a nucleophilic reaction by the cysteine SH group. The exposed position of the cysteine in the highly flexible *C*-terminus of Ras makes this reaction almost specific. The maleimide group reacts specifically with sulfhydryl groups when the pH of the reaction mixture is between pH 6.5 and 7.5. In addition, cysteine in the protein core was mutated to serine (C118S mutation) to ensure the correct product without significant side reactions.

Two routes for coupling reaction were explored: a) coupling on LUV surface; b) introduction of already lipidated protein into LUV (Figure 2-8). First method seemed to be promising since it ensured attachment of protein to LUV surface (*111*). However, after several attempts we were unable to successfully perform the coupling. One of the possible reasons is that the presence of DOPG lipid adds a negative charge to LUV surface and obstructs the coupling reaction by repelling negatively charged block I construct away from the membrane surface.

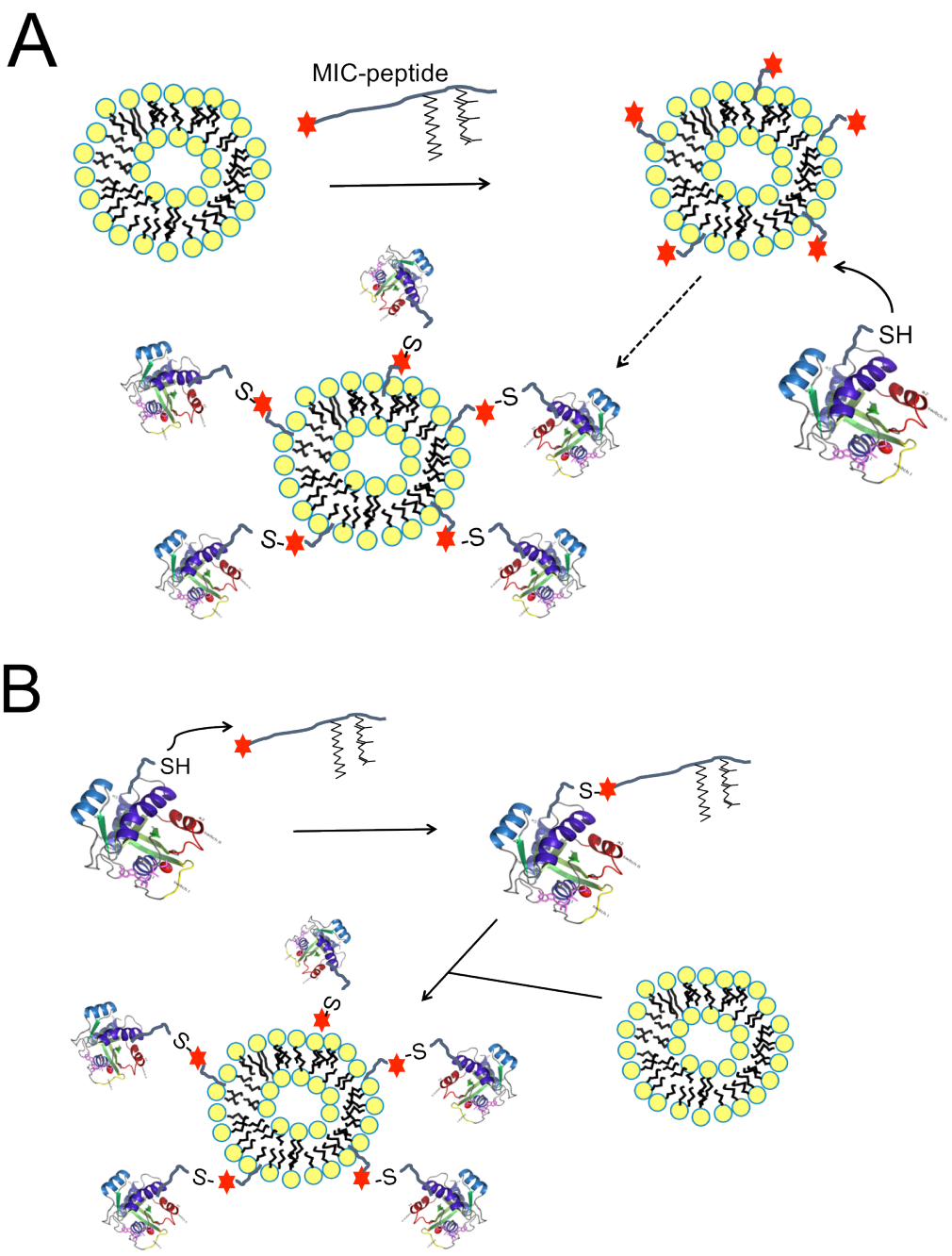

Figure 2-8 Coupling reaction routes: (A) LUV containing MIC-lipidated peptides allowed to interact with RasC118S-181 construct producing protein-LUV complex; (B) coupling reaction between the Ras-181 construct and lipidated peptide followed by addition of obtained lipidated protein to LUV and spontaneous association with the bilayer

Another coupling route required additional steps, as the generation of lipidated proteins and it's purification, followed by introduction of full-length protein into lipid

mimic. The drawback of this route that the lipidated protein would be incorporated into LUVs with low efficiency with certain percentage of protein left in aggregated form in solution. We had to ensure that non-lipidated protein does not react with LUVs.

The coupling of the lipopeptide with the *N*-Ras protein was performed in a Triton X-114-containing Tris buffer for 8 hours at 4° following Bader et al. (*56*). This nonionic detergent made it possible to keep both the lipophilic peptide and the hydrophilic *N*-Ras in solution. The extraction of the obtained lipoproteins could also be easily accomplished with the aid of Triton X-114 (Figure 2-9) since it is miscible with water below 30 ° C, but above this temperature it forms its own hydrophobic phase. Hydrophobic proteins, such as lipoprotein, dissolve in the detergent phase, and uncoupled protein remains in the aqueous phase so that the lipidated protein could be effectively separated. After the phase separation at 37 °C, the coupling product was purified from detergents by Amberlite resin and analyzed by SDS-PAGE and MALDI-TOF (Figure 2-10). Due to the low CMC of Triton X114, it cannot be removed by simple dialysis. Instead, ion-exchange columns are normally used for this purpose. We introduced an effective alternative route for removal of detergent from the reaction mixture using small amounts of Amberlite. Amberlite is ion-exchange resin, which specifically removes detergent from the solution leaving the protein behind. This way of detergent removal is superior comparing to others since a very low amount of the resin has to be added avoiding dilution of the sample.

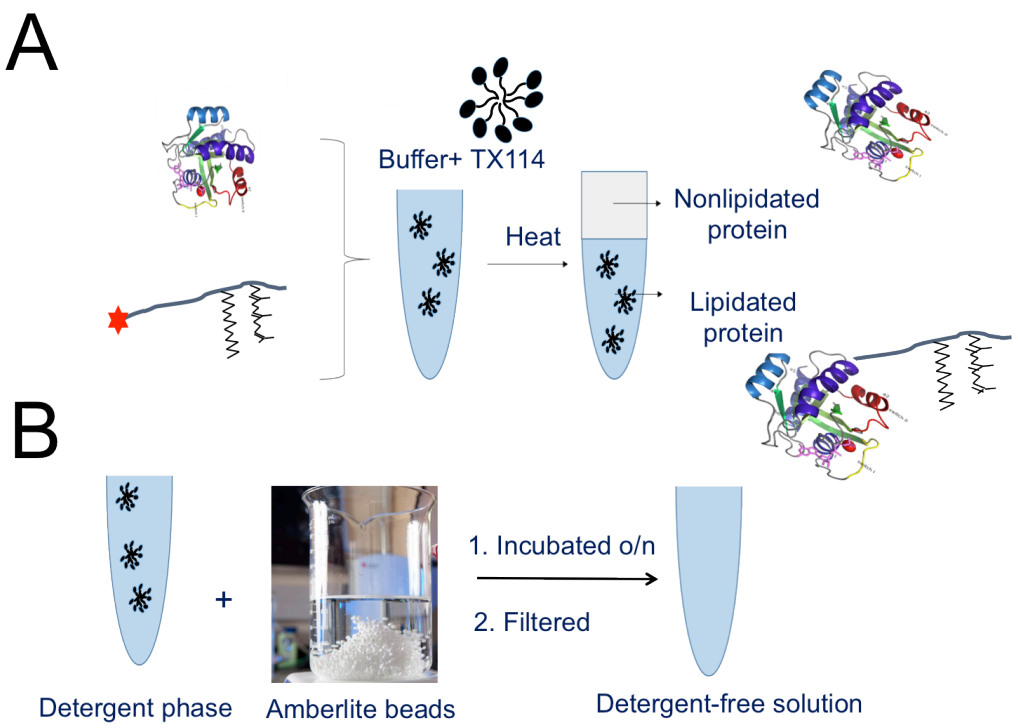

Figure 2-9 A. Separation of the non-lipidated protein from the lipidated one. After heating the mixture separates in two phases: the lipidated protein remains in detergent phase (bottom), non-lipidated protein enriches in aqueous phase (top); B. Detergent removal by Amberlite beads

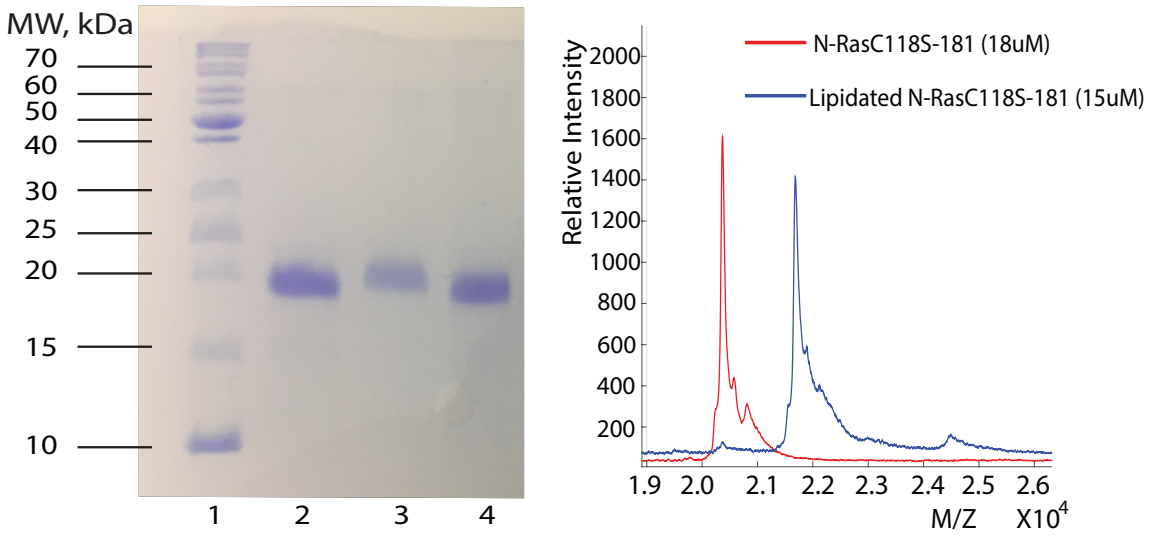

Figure 2-10 Left: SDS-PAGE of the C118S *N*-Ras protein before (lanes 2 and 4) and after conjugation with lipidated peptide (lane 3). Right: MALDI-TOF spectra of C118S *N*-Ras protein before and after conjugation with the lipidated peptide (the difference of the major peaks is 1315 Da)

Similarly the so-called chimera *H*-Ras was obtained and confirmed by MALDI (Figure 2-11). Chimeras are non-natural Ras proteins comprising the *G*-domain of one isoform coupled to the lipidated peptide sequence of another isoform. Chimeras are good tool to probe specific interaction between *G*-domain and HVR playing a role in segregation of protein into specific lipid domains.

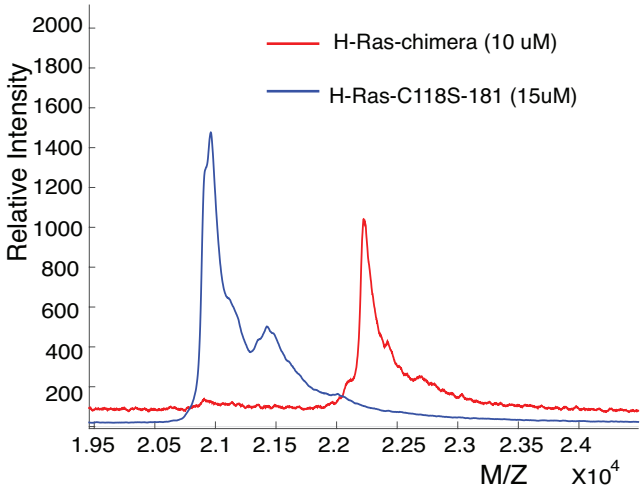

Figure 2-11 MALDI-TOF spectra of C118S *H*-Ras protein before and after conjugation with the lipidated *N*-Ras peptide (the difference of the major peaks is 1315 Da)

2.1.4 Mimicking Two Functional States of Ras

Experiments with samples involving Ras *G*-domain were performed for both GDP and GTP states. It is difficult to work with Ras-GTP due to relatively fast GTP hydrolysis. To mimic Ras-GTP we used its analog – 5'-guanylyl imidodiphosphate GppNHp (Figure 2-12). In this form, one of the oxygen atoms is replaced with amine, producing a slowly hydrolyzable functional group (*112*).

Mant- (Abs/Em = 355/448 nm) and Rhod- (Abs/Em = 460/560 nm) fluorophores exhibit good spectral overlap, which makes them a suitable FRET pair. The mant-guanine

nucleotides Mant-GDP and Mant-GppNHp (Figure 2-12) are commercially available. Using Mant- as a donor offers several advantages. First, the fluorescence quantum yield of Mant fluorophore is relatively high in aqueous solutions, which increases sensitivity of measurements. Second, the Mant-group is relatively small comparing with over fluorescent probes, and does not interfere with the Ras function (*113*).

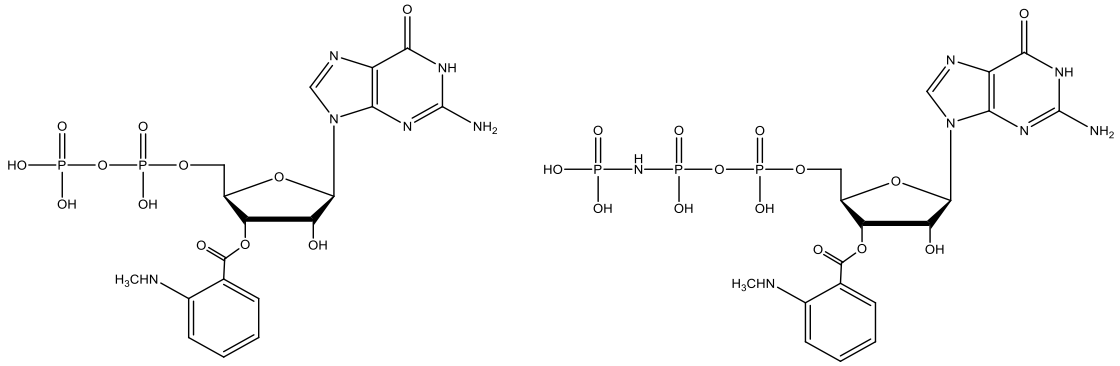

Figure 2-12 Structures of fluorescent nucleotides Mant-GDP and Mant-GppNHp used for labeling of Ras proteins

The 2D fluorescence spectra for mant-GDP and Mant-GppNHp loaded *N*-Ras proteins represented on Figure 2-13.

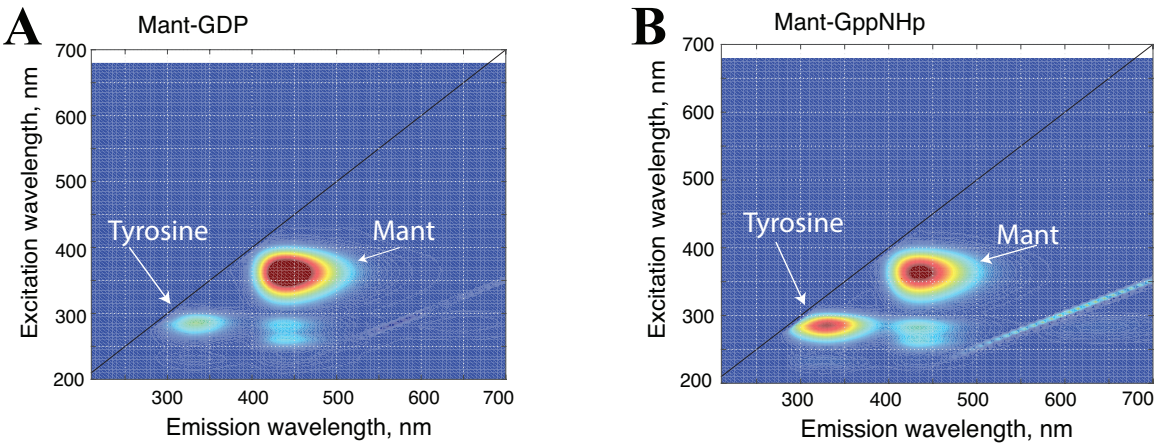

Figure 2-13 2D fluorescence spectra (A) Mant-GDP loaded lipidated *N*-Ras, (B) Mant-GppNHp loaded lipidated *N*-Ras. Tyrosine peak located at ex 280 nm/ em 330nm;mant peak located at ex 360 nm/ em 440 nm

2.2 Making Biologically Relevant Lipid Bilayer

2.2.1 Lipid Domains

Before introduction of the protein we wanted to explore relative affinity of Ras to lipid nanodomains we used two types of lipid mixtures for each set of the experiments:

- homogeneous non-raft mixture (POPC/DOPG);
- lipid raft-containing mixture: SM/POPC/Cholesterol;

Homogeneous mixture served as a control for experiments with raft-containing mixtures. It contained 2% of negatively charged DOPG lipids to mimic the inner membrane leaflet, where Ras proteins reside. The raft mixture was also negatively charged due to the presence of 2% Rhod-DOPE. Type 2 lipid mixtures exhibit nanodomains of ~7 nm radius (Figure 2-14) (*98*).

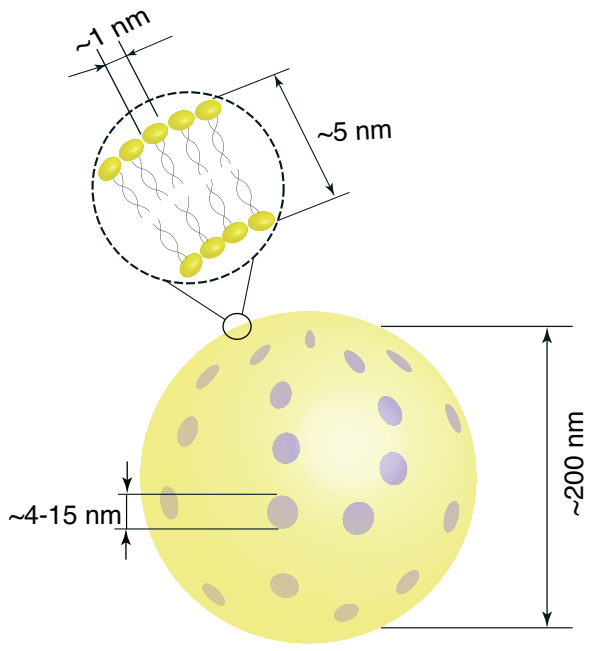

Figure 2-14 A schematic drawing of lipid vesicle and nano-scale raft domains (approximately to scale)

2.2.2 FRET-Based Detection of Lipid Nanodomains

The ternary lipid mixture SM/POPC/Cholesterol was shown to have phase separation and often called canonical model raft mixture. The POPC forms a liquid disordered (Ld) phase, whereas SM/Chol mixtures with a molar ratio close to 1:1 form a liquid-ordered (Lo) phase (*114*). As seen on tertiary diagram (Figure 2-15) there is a broad phase coexistence area at room temperature, however the exact location, shape, and boundaries of the Ld/Lo coexistence region appear to vary with the method of observation (*115*).

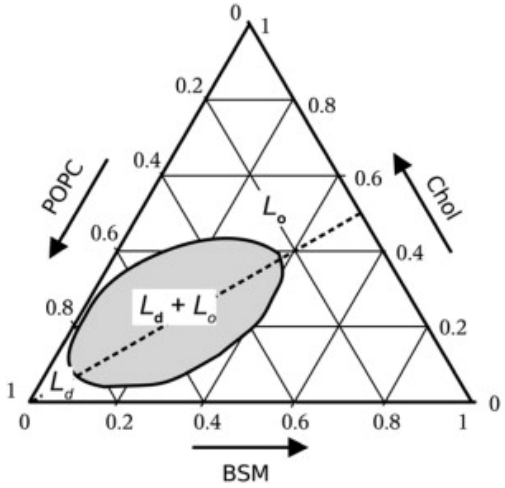

Figure 2-15 Simplified phase diagram for a ternary mixture of SM/Cholesterol/POPC at 25°C (*115*). The coexistence of Lo and Ld phases shown in gray

To detect the presence of nanodomains we used methodology described by Pathak and London (*98*). In our study, we examined eSM/Chol/POPC (egg sphingomyelin was used instead of bovine) system utilizing fluorescence resonance energy transfer (FRET) between DPH (donor; partitions evenly between ordered and disordered domains) and Rhod-DOPE (acceptor; partitions strongly into Ld domains). An effective R_0 of this pair

is 36 Å (*102, 116*). The simplest way to measure FRET is by calculation of the ratio of donor fluorescence intensities F/F_0, where F sample contains both donor and acceptor, and F_0 sample contains only donor.

The principle of FRET-based detection of lipid nanodomains is illustrated in the Figure 2-16. The purple shape represent lipid raft. Red spheres represent FRET acceptors (Rhod-DOPE) and green spheres represent FRET donors (DPH). The significant energy transfer is expected when an acceptor is within the radius R_0 of a donor.

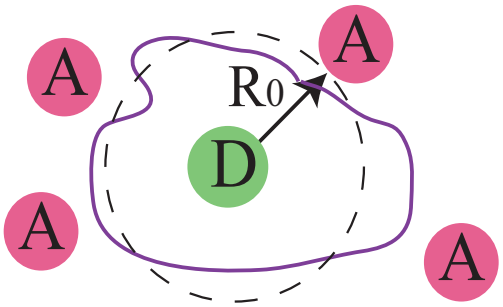

Figure 2-16 Schematic representation of the lipid probes segregation into phases. D is a donor, A is an acceptor. R_0 is an effective distance at which 50% of the donor fluorescence is transferred to an acceptor

One difficulty of domain detection arises from temperature dependence of the domain's size. At low temperatures, the liquid –ordered (Lo) domains are relatively large. As the temperature is increased, these domains become smaller, and at 37˚C segregated domains typically are no longer detectable by given donor/acceptor pair (with R_0'). However, it is possible to detect inhomogeneities on shorter distance scales by another FRET pair (with $R_0'' < R_0'$) (Figure 2-17). These nanodomains may be more relevant to biological membranes than the larger domains formed at lower temperatures.

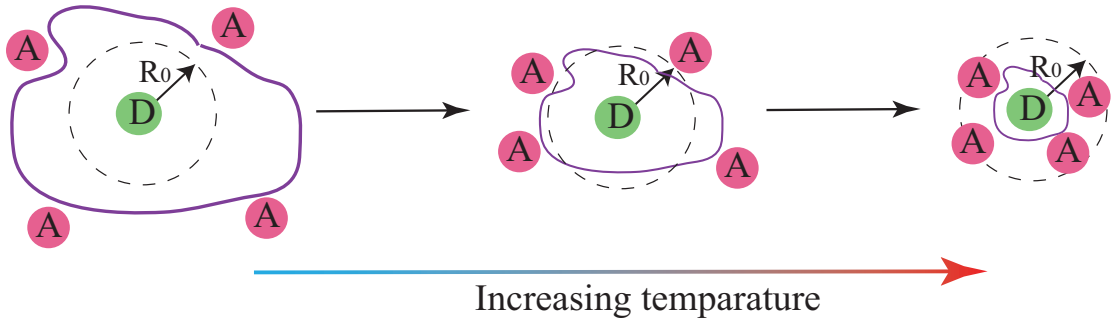

Figure 2-17 The size of lipid rafts decreases upon melting. The actual size of lipid raft is not detectable after certain point for the particular FRET pair since R_0 is greater than the size of the domain

LUVs were prepared by mixing of bulk lipids (SM/POPC/Chol) and addition of donor only (F_0) or donor and acceptor lipids (F) (see Materials and methods for details, Chapter 4.16). Two F_0 samples and two F samples were heated (or cooled) simultaneously with a rate 0.5°C /min and the intensity of both dyes were detected. The FRET measurements were repeated 4 times for each F_0 and F samples, and the final F/F_0 ratio was calculated by averaging. Excitation of DPH in the presence of Rhod-DOPE within a distance comparable to R_0 (or shorter) resulted in a decrease in DPH emission, indicating that energy transfer had taken place.

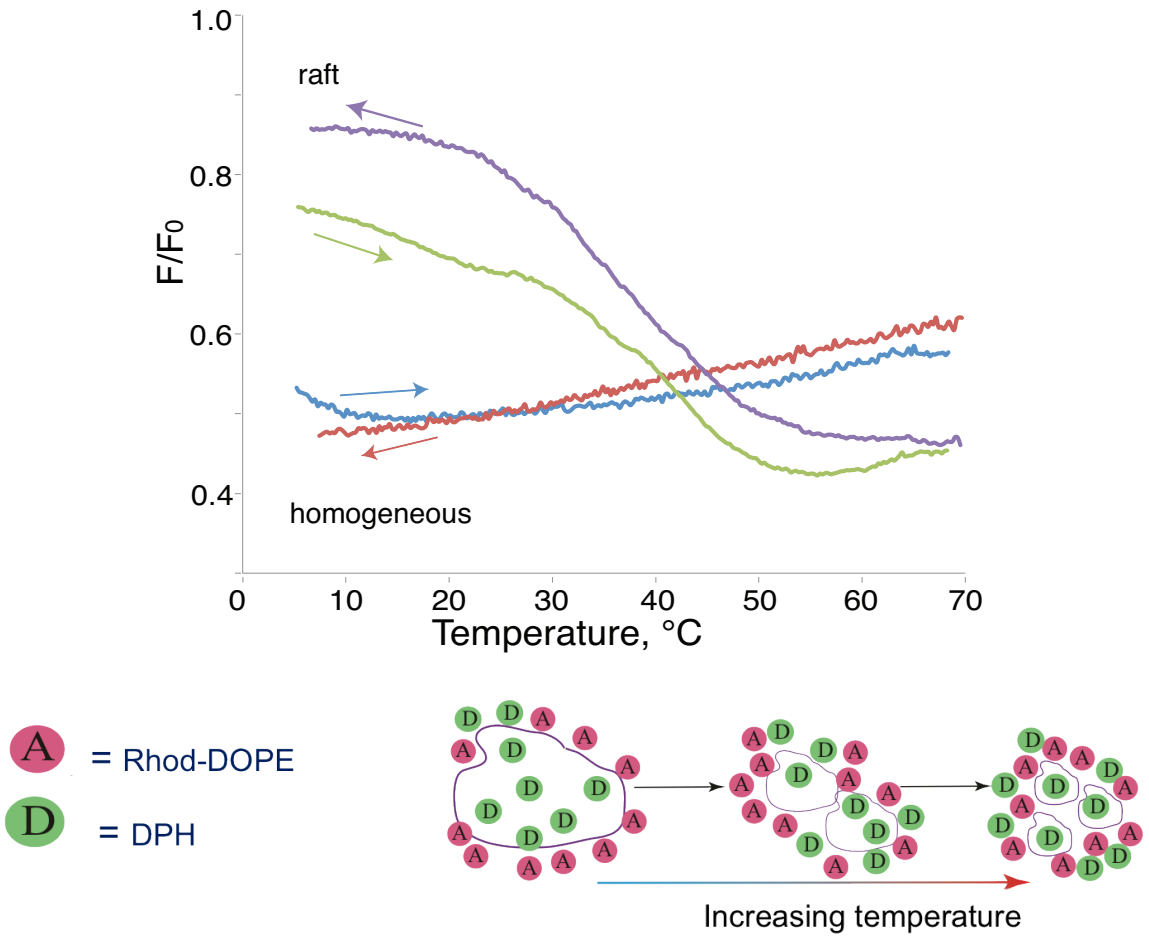

Figure 2-18 Top: Presence of rafts in SM/POPC/cholesterol lipid bilayers detected by FRET between lipid domain markers. Heating and cooling profiles of the homogeneous and raft LUV solutions with the DPH (0.1% mol) and Rhod-DOPE (2% mol) donor/acceptor pair at a scan rate of 0.5 °C/min. Each curve is an average of two independent samples. Fluorescence intensity ratio, F/F_0, is calculated using DPH emission of F and F_0 samples, containing and lacking Rhod-DOPE, respectively. Bottom: schematic representation of distribution of donors and acceptors in raft-containing samples upon heating

Figure 2-18 shows F/F_0 versus temperature of the samples upon heating and cooling of the samples. Similarity of heating and cooling profiles confirmed reversibility of phase transitions in the raft bilayer and relative photostability of the fluorophores. Homogeneous bilayer (red and blue) did not reveal dramatic changes in F/F_0 as anticipated. Reduced FRET at low temperature (high F/F_0 value) in raft samples (green and purple) reflects segregation of donor and acceptors in different lipid phases. As temperature was increasing to 40°C the domains were melting, leading to increasing

FRET (reduced segregation). After approximately 45°C the bilayer was homogeneous, no phase coexistence was detected, which is in agreement with literature data (*117*).

2.2.3 Microscopy of Supported Lipid Bilayers

To verify that the lipid-raft mixture creates nano-scopic (not microscopic) domains, we made a supported bilayer using the lipid raft mixture and observed them in a confocal microscope. The spreading of small lipid vesicles on hydrophilic solid supports, pioneered by McConnell et al. (*118*), is a simple route to form supported lipid bilayers (SLBs) (Figure 2-19).

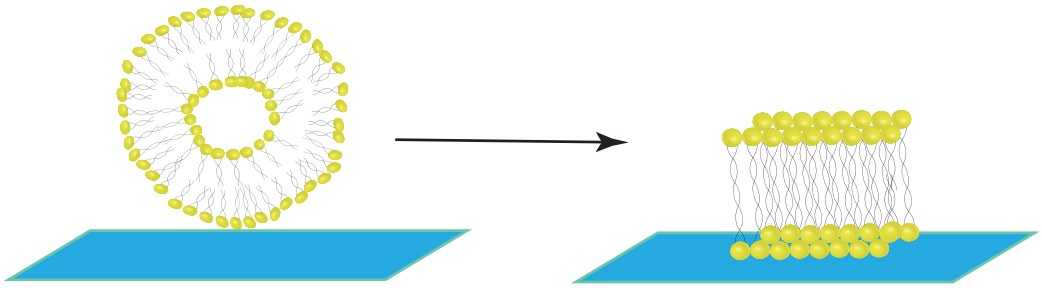

Figure 2-19 Formation of supported bilayer on glass from LUVs: LUV solution in a buffer is spread on acid-treated glass surface producing a supported lipid bilayer

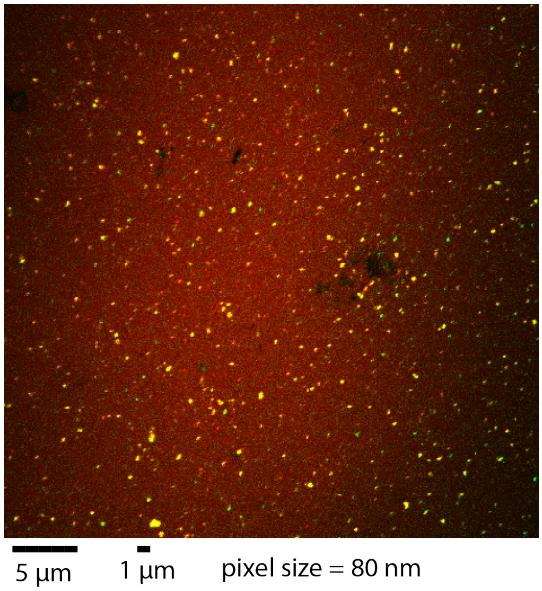

Figure 2-20 Overlay of images of NBD-DPPE fluorescence (green) and Rhod-DOPE fluorescence (red) in supported lipid bilayers made of raft lipid mix. Bright yellow spots correspond to aggregated LUV that were not removed during the wash phase

In a supported lipid bilayer mixture instead of DPH we used NBD-DPPE fluorescent lipid, a lipid raft marker. Figure 2-20 reveals that on a microscopic scale the lipid bilayer appears homogeneous; no separated domains were visible, suggesting that the domains size is well below the limit of resolution of the microscope (~ 200nm). Therefore, confocal microscopy of LUVs supported the absence of domains in SM/POPC/Chol lipid mixture, yet Figure 2-18 shows the melting profile, which confirms the coexistence of two phases. Taken together these results imply that raft domain size is, indeed, nano-scopic.

2.3 Protein-Lipid Interactions

2.3.1 Preferential Localization of *C*-Terminal Lipopeptides

To reveal a contribution of the lipidated *C*-terminus of Ras to interactions with lipid rafts, we evaluated the preferential localization of *N*-Ras *C*-terminal lipopeptide in absence of the *G* domain. *N*-methylanthranyl group (mant) was attached to the lipopeptide *N*-terminus to serve as a donor fluorophore. Spectral properties of mant are comparable to DPH, therefore, we expected a similar Förster radius and similar sensitivity to domain localization.

Heating and cooling profiles of F/F_0 for mant-lipopeptide (Figure 2-21) revealed a pattern, which was opposite to the one observed for DPH in Figure 2-18. Instead of an initial high F/F_0 values indicative of low FRET due to segregation of acceptors from donors, we observed a lower initial F/F_0 values implying co-localization of mant-lipopeptide with Rhod-DOPE. Heating lead to increasing F/F_0, indicating the reduction of the FRET efficiency at higher temperatures, which may be explained by dilution of fluorophores due to melting of rafts (*119*).

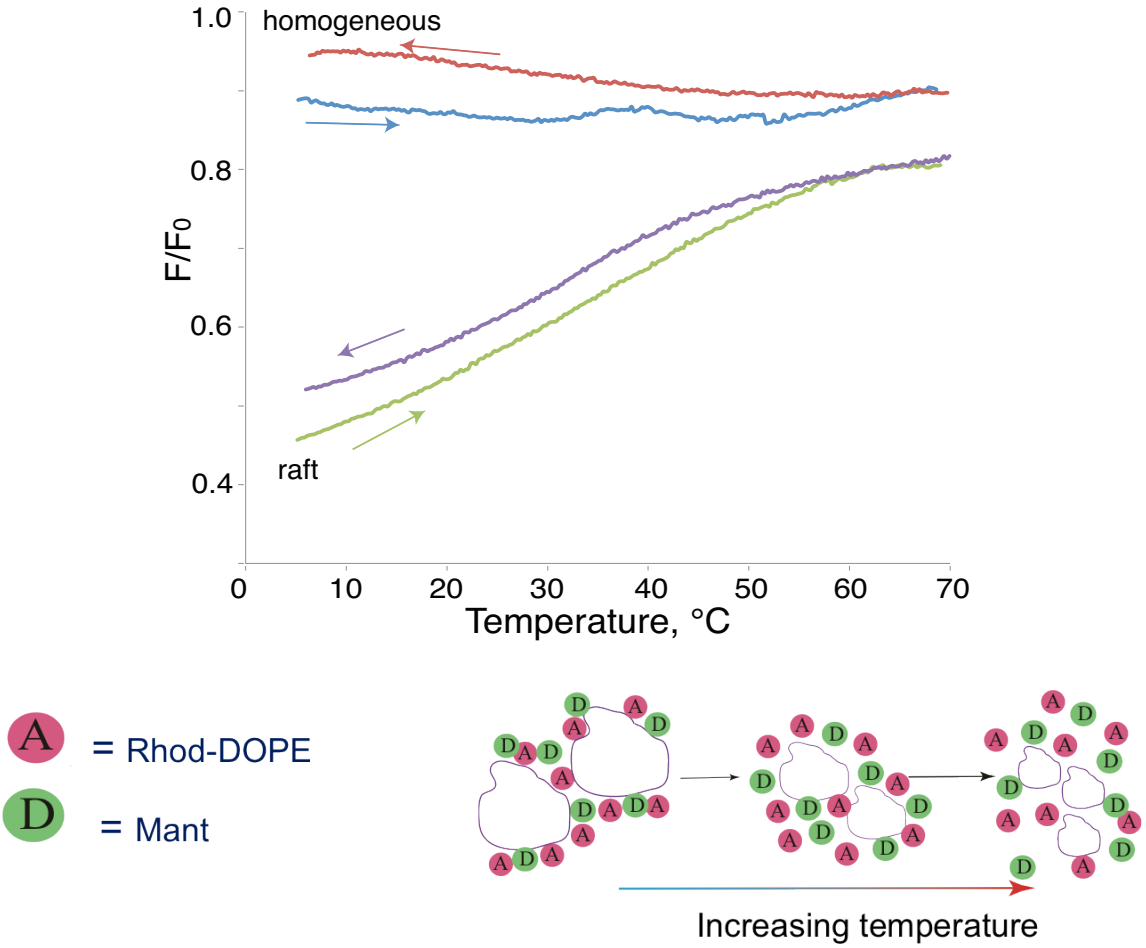

Figure 2-21 Top: Non-raft localization of *N*-Ras *C*-terminal lipopeptide revealed by FRET to the disordered domain marker. Heating and cooling profiles of the homogeneous and raft LUV with Rhod-DOPE (acceptor; 2% mol) in the presence of the mant-labeled *N*-Ras *C*-terminal lipopeptide (donor; 0.1% mol). Fluorescence intensity ratio, F/F_0, was calculated using mant emission of F and F_0 samples, containing and lacking Rhod-DOPE, respectively. Each curve is an average of two independent samples. The F/F_0 curves for homogeneous LUV show unexpectedly high (yet relatively constant) values reflecting difficulties with quantitative subtraction of light scattering caused by LUV; Bottom: schematic representation of distribution of donors and acceptors in raft-containing samples upon heating

To confirm this interpretation, we used another lipid domain marker 1,2-dioleolyl-sn-glycero-3-phosphoethanolamine-N-5-dimethylamino-1-naphthalenesulfonyl (Dansyl-DOPE) and recorded the temperature dependence of F/F_0 for dansyl group fluorescence (Figure 2-22). Dansyl-DOPE is localized in a disordered lipid phase due its unsaturated lipid chains. A similar increasing trend in the temperature dependence of F/F_0 values was

observed confirming localization of mant-labeled lipopeptide to the non-raft disordered lipid phase.

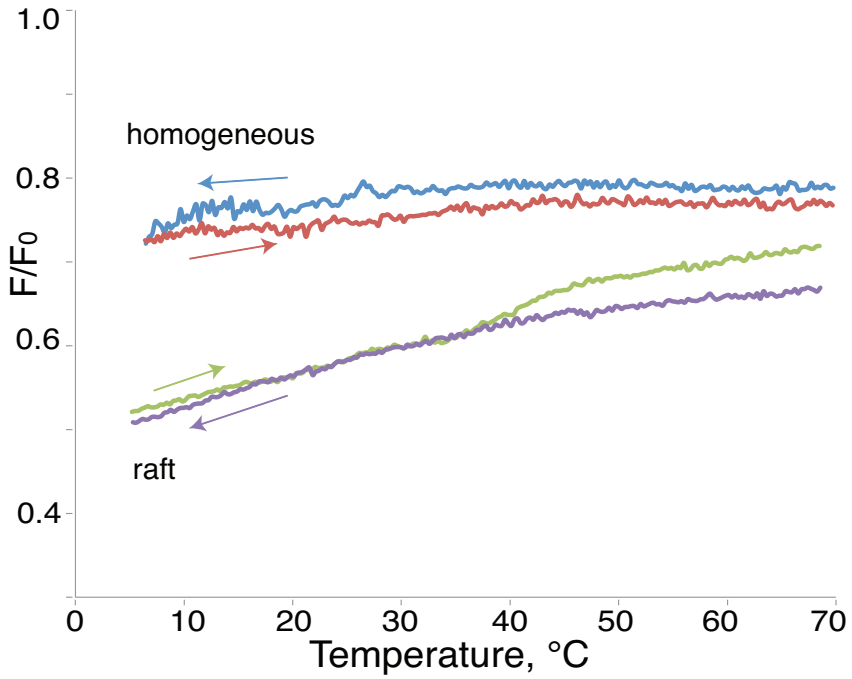

Figure 2-22 Disordered domain markers demonstrate increasing FRET upon reduction in raft size. F/F_0 temperature dependence for Dansyl-DOPE donor (0.1% mol) incorporated into the homogeneous and raft-containing lipid bilayers containing Rhod-DOPE (2% mol)

Similar experiment was done for mant-labeled *H*-Ras lipidated peptide (Figure 2-23). *H*-Ras has an additional palmitoyl lipid anchor, believed to increase Ras affinity to lipid rafts. In spite of the presence of the third lipid anchor in the structure of *H*-Ras membrane targeting region similar co-localization of mant-*H*-Ras-lipopeptide with Rhod-DOPE was observed.

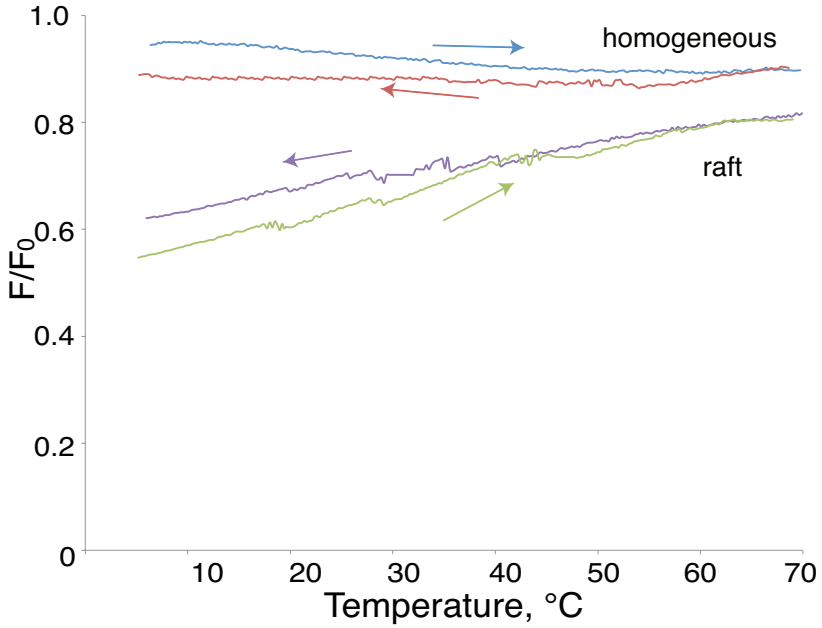

Figure 2-23 Non-raft localization of *H*-Ras *C*-terminal lipopeptide revealed by FRET to the disordered domain marker. Heating and cooling profiles of the homogeneous and raft LUV with Rhod-DOPE (acceptor; 2% mol) in the presence of the mant-labeled *H*-Ras *C*-terminal lipopeptide (donor; 0.1% mol). Each curve is an average of two independent samples

2.3.2 Effect of Lipopeptides on Lipid Raft Formation

Experiments with mant-lipopeptide revealed that the lipopeptide is localized in vicinity of the acceptor fluorophore, Rhod-DOPE. However, we could not distinguish between the two possibilities: (1) lipopeptide uniformly distributed in the disordered lipid phase, and (2) lipopeptide concentrated at the boundary of the raft domains. Both localizations were observed in experiments with different lipid mixtures (*69*) (*120*). In both cases, mant fluorophore will be easily accessible for quenching by rhodamine.

Boundary localization of the lipopeptide may be directly tested by evaluation of stability of lipid rafts in the presence of different concentrations of the lipopeptide. The key consideration is that if the additive is attracted to the lipid phase boundary, the boundary is stabilized (line tension is reduced) (*121*). In other words, the lipopeptide will

act as a lineactant and will facilitate breaking the existing rafts into smaller ones to increase the length of the boundary. The reduction in raft size may be detectable in FRET experiments because DPH will be more effectively quenched by Rhod-DOPE when rafts become comparable or smaller than the Forster radius for this FRET pair.

Figure 2-24 shows the heating profiles for raft LUV containing increasing concentration of the lipopeptide (no fluorophore attached; see Supporting Information for estimates of the lipopeptide density at the raft boundary). The reduction in F/F_0 values upon heating was associated with melting of lipid rafts. Lipid rafts were not affected by presence of the lipopeptide as judged by similar sigmoidal patterns of the samples with 0%, 0.1%, and 0.5% of lipidated *N*-Ras peptide. This observation questions boundary localization of the lipidated peptide.

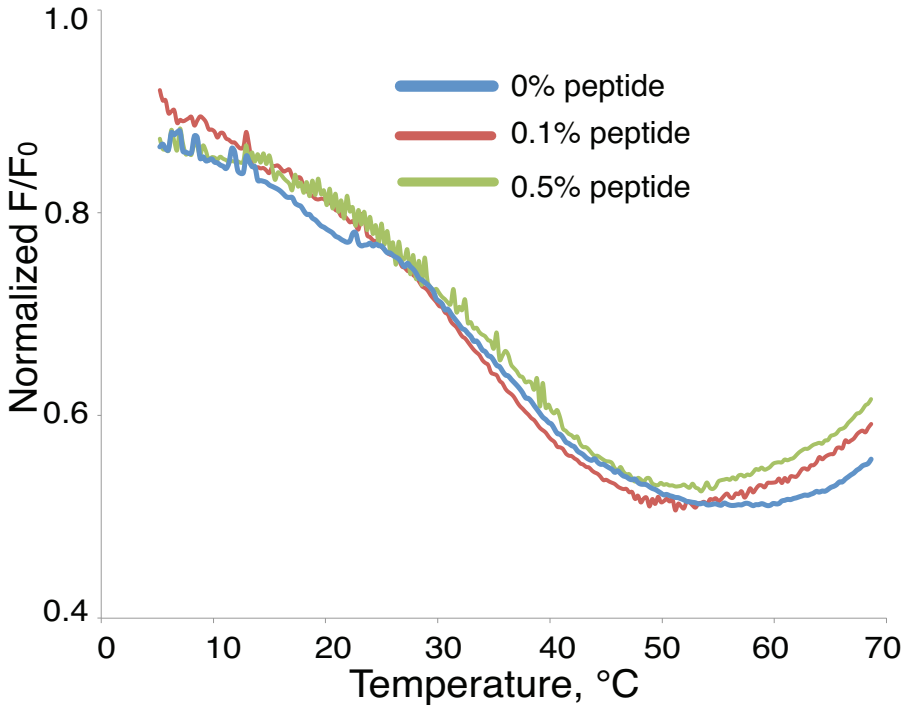

Figure 2-24 Test of a boundary localization of N-Ras C-terminal lipopeptide. Heating profiles for raft LUV with DPH and Rhod-DOPE and increasing concentration of non-fluorescent lipopeptide. The curves were shifted along Y-axis to facilitate comparison of the transition region

2.3.3 Domain Localization of the Lipid Probes Detected by Time-Domain Fluorescence Measurements

Determination of FRET in heating/cooling experiments was based on fluorescence intensity measurements, which requires exactly matching concentrations of donor in F and F_o samples. This is difficult to achieve for protein-lipid samples because protein incorporation in lipid bilayer is always partially completed. However, FRET may also be estimated from lifetime measurements that are insensitive to variations of donor concentration. Life time measurements were widely used for characterization of environment of the fluorophore labels (*122*) and lipid microdomains (*123*), (*97*). *H*-Ras localization was probed by FRET to lipid domain markers (*124, 125*). In that study the raft membranes were originating from living cells incorporating all other membrane-associated proteins and therefore, it was impossible to determine whether Ras distribution was governed by its own affinity to lipid rafts or was mediated by another protein. The motivation of our work was to create synthetic raft membranes closely mimicking lipid domain organization of cellular membranes but devoid of all other protein components.

Figure 2-25 demonstrates lifetime of DPH in homogeneous and raft-containing LUV. The homogeneous and raft mixtures lacking acceptor exhibited relatively invariable life times throughout full temperature range. In the presence of acceptor, the donor lifetime in a homogeneous sample is reduced but remains independent of the temperature. The raft samples containing the acceptor reveal significant drop in DPH lifetime in a narrow temperature range indicative of raft-melting phase transition. Figure 2-26 demonstrates a corresponding change in FRET efficiency calculated from data in reflecting greater accessibility of DPH to Rhod-DOPE after rafts are melted. This

observation is in agreement with data in Figure 2-18, and confirms that we can use lifetime measurements for determination of protein localization in lipid nanodomains.

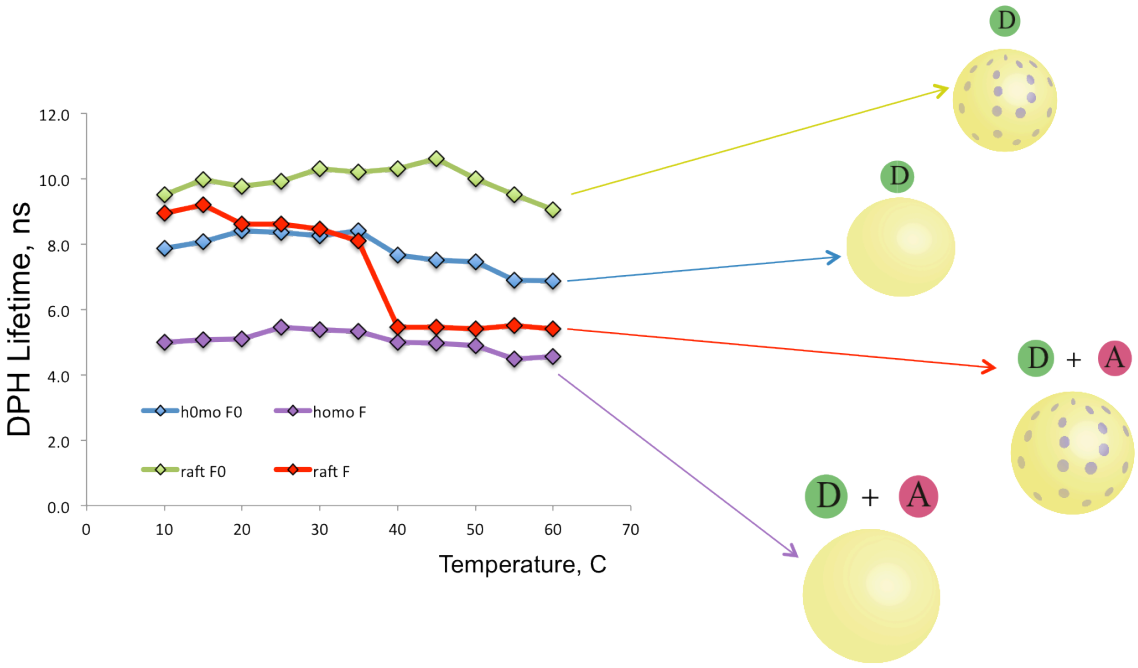

Figure 2-25 Raft stability in SM/POPC/cholesterol bilayers evaluated through time-domain fluorescence measurements. Lifetimes of DPH fluorescence at different temperatures in homogeneous and raft-containing mixtures in the presence and the absence of acceptor Rhod-DOPE

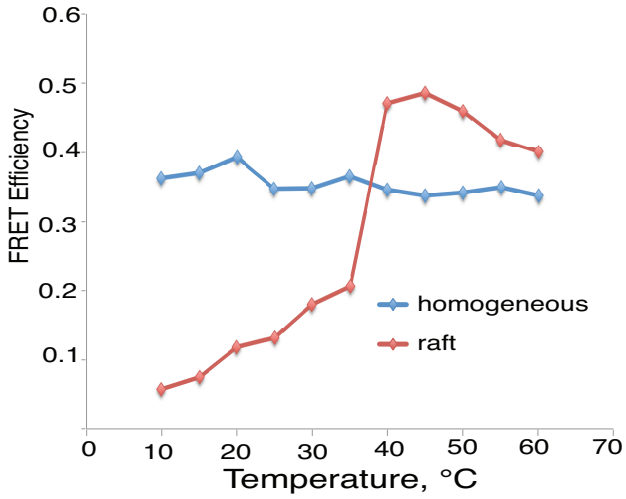

Figure 2-26 FRET efficiency calculated using Eq. 1 (see Materials and Methods) from lifetimes of DPH in Figure 2-25

2.3.4 Interaction of Ras Proteins with Lipid Membrane Mimic

In previously described experiments involving Ras and lipid membrane mimics the proteins were added to bilayers directly before the measurement, without separation of unbounded protein (*126*), (*127*). To analyze the pure sample of the membrane-tethered Ras we excluded several unwanted interactions, which could introduce bias results. First, we confirmed that the majority of the signal we measure comes from the membrane-associated Ras (i.e. we had to remove all lipidated protein unassociated with LUVs). Second, we estimated the percentage of the signal, which comes from the free mant nucleotides. To ensure that we are able to completely separate unbound mant-nucleotides and non-lipidated Ras from Ras-LUV conjugates we performed gel-filtration for the following samples:

- homogeneous and raft LUV sample labeled with 2% Rhod-DOPE to establish elution range of LUVs
- non-lipidated *N*-RasC118S-181 sample labeled with Mant-GDP to ensure their elution range is significantly distinct from LUVs
- a mixture of homogeneous LUV sample and non-lipidated *N*-RasC118S-181 incubated overnight to ensure that G-0domain by itself does not interact with the bilayer
- lipidated *N*-RasC118S-181 sample labeled with Mant-GDP to confirm interaction of lipidated protein with the bilayer

After elution the fluorescence intensity of mant or/ and rhodamine dye was measured in each tube and plotted on the graph. Figure 2-27 depicts the elution profile of homogeneous and raft LUV sample labeled with 2% Rhod-DOPE. As expected the LUV

were eluted in a void volume of a column (tubes 0-2) according to their large hydrodynamic radius.

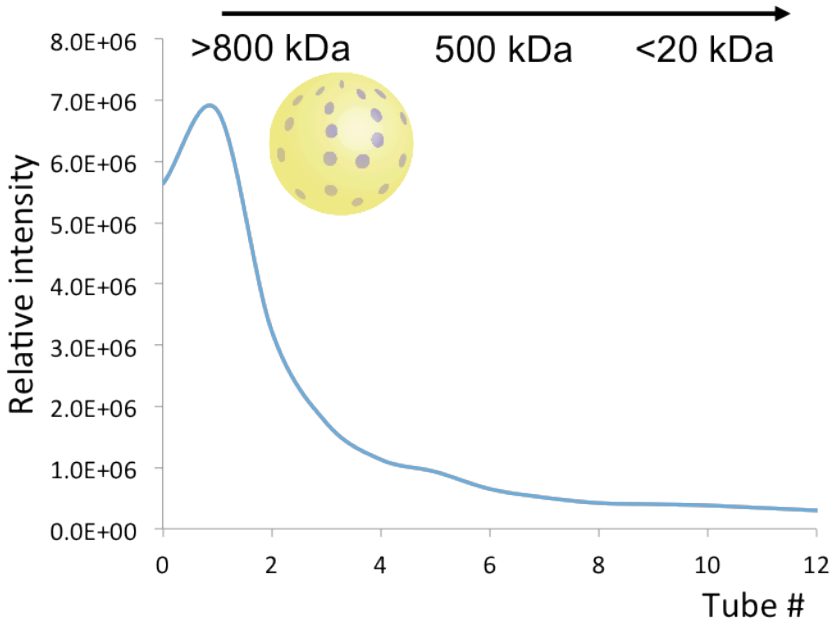

Figure 2-27 Elution profile of homogeneous/raft LUV sample labeled with 2% Rhod-DOPE

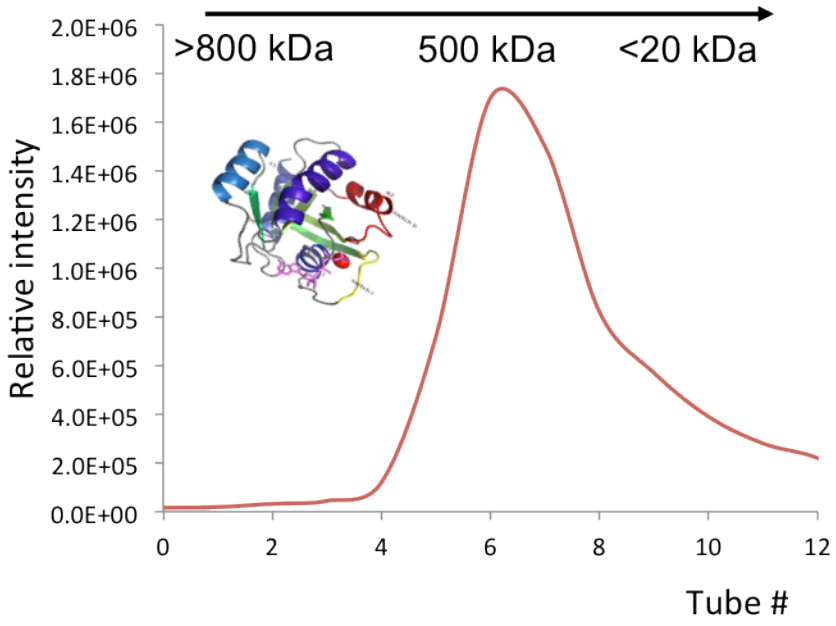

Figure 2-28 Elution profile of non-lipidated *N*-RasC118S-181 sample labeled with Mant-GDP

Similar elution conditions were used for the non-lipidated *N*-RasC118S-181 sample labeled with Mant-GDP (Figure 2-28). As seen on Figure 2-28 the non-lipidated protein was eluted according to it's molecular weight ~22 kDa, very distinct from LUV elution range.

Upon elution of the mixture of Rhodamine-labeled LUVs with non-lipidated Ras bound to mant-GDP the peaks of the corresponding dyes were approximately at the same molecular weight range as in Figure 2-27 and Figure 2-28, suggesting that the protein without lipid anchors cannot significantly interact with the lipid bilayer (Figure 2-29).

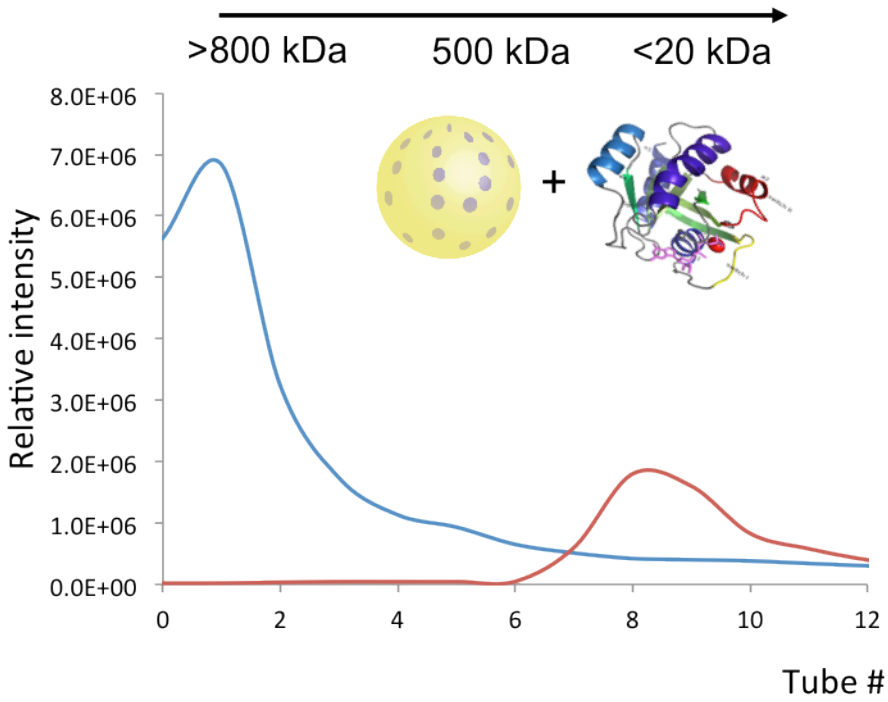

Figure 2-29 Elution profile of a mixture of homogeneous LUV sample and non-lipidated *N*-RasC118S-181 incubated overnight

The lipidated *N*-Ras protein eluted in a higher molecular weight region (approx.500 kDa compared to 22 kDa calculated molecular weight) (Figure 2-30). Larger hydrodynamic radius is likely caused by the presence of the hydrophobic lipid tails, which induce the formation of micelle-like aggregates comprising a few protein molecules.

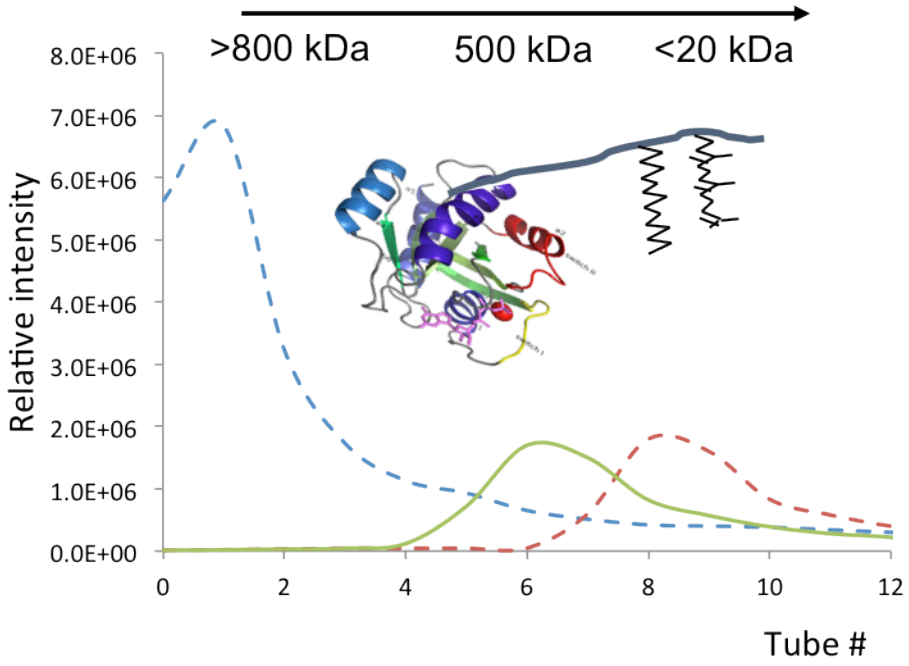

Figure 2-30 Elution profile of lipidated *N*-RasC118S-181 sample labeled with Mant-GDP

The lipidated protein samples incubated with LUVs eluted with the shift of the intensity maximum for Mant- suggesting insertion of the lipidated proteins into the LUV (Figure 2-31). However, the degree of Ras incorporation in homogeneous and raft-LUV was different, as revealed by a peak of free lipidated *N*-Ras unassociated with LUVs.

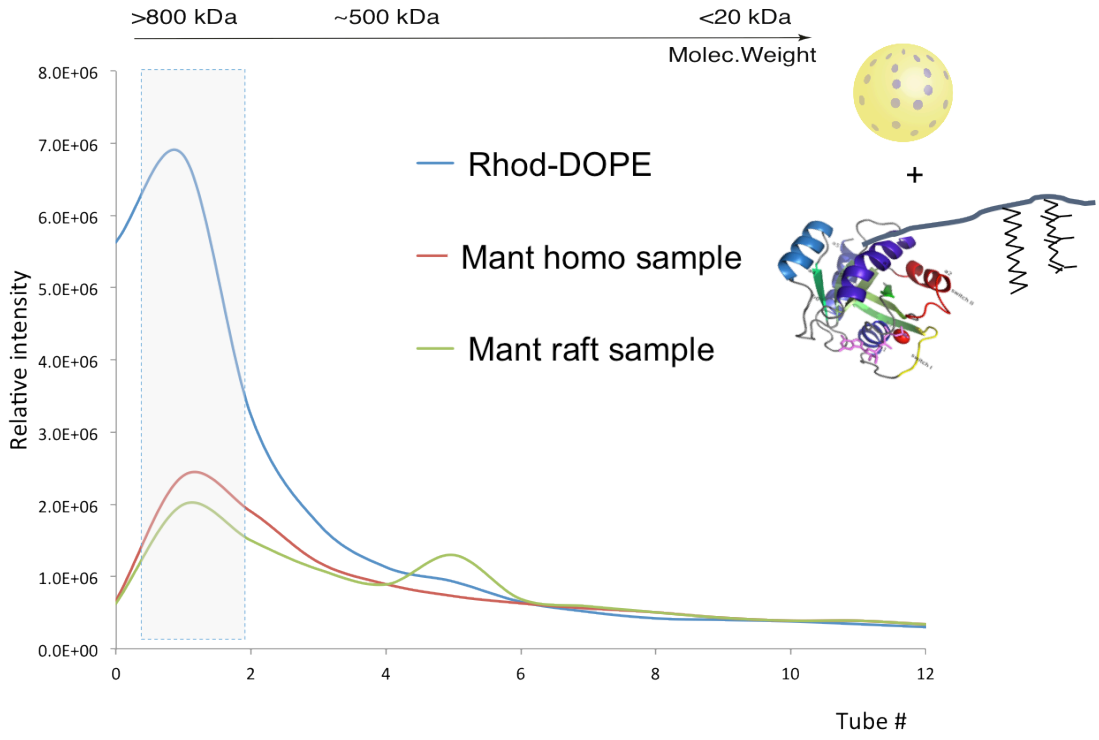

Figure 2-31 Elution profile of a mixture of homogeneous and raft LUV sample and lipidated *N*-RasC118S-181 incubated overnight

The number of lipidated Ras molecules in LUV samples was estimated using Bradford assay, and the corresponding surface density was calculated and represented in Table 2-1 (see Appendix B for the details). Elution volumes and approximate sizes of eluted complexes are summarized in Table 2-2.

Table 2-1. Surface density of protein on different types of LUVs

	Concentration measured, μ g/ml	N-Ras surface density, molec/ μ m2
homogeneous LUV sample	9 ±2	40,000

raft LUV sample	3±2	13,000

Table 2-2 Elution volumes and hydrodynamically equivalent size (a globular protein standard) for gel-filtration of Ras-LUV samples on Superose 6 Increase 10/300 GL column (GE Healthcare)

Sample	Elution volume	Corresponding size of a globular standard
N-RasC118S-181 (no lipid)	25 ml	<30 kDa
Homogeneous LUV	11 ml	>800 kDa
raft LUV	11 ml	>800 kDa
N-Ras-mGDP, lipidated, no LUV added	15-16 ml	~500 kDa
LUV with *N*-Ras-mGDP	11 ml	>800 kDa
LUV with *N*-Ras-mGppNHp	11 ml	>800 kDa

2.3.5 Preferential Localization of *N*-Ras

To determine the preferential localization of Ras we used FRET measurement between mant-nucleotides and lipid markers in raft bilayers. Lifetime measurements are preferable for protein samples to avoid unfolding of the protein upon heating. The lifetime constants were determined as described in Materials and methods (Ch.4.10.3). The lifetimes obtained by least-squared fits to the data are summarized in Appendix B. FRET efficiency was calculated using Eq. 1:

$$E = 1 - \frac{\tau_{DA}}{\tau_D}, \qquad \text{Eq.1}$$

where τ_{DA} and τ_D are the life times of donor in the presence and the absence of the acceptor (F and Fo samples), respectively. Standard deviation of FRET efficiency was estimated assuming independent errors of life times expressed by the Eq.2:

$$\delta E = \sqrt{\left(\frac{\delta\tau_{DA}}{-\tau_D}\right)^2 + \left(\frac{\tau_{DA}\delta\tau_D}{\tau_D{}^2}\right)^2} \qquad \text{Eq. 2}$$

An average FRET efficiency values for GDP- and GppNHp-loaded *N*-Ras proteins in homogeneous and raft LUVs at 5 °C are shown in Figure 2-32 (complete dataset if lifetimes can be found in Appendix B). High FRET efficiencies were observed for both homogeneous samples (mGDP and mGppNHp-loaded) indicating significant energy transfer from the donor (mant) fluorophore to the acceptor (rhodamine). This result was expected, since there is no phase separation in the bilyaer. In lipid raft samples the mGppNHp-loaded protein showed similarly high FRET efficiency reporting on easy accessibility of mant to rhodamine, which indicated that proteins is relatively excluded from rafts. In contrast, *N*-Ras-mGDP exhibited very low FRET values indicating effective segregation of mant-labeled Ras-GDP from Rhod-DOPE.

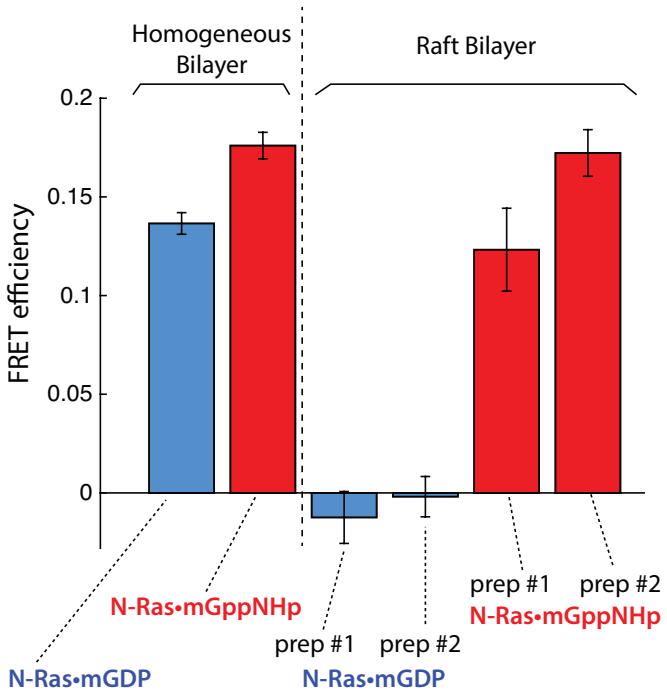

Figure 2-32 Efficiency of FRET between mant and Rhod-DOPE in samples of *N*-Ras-mGDP and *N*-Ras-mGppNHp at 5 ^{o}C. Error bars indicate standard deviations from replicate lifetime measurements (for the numbers of replicates see Appendix B). The raft LUV sample preparations were repeated to increase confidence in the result (indicated as prep #1 and #2, accordingly)

Similar measurements were performed for a "chimera" construct consisting of *H*-Ras *G*-domains coupled to *N*-Ras *C*-terminal lipidated peptide. As seen on Figure 2-33 all samples showed relatively high FRET efficiency independent on type of the nucleotide in both homogeneous and raft bilayers. In addition, the absolute value of FRET efficiency in homogeneous-mGppNHp, raft-mGppNHp and raft-mGDP samples was significantly higher comparing to homogeneous-mGDP suggesting that mant was more easily accessible for quenching by rhodamine.

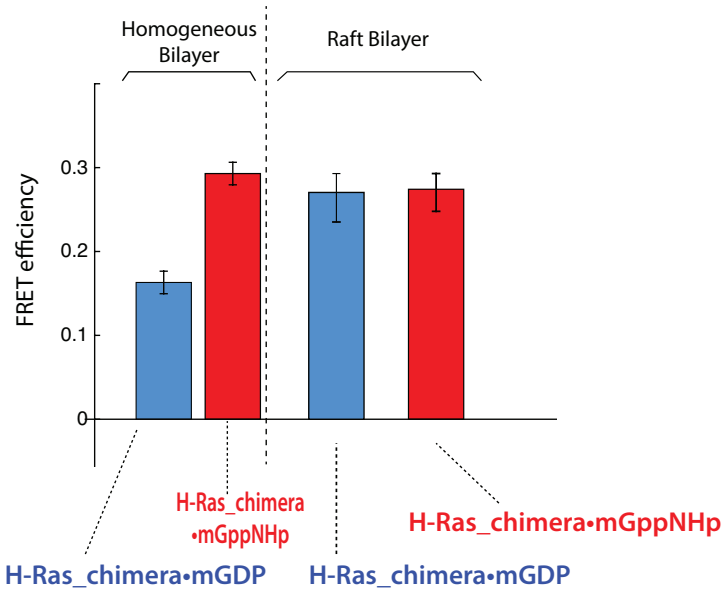

Figure 2-33 Efficiency of FRET between mant and Rhod-DOPE in samples of *H*-Ras-chimera-mGDP and *H*-Ras-chimera-mGppNHp

As an internal control, we attempted to convert raft samples into a "homogeneous" state by heating to 37 °C when much of the raft phase is gone. However, at this elevated temperature all homogeneous and raft LUV samples displayed near-zero FRET efficiencies suggesting that mant-nucleotides are completely separated from Rhod-DOPE. This separation might be due to dissociation of mant nucleotides from *N*-Ras upon heating considering long (1-4 hours) acquisition times of the TCSPC experiment and the weaker affinities of mant-nucleotides to Ras relatively to GDP and GTP.

2.3.6 Nucleotide Exchange of *N*-Ras Bounded to Lipid Mimic

FRET analysis of *N*-Ras association with lipid nanodomains presented in Figure 2-32 revealed that N-Ras in the GDP-bound form (signaling-inactive state) concentrates in rafts and exits into the disordered phase upon binding of a GTP-mimic. We attempted

to recapitulate this property in one sample and see how FRET will change upon the nucleotide exchange in protein associated with LUVs. We used mGDP-loaded samples associated with raft LUVs as a starting point. The FRET efficiency measurement replicated the results from the Figure 2-32 study with the nearly zero values for mGDP-Ras in raft-LUVs. Then the samples were subject to the nucleotide exchange followed by another purification. As expected, the fluorescence intensity of both donor and acceptor decreased significantly, however the lifetimes were still measurable. Contrasting to high FRET efficiency values in raft-GppNHp samples in Figure 2-32 the FRET efficiency in samples after nucleotide exchange was still low (nearly zero) (see Appendix B for actual values). These results suggested that the exchange procedure utilized in this experiment was not reliable. In the future work, the nucleotide exchange may be catalyzed by a specific GEF to achieve on-LUV activation.

3. Summary and Conclusions

About thirty years ago the existence of membrane microdomains was postulated using number of biophysical techniques (*128, 129*). The idea of membrane inhomogeneity led to reevaluation of a concept of membrane-associated proteins and their role in cell signaling (*18*). Two phases coexist in biological membrane: liquid disordered and liquid ordered. The latter is enriched in cholesterol and sphingolipids and known as lipid raft (*130*). Lipid rafts are present in both the inner and the outer leaflets of an asymmetric cell membrane (*131*), and form communication membrane platforms allowing tight interactions of signaling molecules together (*132*).

There are many membrane proteins incorporated into lipid raft phase. Examples include transmembrane proteins and GPI-anchored proteins (*133, 134*). Most of these proteins are permanently attached to the raft phase in the course of their functional cycle, but Ras protein is unique example that *switches* its domain localization according to protein functional state (*135*), (*83*). Thus, *K*-Ras was preferentially found outside lipid rafts, and *H*-Ras localization is regulated by GTP loading (*136*). In addition, in silico simulations provided evidence indicating that GTP-bound *H*-Ras is localized to the border between the lipid ordered/lipid disordered domains (*137*). However, the exact molecular mechanism of Ras partitioning between ordered and disordered domains has not been detailed in a well-defined model raft membrane.

The goal of our study was to evaluate lipid domain preferences of Ras in a synthetic lipid raft membrane. Use of in-vitro lipid bilayer mimic allowed identifying specific interactions that Ras makes with the lipid domains in the absence of other cellular proteins. One of the difficulties of mimicking natural lipid rafts that their size is

comparable to the wavelength of visible light making natural raft not resolvable in optical microscopes (*138, 139*). To create such nano-scale lipid domains, we utilized sphingomyelin/POPC/Cholesterol large unilamellar lipid vesicles and detected nanodomains with FRET. To calculate FRET we established two parallel measurements: intensity and lifetime-based approaches.

It was crucial to use faithful mimic of a post-translationally lipidated Ras in this analysis, therefore, we created semi-synthetic Ras protein constructs following a methods developed by H. Waldman group (*140*) (*110*) . The synthesis of full-length proteins was based on combination of bacterial expression and solid-phase synthesis technique. Flexible synthetic protocol allowed to make several types of constructs to test our main hypothesis about native partitioning of Ras, determined by concerted interactions of the G-domain and lipid anchors with the membrane domains.

We assessed the preferential localization of *C*-terminal lipopeptides for *N*-Ras and *H*-Ras isoforms and determined that the part of the hypervariable region was relatively excluded from rafts for both isoforms. We also tested the effect of lipopeptides on formation of the lipid rafts and found that lipid rafts stability was not affected by the presence of the *N*-Ras peptide. This funding indicated membrane-anchoring part of the protein is not involved in alteration of the bilayer.

Measurements of lifetime of mant-labeled Ras proteins associated with rhodamine containing LUVs allowed us to determine localization of semisynthetic lipidated Ras. We used both mant-GDP and mant GppNHp to mimic two functional states: the signaling-inactive, GDP-bound *N*-Ras was found to have preferential affinity for lipid rafts. *N*-Ras

in its activated conformation (bound to a GTP-mimic, mant-GppNHp) was localized outside of the rafts, at the raft boundary or in a disordered lipid phase.

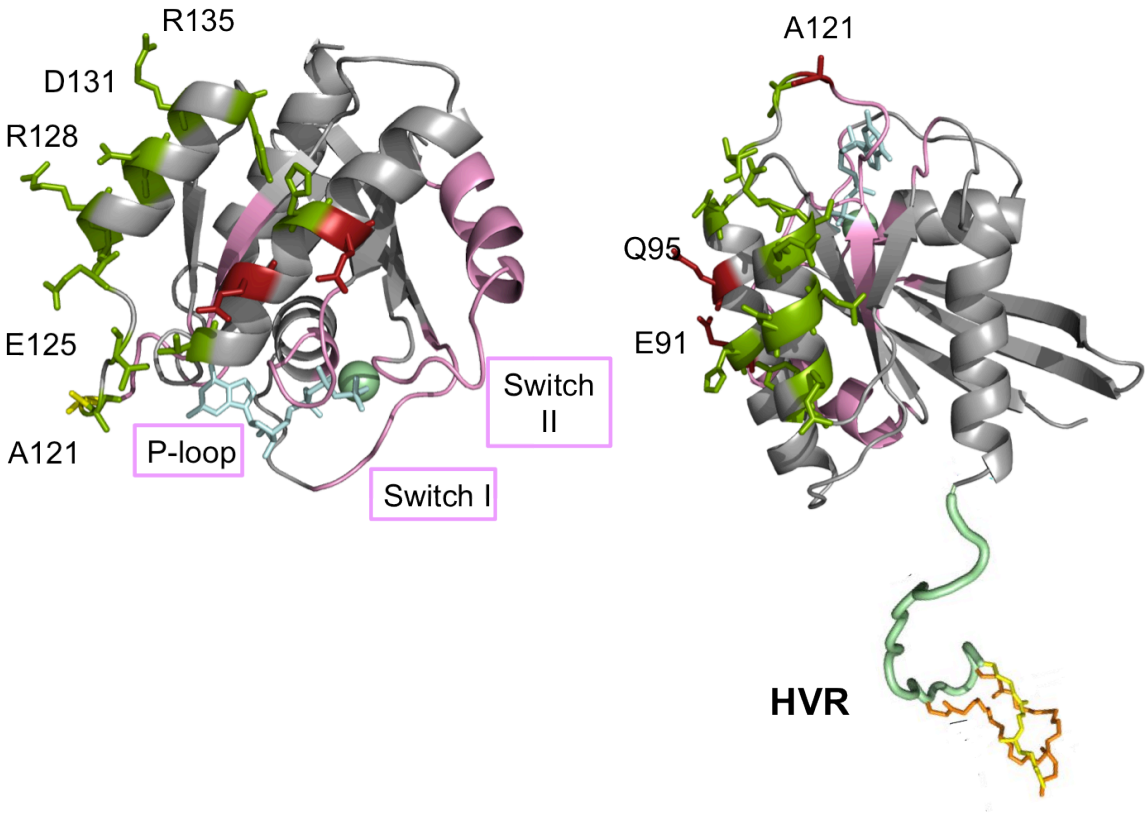

Figure 3-1 Left: *H*-Ras isoform catalytic domains structure (PDB ID 5p21). Right: lipidated *H*-Ras isoform structure. Residue differences in catalytic domains of *H*-Ras and *N*-Ras are shown as sticks. Pink – functionally important protein residues (conserved), green – conservative or semi-conservative mutations, red – non-conservative mutations

In summary, we demonstrated that *N*-Ras lipoprotein changes its lipid nanodomain preferences in a nucleotide-dependent manner in the absence of other membrane proteins. This indicates that Ras proteins themselves are responsible for the nucleotide-dependent localization in a living cell. The chimera construct where *H*-Ras G-domain was fused to *N*-Ras lipopeptide did not exhibit affinity to rafts. This finding indicates that Ras-lipid interaction mechanism depends on the particular sequence of the

G-domain (Figure 3-1) (*H*-and *N*-Ras G domains are homologous, but not identical, see sequence alignment in Appendix G). It is believed that upon the interaction between the catalytic domain and the plasma membrane orients positively charged helix 4 residues R128 and R135 close to the membrane (Figure 3-1), promoting specific electrostatic attraction to negatively charged lipids (*141*). Further studies involving mutants in the lipopeptide and the catalytic *G* domain parts are needed to identify the structural parts responsible for such behavior.

4. Materials and Methods

4.1 Chemicals

Table 4-1 List of the chemicals and suppliers

Name	Abbreviation	Supplier
N-[(9H-Fluoren-9-ylmethoxy)carbonyl]glycine	FmocGlyOH	Advanced Chem Tech
N-(9-Fluorenylmethoxycarbonyl)-L-proline	FmocProOH	Advanced Chem Tech
N-(9-fluorenylmethoxycarbonyl)-L-leucine	FmocLeuOH	Advanced Chem Tech
N-[(9H-Fluoren-9-ylmethoxy)carbonyl]-L-methionine	FmocMetOH	Advanced Chem Tech
Fmoc-N'-methyltrityl-L-lysine	FmocLys(Mtt)OH	Alfa Aesar
Fmoc-O-trityl-L-serine	FmocSer(Trt)OH	Alfa Aesar
N-Fmoc-S-trityl-L-cysteine	FmocCys(Trt)OH	Alfa Aesar
6-Maleimidohexanoic acid	MIC-COOH	Alfa Aesar
N-Methylanthranilic acid	Mant-COOH	TCI America
2-(1H-benzotriazol-1-yl)-1,1,3,3-tetramethyluronium hexafluorophosphate	HBTU	Advanced Chem Tech
Hydroxybenzotriazole	HOBt	Advanced Chem Tech

2,4,6-Trimethylpyridine	TMP	Sigma Aldrich
Trimethylacetic anhydride	Pivalic anhydride	Alfa Aesar
1-Hexadecene	Hexadecene	Alfa Aesar
2,2'-Azobis(2-methylpropionitrile)	AIBN	Alfa Aesar
Palmitoyl chloride	Pal-Cl	Alfa Aesar
Triethylamine	Et_3N	Alfa Aesar
N-(9-Fluorenylmethoxycarbonyloxy)succinimide	Fmoc-OSu	Alfa Aesar
trans,trans-Farnesyl bromide	FarBr	Sigma Aldrich
Ammonia solution, 7N in methanol	7N NH_3/MeOH	Alfa Aesar
N,N-Diisopropylethylamine	DIPEA	Alfa Aesar
1,1,3,3-tetramethylguanidine	TMG	Sigma Aldrich
Pyridine	Py	Sigma Aldrich
Copper(II) acetate	$Cu(OAc)_2$	Alfa Aesar
Trifluoroacetic acid	TFA	Alfa Aesar
Triethylsilane	TES	Alfa Aesar
Sodium borohydride	$NaBH_4$	Sigma Aldrich
1,2-dipalmitoyl-sn-glycero-3-phosphoethanolamine-N-[4-(p-maleimidomethyl)cyclohexane-carboxamide] (sodium salt)	MCC DPPE	Avanti Polar Lipids

2-Aminoethanethiol	cysteamine	Alfa Aesar
1,6-diphenyl-1,3,5-hexatriene	DPH	Sigma Aldrich
Cholesterol	Chol	Sigma Aldrich
Triton X-114	TX114	Sigma Aldrich
Chicken egg sphingomyelin	SM	Avanti Polar Lipids
1-palmitoyl-2-oleoyl-phosphatidylcholine	POPC	Avanti Polar Lipids
1,2-dioleoylphosphoethanolamine-N-(Lissamine Rhodamine B Sulfonyl	Rhod-DOPE	Avanti Polar Lipids
1,2-dioleoyl-sn-glycero-3-phospho-(1'-rac-glycerol) (sodium salt)	DOPG	Avanti Polar Lipids
1,2-dioleoyl-sn-glycero-3-phosphoethanolamine-N-(5-dimethylamino-1-naphthalenesulfonyl) (ammonium salt)	Dansyl-DOPE	Avanti Polar Lipids
2'-/3'-O-(N'-Methylanthraniloyl)guanosine-5'-O-diphosphate, sodium salt	Mant-GDP	Biolog Lifescience Institute (Bremen, Germany)
2'/3'-O-(N'-Methylanthraniloyl)guanosine-5'-O-[(β,γ)-imido]triphosphate	Mant-GppNHp	Biolog Lifescience Institute (Bremen, Germany)
Bacto Tryptone		Becton, Dickinson and Company
Yeast extract		Becton, Dickinson and Company
Sodium Chloride	NaCl	Sigma Aldrich
Tris(hydroxymethyl)aminomethane	TRIS	Sigma Aldrich

Ampicillin	Amp	TCI America
Agar	agar	Amresco
Isopropyl β-D-1-thiogalactopyranoside	IPTG	VWR Scientific
Ammonium persulfate	APS	Fisher Scientific
N,N,N',N'-tetramethylethane-1,2-diamine	TEMED	Fisher Scientific
30 % acrylamide solution	30 % AA	Hoefer
Bromophenol Blue	BPB	Fisher Scientific
Sodium Dodecyl Sulfate	SDS	VWR Scientific
β-mercaptoethanol		Sigma Aldrich
Dithiothreitol	DTT	VWR Scientific

All solvents were obtained from commercial suppliers (Thermo Fisher and VWR) and used without further purification.

4.2 Enzymes

All restriction enzymes and DNA modification enzymes were purchased from MBI Fermentas (ThermoFisher, USA) and New England Biolabs (Ipswich, MA).

4.3 Kits

E.Z.N.A Plasmid DNA Mini Kit I, OMEGA bio-tek

QuikChangeII Site-directed Mutagenesis Kit, Agilent Technologies

TOPO-TA Cloning Kit Invitrogen, Life Technologies

QIAGEN Plasmid Midi Kit, Qiagen

4.4 Software

Microsoft Office Excel

Microsoft Office Powerpoint

Microsoft Office Word

Matlab

FelixGX

DecayFit 1.4

MestreNova

ACDLabs

ChemDraw

Adobe Illustrator

EndNote

ApE (A plasmid editor)

4.5 Equipment

Table 4-2 List of instruments and equipment

Name	Model	Manufacturer
pH meter	Symphony SB90M5	VWR Scientific
Autoclave	L610	Washer Solutions
UV/vis Spectrophotometer	Cary 50 Bio	Varian
PCR machine	Mastercycler personal 5332	Eppendorf
Incubator shaker	I2500 series	New Brunswick Scientific
Centrifuge	5810R 15 amp version	Eppendorf
Centrifuge	Sorvall Lynx 4000	ThermoFisher
Dry heating block	D1100	Labnet International, Inc.
Mini Vortexer	VM-3000	VWR Scientific
Electrophoresis apparatus	Power Ease 500	Invitrogen, Life Technologies
Water bath	VWR	VWR Scientific
Sonifier	Branson 450	VWR Scientific
FPLC System • detector	SPD-M20A	Shimadzu, Japan

• degasser • communication module • liquid chromatograph	DGU-20A CBM-20A LC-20AT	
Rotary evaporator	R-200	Buchi
Solid phase synthesis reactor	50 mL	Chemglass

4.6 Resins and Chromatography Columns

Table 4-3 List of chromatography columns

Name	Manufacturer
Ultrogel Aca54/Superdex S200	GE Healthcare
Monobeads Q column XK 16/40 Q Hypercell resin	GE Healthcare/ Pall
Superose 6 Increase 10/300 GL	GE Healthcare
Jupiter 300 C4 column	Phenomenex

4.7 Bacterial Strains

BL21 CodonPlus ™ (DE3) competent cells

DH5 alpha competent cells

4.8 Plasmid Vectors

pCR 2.1-TOPO

The vector pCR 2.1-TOPO is a part of Topo TA cloning Kit. This vector bears Ampicillin- and Kanamycin –resistance genes, which allowed selection. The promoter used for an expression is a T7 polymerase. The vector map can be found in Appendix A.

pET43.1a(+)

The vector pET43.1a(+) was used as an expression vector for N-RasC118S-181C and H-RasC118S-181Cs. a part of Topo TA cloning Kit. This vector bears Ampicillin-resistance genes. The vector map can be found in Appendix A.

4.9 Oligonucleotides

Table 4-4 List of primers

Name of the primer	5'-Sequence-3'	Description
NRasC118S	GGTGCTAGTGGGAAACAAGTCTGAT TTGCCAACAAGG	forward primer to introduce C118S mutation
NRasC118S-r	CCTTGTTGGCAAATCAGACTTGTTT CCCACTAGCACC	reverse primer to introduce C118S mutation

NRasC118S181Ter	GATGGGACTCAGGGTTGTTAGGGA TTGCCATGTGTGGTG	forward primer for truncated 181N-Ras
NRasC118S181Ter-r	CACCACACATGGCAATCCCTAACAA CCCTGAGTCCCATC	reverse primer for truncated 181N-Ras
NRasC118S166Ter	GAGAAATACGCCAGTACTGAATGAA AAAACTCAACAGC	forward primer for truncated 166N-Ras
NRasC118S166Ter-r	GCTGTTGAGTTTTTTCATTCAGTACT GGCGTATTTCTC	reverse primer for truncated 166N-Ras

4.10 General Experimental Methods

All reactions involving moisture- or air-sensitive reagents were carried out under argon atmosphere in oven-dried glassware with anhydrous solvents. Purifications by chromatography were carried out using flash silica gel (32–63 mesh, VWR Scientific).

4.10.1 NMR Spectroscopy

NMR spectra were recorded on either a Varian Mercury+ 300 MHz or a Varian UnityInova 400 MHz instrument. ^{1}H NMR spectra were calibrated to δ=7.27 ppm for residual $CHCl_3$. ^{13}C NMR spectra were calibrated from the central peak at δ =77.23 ppm for $CDCl_3$. Unless otherwise indicated, NMR data were collected at 25 °C. The coupling

constants *J* are given in Hertz (Hz). Peak multiplicities are abbreviated as follows: s = singlet, d = doublet, dd = doublet of doublets, ddd = doublet of doublet of doublets, t = triplet, m = multiplet, br = broad signal.

4.10.2 Mass Spectrometry

The measurement of the MALDI-TOF mass spectra were recorded on a Voyager-DE ProBioSpectrometryTM workstation PerSeptive Biosystems with dihydroxybenzoic acid (DHB) as the matrix. The ESI mass spectra were measured with Shimadzu HPLC-MS 2020 system. Tandem liquid chromatography/mass spectrometry (LC-MS) was performed on a Shimadzu LCMS-2020 with autosampler, photodiode array detector, and single-quadrupole MS with ESI and APCI dual ionization, using a Peak Scientific nitrogen generator.

4.10.3 Fluorescence spectroscopy

Fluorescence measurements were performed in a QuantaMaster™ 400 Research Fluorometer (PTI). NBD was excited at 460 nm and the emission wavelength was scanned from 470 to 700 nm. DPH was excited at 358 nm and the emission wavelength was scanned from 370 to 700 nm. Mant was excited at 360 nm and the emission wavelength was scanned from 370 to 700 nm. The slit widths were 5 nm (excitation) and 5 nm (emission). The micro cells (3 mm width), StarnaCells, Inc. were used for measurements. The temperature ramp was applied as 1°C/min.

Measurements of steady-state and time-resolved fluorescence were performed using the Photon Technology International QM40 QuantaMaster system equipped with Pico-Master 1 time-correlated single-photon counting unit (HORIBA Scientific, Edison, NJ). A four-position Peltier-based Turret 400 (Quantum Northwest, Shoreline, WA) allowed for simultaneous temperature control and observation of up to four replicates for each sample condition. DPH, mant, and dansyl fluorophores were excited at 350, 360, and 340 nm, and their fluorescence was detected at 425, 440, and 520 nm, respectively. In heating and cooling experiments, temperature change rate was set 0.5^{o}C. Temperature differences between the cells were directly tested with a digital thermometer and did not exceed 0.5^{o}C. Time-domain fluorescence measurements of DPH and mant were done using the 365 nm LED with a pulse width of approx. 1 ns. The slit widths of the emission monochromator were adjusted in a range from 1 to 8 nm to maintain the TCSPC counting rate below 2%. The instrument response function, IRF, was recorded using a solution of a generic scatterer. Time-domain fluorescence decays were analyzed using DecayFit software (kindly shared by Søren Preus; available from www.fluortools.com). The three-exponential decay function was used to model the decay of the fluorophore fluorescence as well as a contribution of excitation light scattered by LUV in the samples.

The DecayFit software subtracted scattered light using variable contribution of the IRF while the rest of scattered photons were accounted for by the fast-decaying component of the three-exponential model (yielding a sub-nanosecond life time). The second component of the model with the life time on the order of 5-8 ns was used as representative of the fluorophore life time in the samples. The third life time, typically—

on the order of 20-40 ns, contributed very small percentage of signal (<5%) and, therefore, was ignored in the FRET analysis. The life time constants of the second component of the model obtained by least-squared fits to the data are summarized in Appendix B.

4.10.3.1 Temperature Ramps Data

All temperature ramps samples were prepared and measured in duplicates/quadruplicates. QM40/Temp mode was used for data collection. F_0 and F samples data was collected in one run to ensure identical temperature conditions. After data collection, blank traces were subtracted, F/F_0 ratio calculated in Felix GX software and corrected fluorescent intensity ratio traces were exported into .txt format. Along with fluorescence intensity ratio traces the temperature ramp traces were exported for each sample. Using the temperature ramp data the temperature of each sample was extrapolated and fluorescence intensity ratio data versus temperature was calculated and plotted.

4.10.3.2 Fluorescence Decays Data

All lifetime samples were prepared and measured in quadruplicates. First, F_0 samples lifetimes were measured, followed by F samples. TCSPC-Pol-temp mode was used for data collection. The following parameters were used for the measurement: channel count 1024, collection time 1800 sec, delay 160 sec, gain 1. Data for each sample was collected for 30 min with 3 repeats. After data collection, the group of traces

representing the same sample (3 repeats) was exported into .txt format (Felix GX). The data from the repeats was combined using pti_group_average.py script and converted to DecayFit compatible format using pti_trace_2_DecayFit.py script. The following parameters were used upon the conversion: start = 5, baseline_end = 20, trace_end = 75, zero_point = 5. Data was processed in DecayFit software using triple exponent fit model.

4.10.4 Absorbance UV-vis Measurements

All steady-state absorbance measurements were performed in 3 and 10 mm quartz cuvettes (Starna) using Varian Cary 50 Bio UV-Vis spectrophotometer.

4.10.5 Confocal Microscopy of Supported Lipid Bilayers

The LUVs with the lipid probes were prepared as described below. A small aliquot of the small-unilamellar vesicles suspension was diluted in PBS buffer, and then put in contact with freshly cleaned glass dish. The mixture was incubated at 37˚C for 30 min, and rinsed several times with buffer to remove the non-fused vesicles. The confocal fluorescence microscopy was performed on a Nikon A1R instrument (Nikon, Melville, USA). Confocal images were taken using the excitation light of an Alexa laser at 480 nm.

4.11 Molecular Biology Methods

4.11.1 Creation of Expression Vectors for N-Ras C118S-181

The following workflow was used to create an expression vector for N-RasC118S-181.

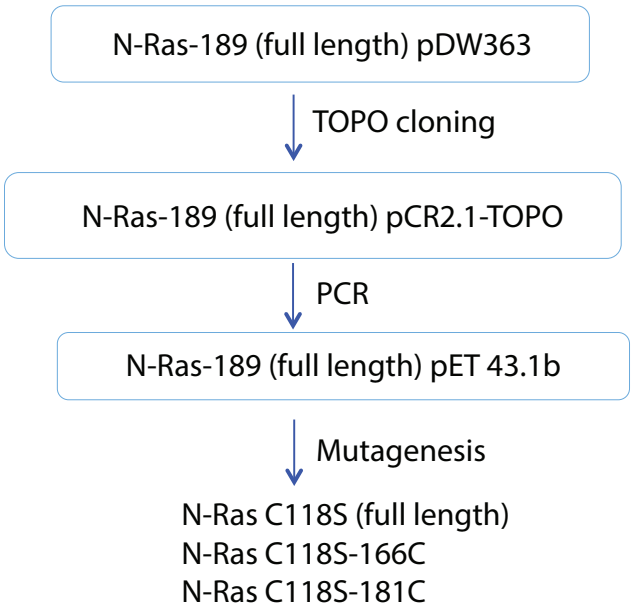

Figure 4-1 Block scheme for creation of expression vector for *N*-RasC118S-181C

4.11.1.1 TOPO Cloning

Cloning of amplification products was carried out with the help of TOPO TA Cloning Kits (Invitrogen, Life Technologies). In this case, the property of the topoisomerase I was used, which specifically recognizes the pentameric sequence 5´-(C/T)CCTT-3´ and forms a covalent bond with the phosphate group attached to the 3´ thymidine. The linearized N-Ras vector was provided with topoisomerase I covalently bound to each 3´ phosphate for complete reaction.

4.11.2 Site Directed Mutagenesis

N-Ras sequence was mutagenized by polymerase chain reaction using protocol by the QuikChange Site-Directed Mutagenesis Kit (Stratagene).

The mutagenesis reaction was prepared following the manufacturer's protocol containing:

2.5µ10X reaction buffer

25 ng of dsDNA template

1µl (20pM) of forward oligonucleotide primer

1µl (20pM) of reverse oligonucleotide primer

0.5µl of dNTP mix (0.2mM of dATP, dCTP, dGTP, dTTP)

0.5µl of Pfu ultra DNA Polymerase (25 U/µl)

ddH_2O to a final volume of 25 µl

The cycle parameters for the QuikChange Site-Direct Mutagenesis method are as indicated in Table 4-5.

Table 4-5 The PCR cycle parameters used for N-Ras mutagenesis

Segment	Cycles	Temperature	Time
1	1	95°C	30 sec
2	16	95°C	30 sec
3	1	55°C	1 minute
4	1	68°C	1 minute

The wild type parental pET43.1a(+) (AmpR) plasmid used for genetic manipulation was previously amplified and isolated from a Dam+ strain of E. coli, thus yielding a methylated pET43.1a(+) (AmpR) plasmid. The Quick-change PCR kit was used to create a non-methylated mutated derivative of the pET43.1a(+) plasmid which was used for subsequent cloning steps. The methylated template plasmid was digested by adding 1µl of DpnI restriction enzyme to the 50 µl Quick-change PCR reaction (outlined above) and incubating the sample at 37˚C for 1-2 hrs. Following the DpnI restriction digestion, the DpnI restriction enzyme was heat-killed by 10 minute incubation at 65˚C. The sample was then incubated on ice for 1 minute and the non-methylated mutated pET43.1a(+) (AmpR) plasmid was transformed into bacterial competent cells (DH5alpha) and plated on to LB +Amp plates for selection of positive transformants. DNA sequencing was also performed to verify the mutated residue and no additional mutations within the ORF of interest were present.

4.11.3 Cloning of *N*-Ras

Truncation of the full-length *N*-Ras cDNA and the introduction of the point mutation C118S were achieved using the high-fidelity *Pfu* DNA polymerase (Stratagene, La Jolla, CA). For the truncated version of *N*-Ras a stop codon was introduced to position 181 of the N-Ras C118S cDNA. The resulting fragment *N*-Ras C118S -181 was purified and digested with *Eco*RI and *Sma*I. It was subcloned into the pET43.1 expression vector and was transformed into the *Escherichia coli* strain CK600K (Stratagene).

4.11.4 Isolation of Plasmid DNA

The isolation of the plasmid DNA was achieved using E.Z.N.A. plasmid DNA Mini Kit I, Spin protocol. The final concentration of pET *N*-Ras C118S-181C plasmid was 0.2 ug/mL.

4.11.5 DNA Sequencing

DNA sequencing was performed at the Functional Biosystems Company, Madison.

The mRNA sequence alignment of human *N*-Ras wild type protein (Homo sapiens neuroblastoma RAS viral (v-ras) oncogene homolog, NCBI reference sequence: NM_002524.4) and *N*-RasC118S-181C construct is available in Appendix A. First mismatch corresponds to C118S mutation and the second one highlights the introduced stop codon 181.

4.12 Protein Chemistry Methods

This chapter describes the chemicals and biological reagents as well as molecular biology, cell biology and protein chemistry methods used in this study.

4.12.1 Expression Media Preparation

Luria Broth Medium, pH 7.4: 10 g of Bacto Tryptone, 5 g of yeast extract and 10 g of sodium chloride were mixed and dissolved in 800 mL of ddH_2O. After the pH was

adjusted to 7.4, and the volume of the solution was adjusted to 1L. The solution was autoclaved.

4.12.2 Antibiotics Stock Solutions Preparation

Ampicillin stock (100 mg/ml): 10g of ampicillin powder were dissolved in 10 mL of ddH_2O. The solution was filtered through 0.2 um sterile syringe filter and stored at -20°C.

4.12.3 IPTG Stock Preparation

2.38 g of IPTG were dissolved in 8 ml of ddH_2O. Final volume of the solution was adjusted to 10 mL. The solution was filtered through 0.2 um sterile syringe filter and stored at -20°C.

4.12.4 Agar Plates Preparation

1.5% agar in LB media

About 3 g of dry agar was added to autoclaved 200 mL LB media and heated to 50°C until homogeneous solution was obtained. Then the solution was poured into the sterile plates and kept at 4°C.

4.12.5 Transformation of Plasmid DNA into Competent Cells

The plasmid DNA (10-100 ng) was added to the competent cells and incubated on ice for 10 min. After incubation for the mixture was placed in water bath (42°C) for 30

sec and then incubated on ice for 5 min. Next the cells were allowed to recover and grow in 1mL of LB media without antibiotic for 1,5 hours at 37°C.

For protein expression the plates containing Ampicillin (1%) were used. The cell culture (100-200 uL) was evenly applied to the surface of the plate with Drigalski spatula and allowed to grow for 8-12 hours at 37°C.

4.12.6 SDS Page

The SDS-polyacrylamide gel is composed of stacking gel and separating gel. These gels have different acrylamide concentration and the pH value. Acrylamide forms polymers through a two-component redox system (APS and TEMED) by the addition of free radicals in a chain reaction. These are cross-linked into polyacrylamide in the presence of bisacrylamide. For the samples used in this work 15% bisacrylamide gels were prepared.

4.12.6.1 4X Separating Gel Buffer Preparation

Tris base (18.17 g) was mixed with 4 mL of 10% (w/v) SDS stock solution, and then pH was adjusted to 8.8. The final volume of the solution was adjusted to 100 mL. The buffer was stored at room temperature.

4.12.6.2 4X Stacking Gel Buffer Preparation

Tris base (3.03 g) was mixed with 2 mL of 10% (w/v) SDS stock solution, and then pH was adjusted to 6.8. The final volume of the solution was adjusted to 50 mL. The buffer was stored at room temperature.

4.12.6.3 10% APS Preparation

1 g of ammonium persulfate (APS) was dissolved in 10 mL of ddH_2O. The solution was stored at -20°C.

4.12.6.4 15% SDS-Polyacrylamide Gel Preparation

Table 4-6 Relative quantities of the reagents for preparation of stacking and separations gels

	Stacking gel	Separating gel
ddH_2O	1.20 mL	1.04 mL
30% acrylamide solution	532 uL	2.26 mL
4X separation gel buffer	-	1.14 mL
4X stacking gel buffer	360 uL	-
10% APS	33.6 uL	67.2 uL
TEMED	3 uL	3 uL

The gel was poured between two glass plates separated by the spacer. About two-thirds of the chamber was filled with the separating gel and 1 mL of isopropanol was added at the top of the gel to ensure flat edge after polymerization. After polymerization of the separation gel, the isopropanol was removed, the comb was gently inserted into the chamber and the stacking gel was poured over the separation gel. After polymerization, the casting plate was clamped into the gel chamber. The chamber was filled with SDS electrophoresis buffer, and the protein samples were loaded into the wells. The proteins were separated at 20 mA per gel and 200 V for about 1.5 h. After completion of the gel electrophoresis, the gel was removed from the glass plates and stained in the Coomassie dye for 1-3 hours.

4.12.6.5 4×SDS Sample Buffer Preparation

The following components were mixed: 1.0 g of SDS powder, 2.5 mL of 1M Tris solution with pH 6.8, 0.5 mL of ddH_2O, 4 mL of glycerol, 0.8 mL of 0.1% (w/v) Bromophenol Blue solution. The mixture was stored at -20°C in 1 mL vials. 0.2 mL of 14.3M β-mercaptoethanol was added to each vial before the use.

4.12.7 Protein Samples Preparation

The protein samples were treated with a suitable amount of 4 × SDS sample buffer, heated to 100°C for 3 min and after short centrifugation applied to the prepared polyacrylamide gel.

4.12.8 Bradford Assay

Protein concentrations were established using both Pierce Coomassie Protein Assay Kit (Thermo Scientific) and absorbance at 460 nm with the extinction coefficient of 21600 au M^{-1} cm^{-1}. Two BSA standard calibration curves were used for the concentration determination: 25-1500 ug/mL working range and 1-25 ug/mL working range (see Appendix A for details).

4.12.9 Protein Expression and Isolation

Expression and isolation *N*-Ras-C118S-181 and *H*-Ras-C118S-181 as performed as described earlier (*142, 143*) with little modifications. In brief, pET-RasC118S-181 DNA was expressed in BL21(DE3) cells under conditions favoring inclusion body formation (37 °C , 250 rpm) in Luria Broth medium. Protein overexpression was induced with 1.0 mM IPTG. The expressed protein was allowed to accumulate for 3 h at 37°C. The cultures were then centrifuged at 3500 g, and the pellet was frozen. Cell pellets were lysed by osmotic shock in 20 mM Tris, pH 8.0 and sonication. The inclusion body pellet was further solubilized in buffer containing 6 M urea, 20 mM Tris, pH 8.0, 5 mM $MgCl_2$, 1 mM DTT, and 0.03 mM GDP. The solubilized protein was spun for 10 min at 10,000 g, and the supernatant was separated from the pellet. The protein was refolded by slow injection into a refolding buffer (20 mM Tris, pH 8.0, 5 mM $MgCl_2$, 1 mM DTT, 0.3 mM GDP) to a final dilution ratio of 1:10. The refolded protein was extensively dialyzed against 20 mM Tris pH 8.0, 5 mM $MgCl_2$, 50mM NaCl, and concentrated using Amicon filter with 3000 MWCO membrane, loaded onto an anion exchange MonoBeads Q

column (GE Healthcare) equilibrated with the dialysis buffer and eluted with a linear NaCl concentration gradient. Eluted fractions were analyzed by SDS-PAGE, and pooled fractions were concentrated using Amicon centrifugal devices with MWCO of 3000 kDa. Concentrated protein solution was injected on Superdex S200 (GE Healthcare) column equilibrated with 20 mM Tris, pH 8.0, 200 mM NaCl, 5 mM $MgCl_2$, 1mM DTT. Purified protein was eluted as a symmetrical peak corresponding to a molecular weight of approximately 18 kDa. Final protein yield was 2 mg from 1 L of medium. The final protein purity was greater than 95% (judged by sodium dodecyl sulfate−polyacrylamide gel electrophoresis).

4.13 Synthetic Chemistry Methods

Preparation of 1a

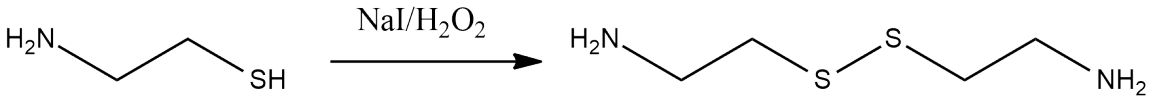

1a

Sodium iodide (8 mg, 0.052 mmol) and 30% hydrogen peroxide (1.2 mL, 5.2 mmol) were added to a stirred solution of cysteamine (0.40 g, 5.2 mmol) in water (0.5 mL) at r.t. The precipitated oil-like cystamine was collected by filtration. The remaining solvent was removed under vacuum. Rf 0.3 (dichloromethane/ methanol = 1:1). Yield: 0.6 g (mmol, 85 %). ^{1}H NMR (400 MHz, D_2O): 3.38 (t, J=8.5 Hz, 2H), 3.24 (t, J=7.0 Hz, 2H), 3.15 (t, J=8.7 Hz, 2H), 2.8 (t, J=8.7 Hz, 2H). MS (ESI): m/z calculated for 138.03 $[M + H]^+$, found 138.3 $[M + H]^+$.

Preparation of 1b

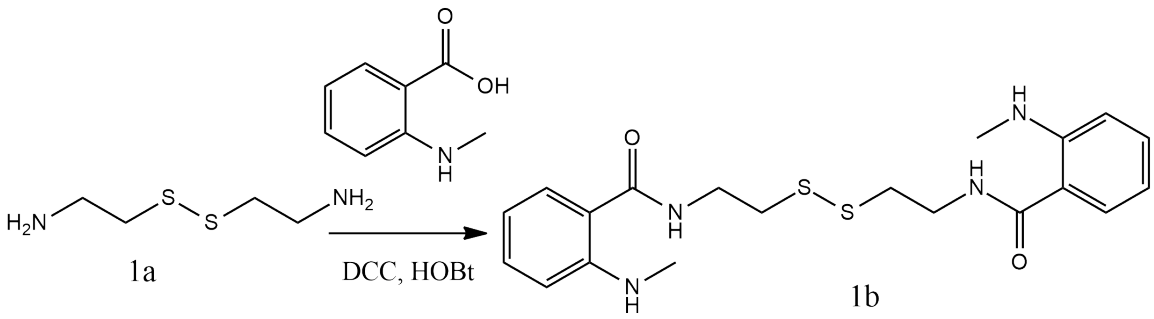

N,N'-dicyclohexylcarbodiimide (0.23 mg, 1.1 mmol) was added to a mixture of *N*-methylanthranilic acid (0.15 mg, 0.99 mmol) and 1-Hydroxybenzotriazole hydrate (HOBt) (0.134 mg, 0.99 mmol) in 15 mL of dry dichloromethane chilled in ice-water bath. The mixture was stirred for 1 h, and then the ice bath was removed. The formation of white precipitate was observed. Then cystamine (0.15 mg, 0.99 mmol) dissolved in 5 mL dichloromethane was added and the mixture was stirred 2 h at r.t. The mixture was placed in a freezer overnight, and the precipitate was removed by filtration. The desired compound was purified by silica gel chromatography in hexanes/ethyl acetate = 10:1. Rf 0.6 (hexanes/ethyl acetate = 9:1). Yield: 0.35 g (0.84 mmol, 85%). ^{1}H NMR (400 MHz, DMSO-d6): 8.5 (t, J=8.5 Hz, 2H), 7.5 (d, J=7.0 Hz, 2H), 7.25 (t, J=8.7 Hz, 2H), 6.6 (d, J=8.7 Hz, 2H), 6.5 (t, J=7.0 Hz, 2H), 3.5 (m, J=8.5, 7.5 Hz, 4H), 3.3 (s, 6H), 2.9 (t, J=7.5 Hz, 4H). MS (ESI): m/z calculated for 419.15 $[M + H]^{+}$, found 419.05 $[M + H]^{+}$.

Preparation of 1c

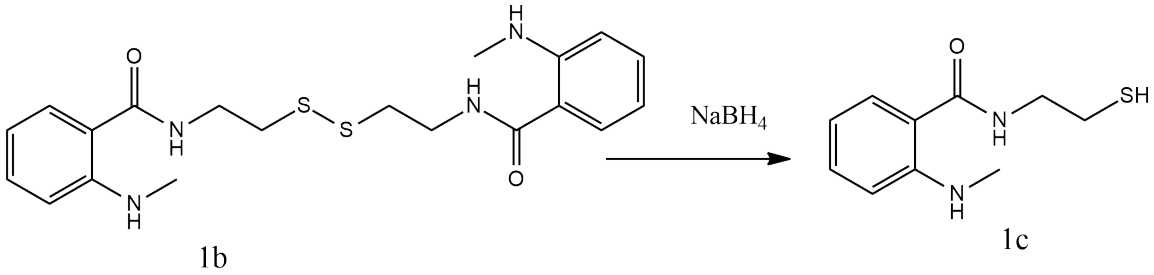

1b 1c

The Mant-disulfide (20 mg, 0.05 mmol) was dissolved in dry methanol under argon atmosphere. The solution was cooled to 0˚C, and sodium borohydride (2 mg, 0.05 mmol) was added slowly. The ice bath was removed and the mixture was stirred for 1h at r.t. The reaction was quenched by water, and methanol was removed by evaporation. The desired compound was extracted with ethyl acetate (3x20mL). The organic phases were collected and dried over anhydrous magnesium sulfate. Evaporation of the organic portion provided pure thiol in quantitative yield. Rf 0.45 (hexanes/ethyl acetate = 9:1). Yield: 0.010g (0.05 mmol, 99%). ^{1}H NMR (400 MHz, DMSO-d_6): 8.6 (t, J=8.5 Hz, 1H), 7.6 (d, J=7.0 Hz, 1H), 7.25 (t, J=8.7 Hz, 1H), 6.6 (d, J=8.7 Hz, 1H), 6.5 (t, J=7.0 Hz, 1H), 3.5 (q, J=8.5, 7.5, 2H), 3.3 (s, 3H), 2.8 (t, J=7.5 Hz, 2H). MS (ESI): m/z calculated for 210.1 $[M + H]^+$, found 210.05 $[M + H]^+$.

Preparation of 1d

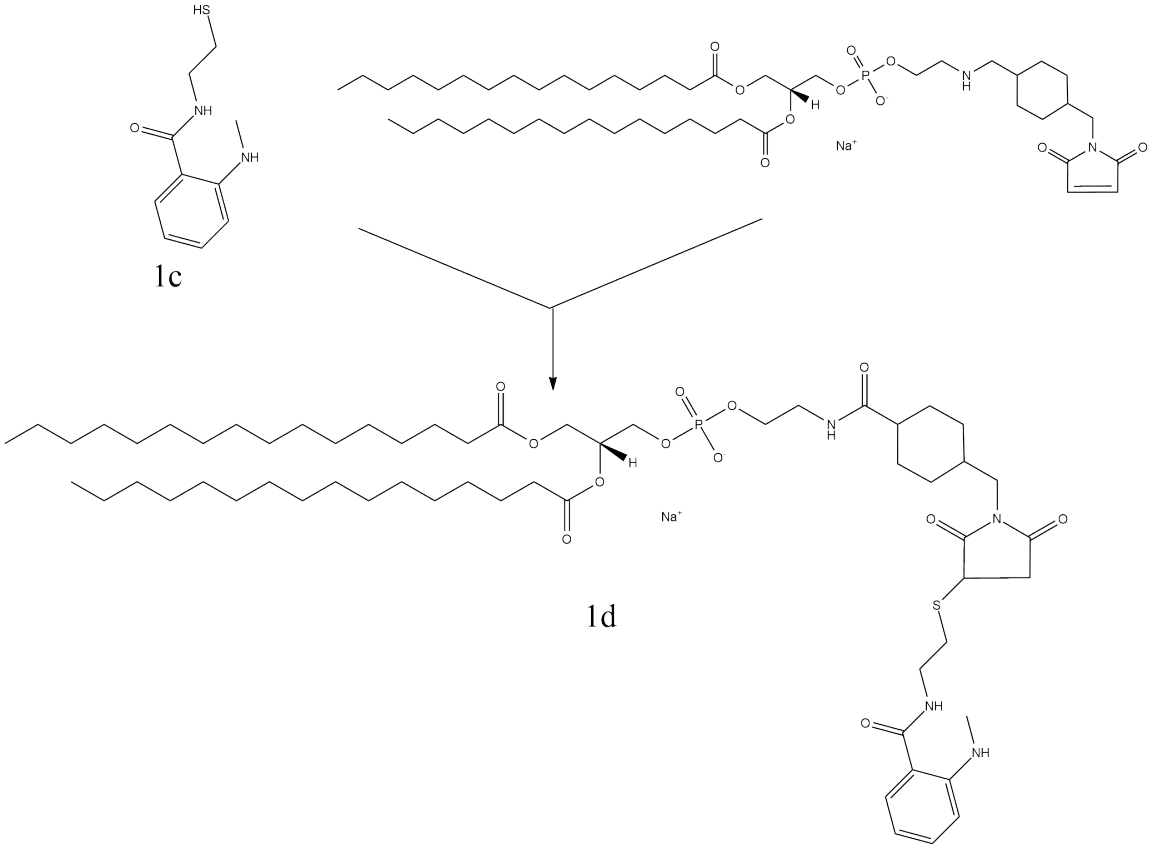

Freshly reduced sulfhydryl (50 mg, 0.24 mmol) was dissolved in dry dichloromethane under argon atmosphere and 1,2-dipalmitoyl-sn-glycero-3-phosphoethanolamine-N-[4-(p-maleimidomethyl)cyclohexane-carboxamide] (sodium salt) (MCC-DPPE) lipid (chloroform solution, 10mg/ml, 150uL=1.5 mg, 0.0016 mmol) was added. The mixture was stirred over weekend under argon. The desired compound was obtained after purification on glass TLC plate. Rf 0.8 (hexanes/ethyl acetate = 9:1). Yield: 1.5 mg (0.89 mmol, 88 %). MS (ESI): m/z calculated for 1121.7 $[M + H]^+$, found 1121.7 $[M + H]^+$.

4.13.1 Preparation of the Lipidated Amino Acids

Preparation of 2a

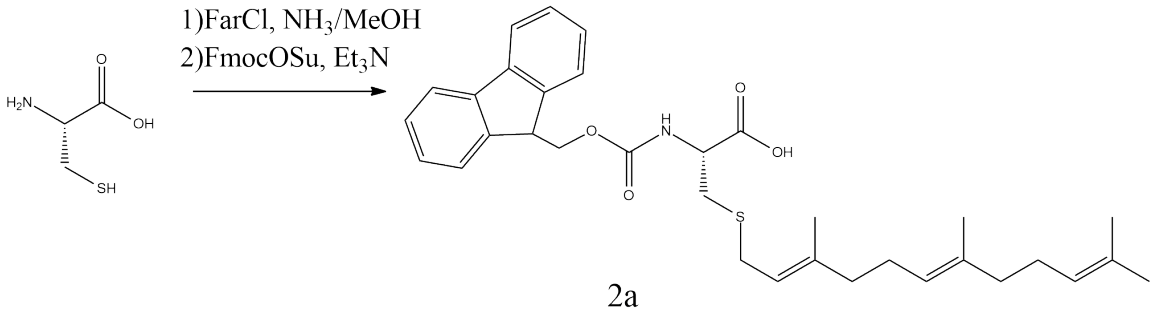

2a

7 N ammonia in methanol solution (8 mL) was added dropwise to a solution of *L*-cysteine hydrochloride monohydrate (0.4 g, 3.3 mmol) in methanol (3 mL) which was cooled to 0°C under argon atmosphere. After 5 min, trans, trans-farnesyl chloride (0.8 mL, 3.3 mmol) was added and the mixture was stirred for 3 h at 0°C and 1 h at room temperature. Subsequently, the solvent was removed under reduced pressure and the residue washed several times with n-pentane to remove residual farnesyl chloride. The residual solid was suspended in dichloromethane (10 mL) and again cooled to 0°C. Triethylamine (0.6 mL, 3.6 mmol) and N-(9-fluorenylmethoxycarbonyloxy)succinimide (1.2g, 3.6mmol) were added and the reaction mixture was stirred at room temperature overnight. After removal of the solvent under reduced pressure the desired compound was obtained as a colorless oil. The crude product was purified by flash column chromatography using gradient of methanol in dichloromethane 0-3%. Rf 0.3 (dicholoromethane/methanol =9:1). Yield: 0.95 g (1.73 mmol, 53% after two steps); ^{1}H NMR (400 MHz, $CDCl_3$): 7.76 (d, *J*=7.4 Hz,2H), 7.61 (d, *J*=7.5 Hz,2H), 7.40 (t, *J*=7.4 Hz,2H), 7.31 (t, *J*=7.4 Hz,2H), 5.60 (d, *J*=8.0 Hz,1H), 5.22 (t, *J*=7.4 Hz,1H), 5.12–5.06

(m,2H), 4.63 (m,1H), 4.47–4.39 (m,2H), 4.24 (t, *J*=7.0 Hz,1H), 3.27–3.15 (m,2H), 3.04–2.90 (m,2H), 2.14–1.93 (m,8H), 1.68 (s,3H), 1.65 (s,3H), 1.59 ppm (s,6H). ^{13}C NMR (100 MHz,$CDCl_3$): 75.7, 156.1, 143.8, 141.4, 140.5, 135.6, 131.5, 127.9, 127.3, 125.3, 124.5, 123.9, 120.2, 119.6, 67.7, 53.9, 47.5, 40.1, 40.0, 33.5, 30.5, 27.2, 26.9, 26.2, 18.2, 16.6, 16.5 ppm. MS (MALDI-TOF): m/z calculated for C33H47NO4S: 548.2835 $[M + H]^+$, found 548.04 $[M + H]^+$.

Preparation of 2b

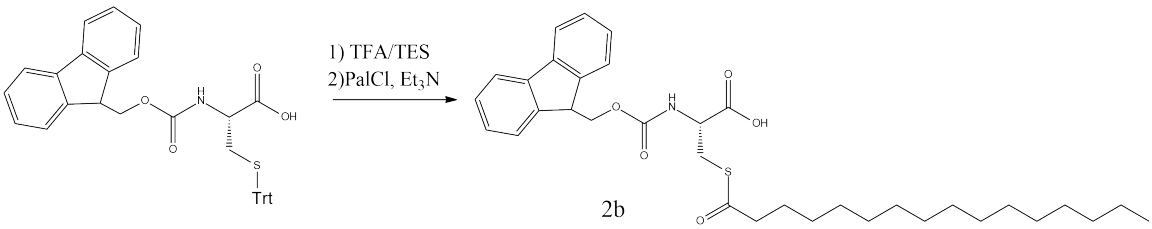

To a solution of N-(9-Fluorenylmethoxycarbonyl)-S-trityl-L-cysteine Fmoc-Cys(Trt) - OH (3 g, 12.5 mmol) in dichloromethane (75 mL) of trifluoroacetic acid (3.75 mL) and triethylsilane (2.25 mL) was added. The reaction solution was stirred for 1.5h at room temperature. The mixture was then co-evaporated with toluene and the residue was washed with n-pentane to remove the resulting triphenylmethane. The colorless solid was dissolved in dichloromethane (32.5 mL) obtained was chlorotrimethylsilane (0.72 mL, 5.63mmol) was added and the reaction mixture was heated under reflux for 2h. To the cooled solution of palmitoyl chloride (4.65 mL, 15.32 mmol) was added and a solution of triethylamine (1.17 mL, 8.39 mmol) in dichloromethane (22.5 mL) was added dropwise over 3 h under an argon atmosphere. The reaction solution was stirred for another hour at room temperature before the solvent was removed under reduced pressure. The crude

product was purified by flash column chromatography using gradient of methanol in dichloromethane 0-4%. The compound was isolated as colorless oil. Rf 0.4 (dicholoromethane/methanol =9:1). Yield: 1.32 g (2.26 mmol, 44% after two steps); ^{1}H NMR (400 MHz, $CDCl_3$): 7.76 (d, *J*=7.5 Hz, 2H), 7.62–7.55 (m, 2H), 7.40 (t, *J*=7.5 Hz, 2H), 7.29 (t, *J*=7.5 Hz, 2H), 5.64 (d, *J*=7.8 Hz, 1H), 4.62 (m, 1H), 4.39 (d, *J*=7.2 Hz, 2H), 4.24 (t, *J*=7.2 Hz, 1H), 3.50–3.34 (m, 2H), 2.59 (d, *J*=7.6 Hz, 2H), 1.70–1.60 (m, 2H), 1.23 (s, 24H), 0.89 ppm (t, *J*=6.9 Hz, 3H). ^{13}C NMR (100 MHz, $CDCl_3$): 199.5, 174.5, 156.2, 143.8, 141.4, 127.9, 127.3, 125.4, 120.2, 67.8, 62.8, 54.3, 47.4, 44.5, 32.4, 30.8, 30.12, 30.11, 30.10, 30.08, 30.03, 29.9, 29.8, 29.7, 29.4, 26.0, 23.1, 14.6 ppm. MS (MALDI-TOF): m/z calculated for C34H48NO5S: 582.3253 $[M + H]^+$, found 581.93 $[M + H]^+$.

Preparation of 2c

Method 1

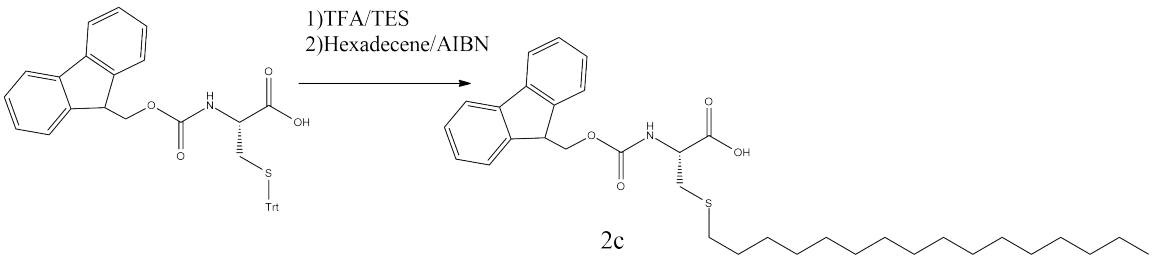

2c

Fmoc-cysteine(Trt)-OH (4 g, 6.8 mmol) was deprotected using similar conditions as in synthesis FmocCys(Pal)OH. The residue was dissolved in 30 mL of 1,2-dichloroethane (solvent was degassed under an argon stream in a sonicator bath for 15 min prior to use).

3 eq of 1-hexadecene and 0.5 eq of 2,2'-Azobis(2-methylpropionitrile) (AIBN) were added to this solution of the deprotected cysteine, and the mixture was brought to reflux at 90°C for 3 hours. The solution was cooled to room temperature, and the solvent was removed under reduced pressure. The resulting residue was purified by flash column chromatography using gradient of ethyl acetate in hexane 0-15% to provide the desired product. Rf 0.45 (dicholoromethane/methanol =9:1). Yield: 2.0 g (3.39 mmol, 52% after two steps). ^{1}H NMR (400 MHz, $CDCl_3$): 7.77 (d, *J*=7.4 Hz, 2H), 7.61(m, 2H), 7.41 (t, J=7.4 Hz, 2H), 7.32 (t, J=7.4 Hz, 2H), 4.65 (m, 1H, Fmoc), 4.42 (m, 2H), 4.25 (t, J=7.0 Hz, 1H), 3.05 (m, 2H), 2.56 (m, 2H), 1.57 (t, J=7.2 Hz, 2H), 1.26 (m, 28H), 0.89ppm (t, J=7.0Hz, 3H). ^{13}C NMR (100 MHz,$CDCl_3$): 174.9, 156.6, 143.7, 141.3, 127.7, 127.1, 125.1, 120.0, 67.4, 53.6, 47.1, 34.2, 32.9, 31.9, 29.7, 29.4, 29.2, 28.8, 22.7, 14.1 ppm; MS (MALDI-TOF): m/z calculated for C34H49NO4S: 590.3280 $[M+Na]^+$, found 590.3300 $[M+Na]^+$.

Preparation of 2c

Method 2

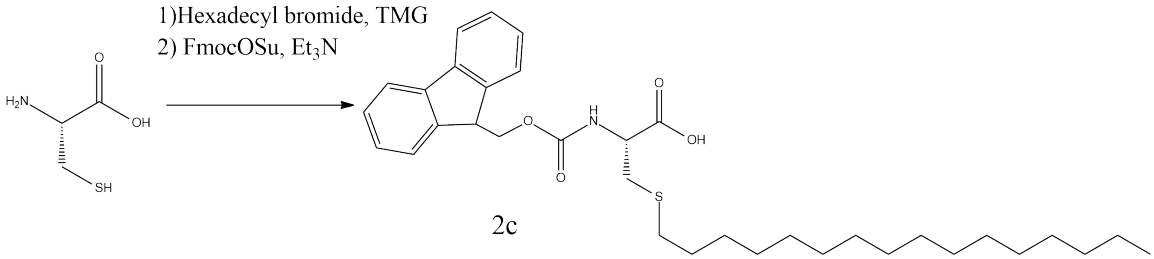

2c

A solution of 1,1,3,3-tetramethylguanidine (TMG) (0.65 ml, 5.2 mmol) in 3 ml of methanol was added dropwise to a stirred (under argon) mixture of *L*-cysteine

hydrochloride monohydrate (0.3 g, 2.5 mmol) in 2 ml of methanol. 0.83 mL (2.7 mmol) of hexadecyl bromide in dichloromethane was added dropwise to the homogeneous solution and the reaction mixture was stirred 1 h at 50 °C and then at room temperature overnight. Subsequently, the solvent was removed under reduced pressure and the residue washed several times with hexanes to remove residual hexadecyl bromide. Centrifugation was used to separate fine precipitate from the solvent. The residual solid was suspended in dichloromethane (6 mL) and cooled to 0°C. Triethylamine (0.25 mL, 1.8 mmol) and N-(9-fluorenylmethoxycarbonyloxy)succinimide (Fmoc-OSu) (0.60 g, 1.8 mmol) were added and the reaction mixture was stirred at room temperature overnight. After removal of the solvent under reduced pressure the desired compound was obtained. The crude product was purified by flash column chromatography using gradient of methanol in dichloromethane 0-5%. Rf 0.45 (dicholoromethane/methanol =9:1). Yield: 0.95g (1.6 mmol, 68 % after two steps). ^{1}H NMR (400 MHz, $CDCl_3$): 7.77 (d, *J*=7.4 Hz, 2H), 7.61(m, 2H), 7.41 (t, J=7.4 Hz, 2H), 7.32 (t, J=7.4 Hz, 2H), 4.65 (m, 1H, Fmoc), 4.42 (m, 2H), 4.25 (t, J=7.0 Hz, 1H), 3.05 (m, 2H), 2.56 (m, 2H), 1.57 (t, J=7.2 Hz, 2H), 1.26 (m, 28H), 0.89ppm (t, J=7.0Hz, 3H). ^{13}C NMR (100 MHz, $CDCl_3$): 174.9, 156.6, 143.7, 141.3, 127.7, 127.1, 125.1, 120.0, 67.4, 53.6, 47.1, 34.2, 32.9, 31.9, 29.7, 29.4, 29.2, 28.8, 22.7, 14.1 ppm. MS (MALDI-TOF): m/z calculated for C34H49NO4S: 590.3280 $[M+Na]^+$, found 590.3300 $[M+Na]^+$.

4.13.2 Solid-Phase Synthesis Procedures

4.13.2.1 Determination of Resin Loading by UV-vis Spectroscopy

A weighed amount of resin (2 to 5 mg) was washed with 10 mL of 20 % piperidine in dimethylformamide (v/v) and shaken for 10 min. The absorbance was measured against reference at λ = 301 nm. The loading was determined according to Beer's Law, A = εcd, where ε= 7800 at 301 nm. The concentration, and thus the degree of occupancy with Fmoc groups, was calculated using the Lambert-Beer's Law ($\mathcal{E}$ = 7800 $M^{-1}cm^{-1}$).

4.13.2.2 Kaiser Test

The Kaiser test was used to check to completeness of the coupling reactions. This test is a very sensitive test for primary amines. Ninhydrin reacts with the deprotected N-terminal amine group of the peptide-resin to produce an intense blue color, which allows qualitative determination of complete coupling reaction.

Kaiser Test Solutions:

Reagent A: 1. 16.5 mg of KCN was dissolved in 25 mL of distilled water and 1.0 mL of solution was diluted with 49 mL of pyridine

Reagent B: 1. 1.0 g of ninhydrin was dissolved in 20 mL of n-butanol

Reagent C: 1. 40 g of phenol was dissolved in 20 mL of n-butanol

10-15 beads of resin were placed in a test tube. 2 to 3 drops of Reagent A, 2 to 3 drops of Reagent B and 2 to 3 drops of Reagent C were added. The tubes was heated at 110°C for 5 minutes. Colorless or faint blue color indicated complete coupling. Dark blue colored solution indicated failed coupling and the coupling procedure was repeated.

4.13.2.3 Cleavage of Fluorenylmethyloxycarbonyl on the Solid Phase

For the removal of the fluorenylmethyloxycarbonyl (Fmoc) protecting group the following procedure was used in all cases.

Procedure E

A mixture of 20% piperidine in dimethylformamide (v/v) was degassed with argon for 15 min and added to the polymer. The resin was shaken for 10 min, and then the process is repeated. Subsequently, the resin was washed five times with dry, degassed dimethylformamide.

4.13.2.4 Solid-Phase Coupling Procedures

As a first step, the resin was swollen for 30 min with dicholoromethane / dimethylformamide (1:1) mixture. Subsequently, the Fmoc group was cleaved according to general procedure E.

Procedure AS1. Coupling of FmocCys(Far)OH

4 eq of FmocCys(Far)OH), 4 eq of 1-Hydroxybenzotriazole hydrate (HOBT) and 4 eq of N,N,N','-Tetramethyl-O-(1H-benzotriazol-1-yl)uronium hexafluorophosphate, O-(benzotriazol-1-yl)-N,N,N',N'-tetramethyluronium hexafluorophosphate (HBTU) were dissolved in degassed mixture of dicholoromethane/dimethylformamide (1: 1) upon stirring. Then 4 eq of collidine were added and the solution was incubated for 3min. After that, the entire solution was added to the resin. After 5h, the resin was washed three times with dicholoromethane, then three times with dimethylformamide. The loading of the resin was determined by loading test (described above).

Subsequently, the Fmoc group was removed according to general procedure E.

Procedure AS2. General coupling procedure

The following coupling procedure was used for coupling of all non-lipidated amino acids.

4eq of amino acid, 4eq of HBTU and 4eq of HOBt in were dissolved in dimethylformamide. Then 8eq of *N,N*-Diisopropylethylamine (DIPEA) were added and the mixture was incubated for 2min before it was added to the resin. After 2 hours, the resin was filtered off and then washed several times with dimethylformamide. The completeness of the coupling was checked with the Kaiser test (described above). In the case of incomplete coupling, the coupling procedure was repeated. Double coupling was performed after introduction of the lipidated amino acids.

Subsequently, the Fmoc protecting group was removed according to general procedure E.

Procedure AS3. Coupling of FmocCys(HD)OH

FmocCys(HD)OH (4 eq), 4 eq of HOBt and 4 eq of HBTU were dissolved in dicholoromethane/dimethylformamide (1:1) mixture, followed by addition of 4 eq of collidine and 3 minute incubation. After that, the entire solution was added to the resin. After overnight (8h) shaking under argon atmosphere, the resin was washed three times with dicholoromethane, then three times with dimethylformamide.

At the next step the Fmoc protecting group was removed according to general procedure E.

After that, the resin was washed with dimethylformamide (5 times), dicholoromethane (5 times) and dimethylformamide (5 times).

Procedure AS4. Coupling of 6-maleimidohexanoic acid MIC-COOH

For the N-terminal attachment of the maleimidocaproic acid the Fmoc protecting group was removed by general procedure E. Then, a solution of 5eq 6-Maleimidohexanoic acid (MIC-COOH), 5eq HBTU, 5 eq HOBt and 5eq DIPEA in dimethylformamide was allowed to couple for 3h. After completion of coupling, the resin was washed five times with dimethylformamide.

Procedure AS5. Coupling of N-methylanthranilic acid Mant-COOH

For the *N*-terminal attachment of the *N*-methylanthranilic acid the Fmoc protecting group was removed by general procedure E. Then, a solution of 5eq *N*-methylanthranilic acid (Mant-COOH), 5eq HBTU, 5 eq HOBt and 5eq DIPEA in dimethylformamide was allowed to couple for 3h. After completion of coupling, the resin was washed five times with dimethylformamide.

4.13.2.5 Capping

For the capping of unreacted amino groups the mixture of pivalic anhydride/ pyridine (1:1) was used. The mixture was added to the resin and shaken for 5 min. After that the resin was washed 5 times with dimethylformamide.

4.13.2.6 Elimination of the Lipopeptide

Before the cleavage of the peptide, the resin was washed three times with dry dicholoromethane.

A solution of copper (II) acetate $Cu(OAc)_2$ (0.55eq), pyridine (35eq), acetic acid (35eq), and methanol (215eq) in dicholoromethane was added. The cleavage reaction was

conducted in an open reactor, as the presence of oxygen was required. The resin was shaken for 2.5 h and washed by filtration several times with dicholoromethane. The crude product was co-evaporated several times with toluene and then purified.

4.13.2.7 Elimination of Mtt and Trt Protective Groups

The resin was washed three times with dry dicholoromethane. Then the resin was treated with a 1 % trifluoroacetic acid (TFA) and 2 % triethylsilane (TES) solution in dry dicholoromethane (v/v/v) and shaken for 1 h under argon atmosphere. The crude product was co-evaporated several times with toluene and then purified.

4.13.2.8 Purification of the Lipopeptides

The copper salts were removed from the crude reaction mixture by the following procedure. The dry crude mixture was dissolved in dicholoromethane and washed with a 0.1 M solution of HCl in water. The organic phase was dried under magnesium sulfate, filtered, and the solvent was eliminated under reduced pressure.

For the purification of the lipopeptides two routes were used. a) The lipidated peptides were purified on silica gel column using a 0–5 % gradient of methanol in DCM; or b) by preparative HPLC using a C4 column (Phenomenex). The detection was at 210 or 260 nm; flow rate 25 mL/min; total time 30 min; solvents: A—0.1 % TFA in water, B—0.1 % TFA in acetonitrile; gradient: 10 % B for 1 min, from 10 % B to 100 % B over 23 min, 100 % B for 2 min, 10 % B for 4 min. In both cases the identity of products was be confirmed by LC–MS.

Preparation of the lipopeptide MIC-Gly-Cys(HD)-Met-Gly-Leu-Pro-Cys(Far)-OMe

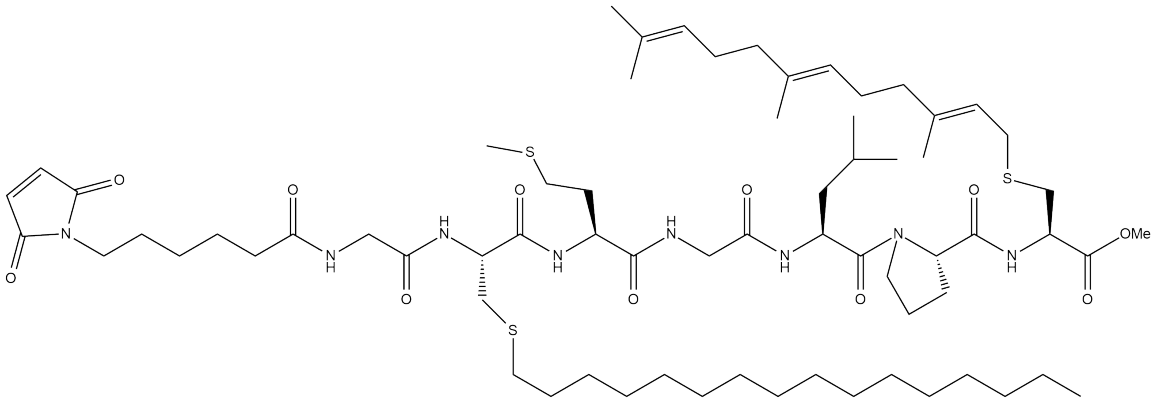

For this purpose, 300mg resin was used and swollen. The Fmoc was removed by procedure E and FmocCys(Far)OH was coupled by procedure AS1. Then the coupling of amino acids was performed according to the general procedures AS2-AS3. The 6-maleimidohexanoic acid was coupled using procedure AS4. Finally, the peptide was cleaved off by 17.8mg copper (II) acetate, 510 uL pyridine, 430 uL acetic acid and 1.54mL of methanol in 8 mL DCM. The peptide was purified by preparative HPLC or column chromatography. Rf 0.4 (dicholoromethane/methanol =9:1). Yield: 0.012g (20%). MS (ESI): m/z calculated for C68H114N8O11S3 1315.8 $[M + H]^+$, found 1315.75 $[M + H]^+$

Preparation of the lipopeptide Mant-Gly-Cys(HD)-Met-Gly-Leu-Pro-Cys(Far)-OMe

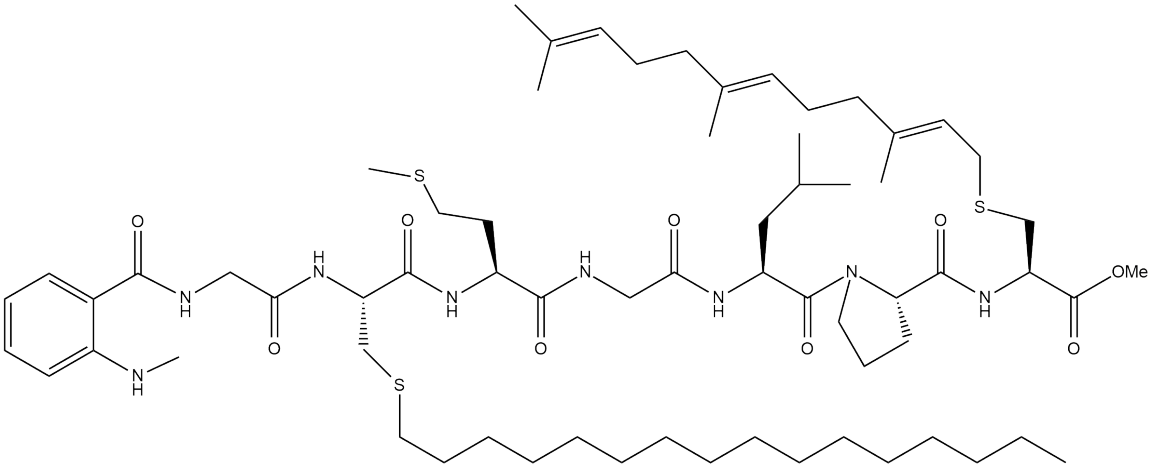

The synthetic procedure is similar to the one above, except that N-methylanthranilic acid was used instead of 6-maleimidohexanoic acid. The N-methylanthranilic acid was coupled using procedure AS5. Rf 0.4 (dicholoromethane/methanol =9:1). Yield: 0.017g (34%). MS (ESI): m/z calculated for C66H111N8O9S3$[M + H]^+$ 1255.8, found 1253.7 $[M + H]^+$.

Preparation of the lipopeptide $(CH_3)_3CC(O)NH$-Gly-Cys(HD)-Met-Gly-Leu-Pro-Cys(Far)-OMe

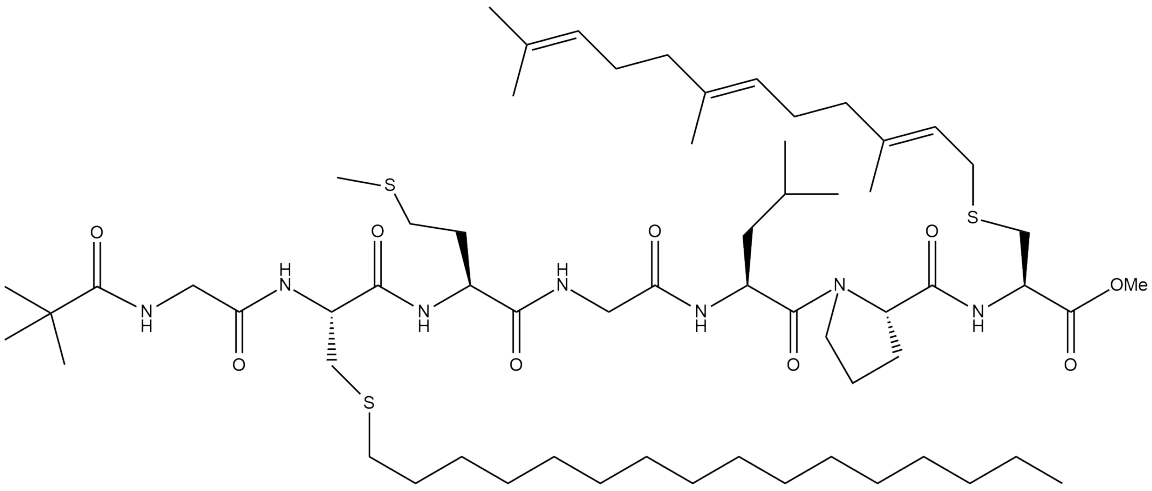

The synthetic procedure is similar to the one above, except that after introduction of FmocGlyOH and Fmoc deprotection, the reaction mixture was capped using the capping procedure (described above). The peptide was cleaved from the resin through elimination procedure. Rf 0.4 (dicholoromethane/methanol =9:1). Yield: 0.022 g (20 %). MS (ESI): m/z calculated for C63H111N7O9S3$[M + H]^+$ 1204.8, found 1204.5 $[M + H]^+$

Preparation of MIC-Gly-Cys(HD)-Met-Ser-Cys(HD)-Lys-Cys(Far)-OMe

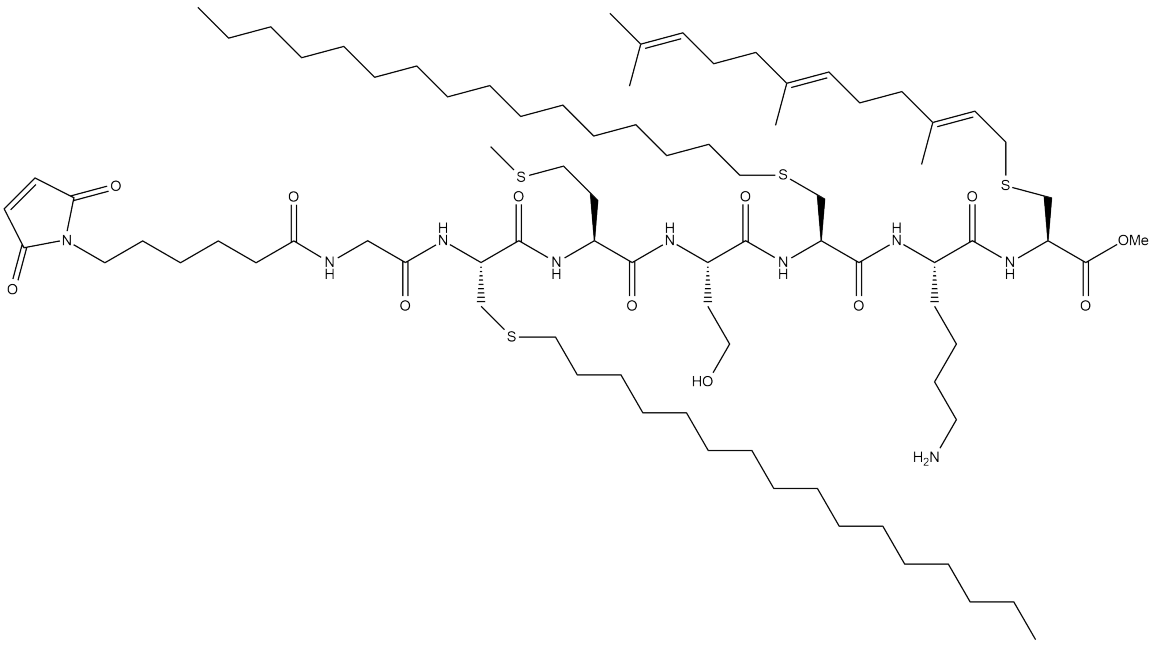

For this purpose, 300mg resin was used and swollen. The Fmoc was removed by procedure E and FmocCys(Far)OH was coupled by procedure AS1. Then the coupling of FmocLys(Mtt)OH was performed according to the general procedure AS2. The FmocCys(HD)OH was coupled using procedure AS3. Next couplings of lipidated and non-lipidtaed amino acids were performed according to AS2 and AS3 procedures, correspondingly. Finally, the peptide was cleaved off by 18.8mg copper (II) acetate, 600 uL pyridine, 480 uL acetic acid and 1.86mL of methanol in 10 mL DCM. The peptide

was purified by column chromatography. The Trt and Mtt protective groups were removed according to the described procedure. The deprotected peptide was purified by column chromatography. Rf 0.4 (dicholoromethane/methanol =9:1). Yield: 0.006 g (8%). MS (ESI): m/z calculated for C68H114N8O11S3 $[M + H]^+$ 1508.8, found $[M + H]^+$ 1508.8.

Preparation of Mant-Gly-Cys(HD)-Met-Ser-Cys(HD)-Lys-Cys(Far)-OMe

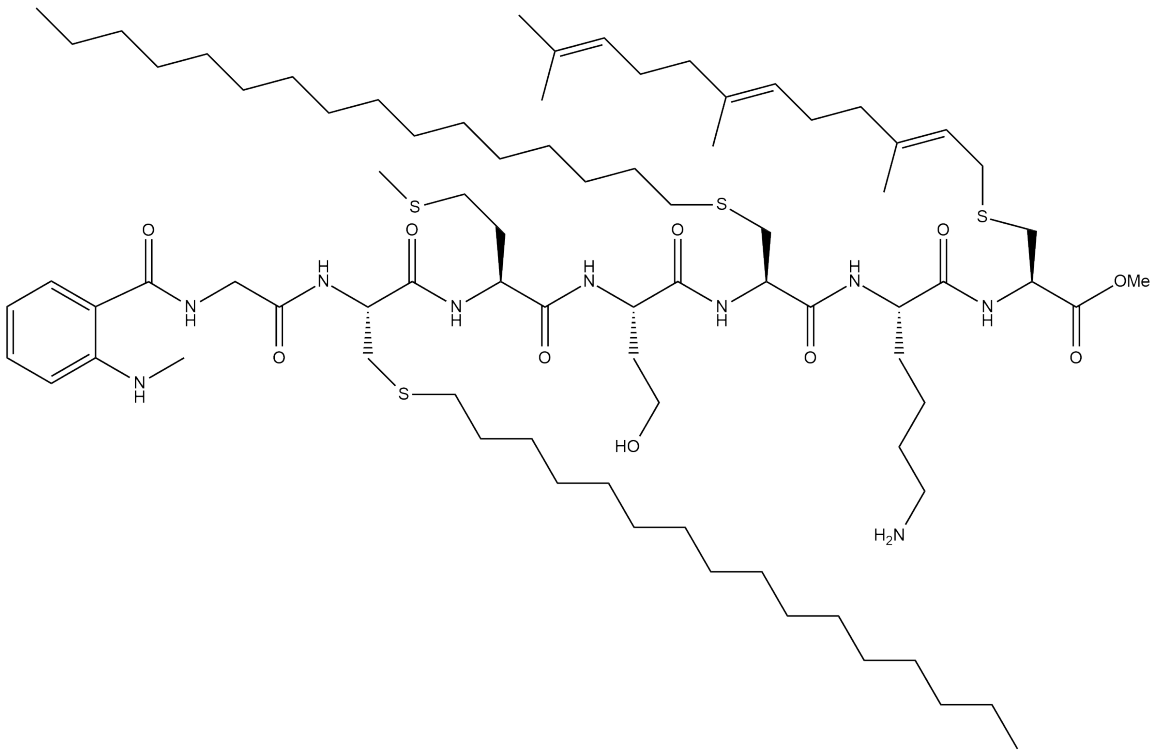

The synthetic procedure is similar to the one above, except that N-methylanthranilic acid was used instead of 6-maleimidohexanoic acid. The N-methylanthranilic acid was coupled using procedure AS5. Rf 0.4 (dicholoromethane/methanol =9:1). Yield: 0.007 g (10%). MS (ESI): m/z calculated for C68H114N8O11S3 $[M + H]^+$ 1643.6, found $[M + H]^+$ 1643.8.

4.14 Precondensation of TX-114

The precondensation procedure was performed to remove hydrophilic impurities from the commercial TX-114 (Sigma Aldrich). For this purpose 30 mM Tris pH 7.4, 100 mM NaCl buffer was used. 1.2 g of TX-114 was mixed in clear plastic tube with 40 mL of cold buffer. The mixture was incubated on ice for 10 min and mixed occasionally. Then the mixture was transferred into warm water bath (37-40°C) until it became cloudy and centrifuged for 7 min, 5,000 rpm at 37°C. The centrifuge was heated ahead of the time and the brakes were set to zero. After the centrifugation the upper phase was discarded, a new portion of ice-cold buffer was added and the separation procedure was repeated. Such washing procedure was repeated at least 3 times. The final purified TX-114 solution was stored at -20°C (1 mL aliquots).

4.15 Conjugation Reaction and Purification of Lipidated Protein

Before the conjugation reaction purified *N*-Ras-C118S-181 protein at concentration about 10 mg/ml was dialyzed against "coupling" buffer (20 mM Tris, pH 7.4, 5 mM $MgCl_2$) to remove DTT and excess NaCl, which may interfere with coupling. Lipidated peptide (1.5 eq) was solubilized in small amount of methanol and Triton X-114 was added. Peptide solution was sonicated and added to the protein. The reaction mixture was flushed with argon and incubated overnight at 4°C on rotator. Next day the mixture was spun for 12 min at 14,000 rpm and the supernatant was transferred to clean plastic tube. The reaction was quenched by addition of cold 20 mM Tris, pH 7.4, 5 mM $MgCl_2$, 1 mM DTT (2x dilution). The mixture was heated to 37°C until solution became cloudy

and centrifuged for 10 min at 3,500 rpm. Detergent and aqueous phases were separated and washed with a fresh DTT-containing "coupling" buffer or Triton X-114, respectively. All detergent phases were combined and diluted with cold DTT-containing "coupling" buffer (10x dilution). Then Amberlite XAD-2 (Supelco) beads prewashed with "coupling" buffer were added to the detergent mixture (to exceed concentration of Triton X-114 approximately 20 times) and incubated overnight at 4°C on rotator. The mixture was filtered and assessed by Bradford assay, UV-vis, SDS-PAGE and MALDI-TOF.

4.16 Preparation of Large Unilamellar Vesicles

Lipids and fluorescent analogs were dissolved in chloroform (with the exception of DPH, which was dissolved in ethanol) and stored at -20°C. The concentrations of fluorescent lipids were determined by absorbance using ε(Rhod-DOPE) 88,000 $M^{-1}cm^{-1}$ at 560 nm, ε(DPH) 84,800 $M^{-1}cm^{-1}$ at 352 nm, and ε(Mant-GDP) 22,600 $M^{-1}cm^{-1}$. Large unilamellar vesicles were prepared similar to as described previously (*98*). Lipids, fluorophores and peptides were mixed in glass vials. The chloroform was evaporated under a stream of nitrogen gas, and the dried lipid film was rehydrated in 20 mM Tris, pH 7.4, 5 mM $MgCl_2$, 150mM NaCl buffer at 70°C. To form 200 nm–sized unilamellar liposomes, the mixture was passed 21 times through a polycarbonate filter with a pore size of 200 nm (Avanti Polar Lipids). Total lipid concentration was 0.5 mM for melting experiments. Samples for Ras-LUV conjugation contained 1 mM total lipids. Background was acquired using samples lacking fluorescent probes.

4.17 Preparation of Ras-LUV Conjugates

At first step lipidated Ras samples were subject to the nucleotide exchange. For introduction of GDP-analog, the GDP nucleotide associated with the GTPase site in Ras was replaced with the (2'-(or-3')-*O*-(*N*-Methylanthraniloyl) guanosine 5'-diphosphate (mant- GDP) using the EDTA-assisted method (*144*). In brief, the magnesium ions in the protein samples were chelated with EDTA added to 6 mM along with the 0.8 mM mant-GDP and additional 10 mM DTT. The reaction mixtures were incubated for 2 h at room temperature, and mixed with LUV solution. Ras-LUV mixtures were incubated overnight at 4 °C and injected onto Superose 6 column equilibrated with 30 mM Tris, pH 7.4, 5 mM $MgCl_2$, 150 mM NaCl, 1 mM DTT buffer. Fractions corresponding to Ras-LUV conjugated were used for further experiments.

Nucleotide exchange for 2'-/3'-*O*-(*N'*-Methylanthraniloyl) guanosine-5'-O-[(β , γ - imidotriphosphate] (Mant-GppNHp) was performed as described in (*145*) with minor modifications. In short, protein solution was dialyzed against nucleotide-exchange buffer (50 mM TRIS, pH 8.0, 5 mM DTT, 200 mM $(NH_4)_2SO_4$). Nucleotide exchange was started by addition of Mant-GppNHp to a final molar ratio of 1:2 to protein. Shrimp alkaline phosphatase (Fermentas) was added (10 units) to hydrolyze released GDP molecules. Exchange was allowed to proceed for 2h at room temperature. Obtained Ras-GppNHp complex was dialyzed against 20 mM TRIS, pH 7.4, 1 mM DTT, 5 mM $MgCl_2$ buffer and mixed with LUVs.

BIBLIOGRAPHY

1. M. Malumbres, M. Barbacid, RAS oncogenes: the first 30 years. *Nat Rev Cancer* **3**, 459-465 (2003).

2. L. B. Eckert *et al.*, Involvement of Ras activation in human breast cancer cell signaling, invasion, and anoikis. *Cancer Res* **64**, 4585-4592 (2004).

3. A. Hall, C. J. Marshall, N. K. Spurr, R. A. Weiss, Identification of transforming gene in two human sarcoma cell lines as a new member of the ras gene family located on chromosome 1. *Nature* **303**, 396-400 (1983).

4. P. A. Konstantinopoulos, M. V. Karamouzis, A. G. Papavassiliou, Post-translational modifications and regulation of the RAS superfamily of GTPases as anticancer targets. *Nature Reviews Drug Discovery* **6**, 540-555 (2007).

5. J. L. Bos, H. Rehmann, A. Wittinghofer, GEFs and GAPs: Critical elements in the control of small G proteins. *Cell* **129**, 865-877 (2007).

6. I. R. Vetter, A. Wittinghofer, The Guanine Nucleotide-Binding Switch in Three Dimensions. *Science* **294**, 1299-1304 (2001).

7. J. Bos, ras oncogenes in human cancer: a review [published erratum appears in Cancer Res 1990 Feb 15;50(4):1352]. *Cancer Res* **49**, 4682-4689 (1989).

8. M. Trahey, F. McCormick, A Cytoplasmic protein stimulates normal N-Ras P21 GTPase, but does not affect oncogenic mutants. *Science* **238**, 542-545 (1987).

9. C. Walsh. (Roberts and Co. Publishers, Englewood, Colo. :, 2006).

10. J. F. Hancock, H. Paterson, C. J. Marshall, A polybasic domain or palmitoylation is required in addition to the CAAX motif to localize p21ras to the plasma membrane. *Cell* **63**, 133-139 (1990).

11. M. Völkert, The Chemical Biology of Ras Lipidation. *Biol. Chem.* **382**, 1133 –1145, (2001).

12. A. I. Lamond, Molecular biology of the cell, 4th edition. *Nature* **417**, 383-383 (2002).

13. E. London, Insights into lipid raft structure and formation from experiments in model membranes. *Current Opinion in Structural Biology* **12**, 480-486 (2002).

14. G. Cevc, Isothermal lipid phase transitions. *Chem Phys Lipids* **57**, 293-307 (1991).

15. G. van Meer, D. R. Voelker, G. W. Feigenson, Membrane lipids: where they are and how they behave. *Nat Rev Mol Cell Biol* **9**, 112-124 (2008).

16. N. Kahya, Light on fluorescent lipids in rafts: a lesson from model membranes. *Biochem J* **430**, e7-9 (2010).

17. S. J. Singer, G. L. Nicolson, The fluid mosaic model of the structure of cell membranes. *Science* **175**, 720-731 (1972).

18. K. Simons, E. Ikonen, Functional rafts in cell membranes. *Nature* **387**, 569-572 (1997).

19. I. A. Prior, C. Muncke, R. G. Parton, J. F. Hancock, Direct visualization of Ras proteins in spatially distinct cell surface microdomains. *J. Cell Biol.* **160**, 165-170 (2003).

20. F. Mollinedo, C. Gajate, Lipid rafts as major platforms for signaling regulation in cancer. *Advances in biological regulation* **57**, 130-146 (2015).

21. J. F. Hancock, Lipid rafts: contentious only from simplistic standpoints. *Nat Rev Mol Cell Biol* **7**, 456-462 (2006).

22. Techniques for studying lipid rafts. *Molecular Membrane Biology* **25**, 177-177 (2008).

23. D. Frey, T. Laux, L. Xu, C. Schneider, P. Caroni, Shared and Unique Roles of Cap23 and Gap43 in Actin Regulation, Neurite Outgrowth, and Anatomical Plasticity. *The Journal of cell biology* **149**, 1443-1454 (2000).

24. S. Maekawa *et al.*, Cholesterol-dependent localization of NAP-22 on a neuronal membrane microdomain (Raft). *Journal of Biological Chemistry* **274**, 21369-21374 (1999).

25. D. E. Saslowsky *et al.*, Placental alkaline phosphatase is efficiently targeted to rafts in supported lipid bilayers. *J Biol Chem* **277**, 26966-26970 (2002).

26. R. M. Henderson, J. M. Edwardson, N. A. Geisse, D. E. Saslowsky, Lipid rafts: feeling is believing. *News in physiological sciences : an international journal of physiology produced jointly by the International Union of Physiological Sciences and the American Physiological Society* **19**, 39-43 (2004).

27. R. M. Epand, B. G. Sayer, R. F. Epand, Peptide-induced formation of cholesterol-rich domains. *Biochemistry* **42**, 14677-14689 (2003).

28. R. P. Richter, R. Berat, A. R. Brisson, Formation of solid-supported lipid bilayers: an integrated view. *Langmuir* **22**, 3497-3505 (2006).

29. Q. Saleem, Z. Zhang, A. Petretic, C. C. Gradinaru, P. M. Macdonald, Single lipid bilayer deposition on polymer surfaces using bicelles. *Biomacromolecules* **16**, 1032-1039 (2015).

30. M. A. Schuler, I. G. Denisov, S. G. Sligar, Nanodiscs as a new tool to examine lipid-protein interactions. *Methods Mol Biol* **974**, 415-433 (2013).

31. D. Chandler, Interfaces and the driving force of hydrophobic assembly. *Nature* **437**, 640-647 (2005).

32. D. E. Vance, Vance, J.E. , *Biochemistry of Lipids, Lipoproteins and Membranes, 5th edition*. D. E. Vance, Vance,J.E, Ed., (Elsevier, Amesterdam, 2008).

33. V. A. Frolov, A. V. Shnyrova, J. Zimmerberg, Lipid Polymorphisms and Membrane Shape. *Cold Spring Harbor Perspectives in Biology* **3**, a004747 (2011).

34. B. L. Mui, P. R. Cullis, E. A. Evans, T. D. Madden, Osmotic properties of large unilamellar vesicles prepared by extrusion. *Biophys J* **64**, 443-453 (1993).

35. I. Langmuir, K. B. Blodgett, Regarding some new methods for the investigation of monomolecular layers. *Kolloid Z* **73**, 257-263 (1935).

36. I. Langmuir, The role of attractive and repulsive forces in the formation of tactoids, thixotropic gels, protein crystals and coacervates. *Journal of Chemical Physics* **6**, 873-896 (1938).

37. E. Kalb, L. K. Tamm, Incorporation of Cytochrome B5 into Supported Phospholipid-Bilayers by Vesicle Fusion to Supported Monolayers. *Thin Solid Films* **210**, 763-765 (1992).

38. S. J. Johnson *et al.*, Coupling of Spectrin and Polylysine to Phospholipid Monolayers Studied by Specular Reflection of Neutrons. *Biophysical Journal* **60**, 1017-1025 (1991).

39. B. W. Koenig *et al.*, Membrane structure at the solid/water interface studied with neutron reflectivity and atomic force microscopy. *Biophysical Journal* **70**, Wp229-Wp229 (1996).

40. O. Purrucker, H. Hillebrandt, K. Adlkofer, M. Tanaka, Deposition of highly resistive lipid bilayer on silicon-silicon dioxide electrode and incorporation of gramicidin studied by ac impedance spectroscopy. *Electrochimica Acta* **47**, 791-798 (2001).

41. J. Gureasko *et al.*, Membrane-dependent signal integration by the Ras activator Son of sevenless. *Nat Struct Mol Biol* **15**, 452-461 (2008).

42. T. K. Ritchie *et al.*, Chapter 11 - Reconstitution of membrane proteins in phospholipid bilayer nanodiscs. *Methods Enzymol* **464**, 211-231 (2009).

43. T. H. Bayburt, Y. V. Grinkova, S. G. Sligar, Self-assembly of discoidal phospholipid bilayer nanoparticles with membrane scaffold proteins. *Nano Lett* **2**, 853-856 (2002).

44. A. Nath, W. M. Atkins, S. G. Sligar, Applications of Phospholipid Bilayer Nanodiscs in the Study of Membranes and Membrane Proteins. *Biochemistry* **46**, 2059-2069 (2007).

45. T. H. Bayburt, S. G. Sligar, Membrane protein assembly into Nanodiscs. *FEBS Lett* **584**, 1721-1727 (2010).

46. M. L. Nasr, S. K. Singh, Radioligand binding to nanodisc-reconstituted membrane transporters assessed by the scintillation proximity assay. *Biochemistry* **53**, 4-6 (2014).

47. N. Skar-Gislinge *et al.*, Elliptical Structure of Phospholipid Bilayer Nanodiscs Encapsulated by Scaffold Proteins: Casting the Roles of the Lipids and the Protein. *Journal of the American Chemical Society* **132**, 13713-13722 (2010).

48. S. A. R. Kynde *et al.*, Small-angle scattering gives direct structural information about a membrane protein inside a lipid environment. *Acta Crystallographica Section D-Biological Crystallography* **70**, 371-383 (2014).

49. R. B. Merrifield, Solid-phase peptide synthesis. An improved synthesis of bradykinin. *Biochemistry* **3**, 1385-1390 (1964).

50. F. Guillier, D. Orain, M. Bradley, Linkers and cleavage strategies in solid-phase organic synthesis and combinatorial chemistry. *Chem Rev* **100**, 2091-2158 (2000).

51. C. F. W. Becker *et al.*, Total chemical synthesis of a functional interacting protein pair: The protooncogene H-Ras and the Ras-binding domain of its effector c-Raf1. *Proceedings of the National Academy of Sciences of the United States of America* **100**, 5075-5080 (2003).

52. J. Offer, C. N. Boddy, P. E. Dawson, Extending synthetic access to proteins with a removable acyl transfer auxiliary. *J Am Chem Soc* **124**, 4642-4646 (2002).

53. T. Dudler, M. H. Gelb, Replacement of the H-Ras farnesyl group by lipid analogues: implications for downstream processing and effector activation in Xenopus oocytes. *Biochemistry* **36**, 12434-12441 (1997).

54. K. Kuhn, Synthesis of Functional Ras Lipoproteins and Fluorescent Derivatives. *J. Am. Chem. Soc.* **123**, 1023-1035 (2001).

55. G. T. Hermanson, *Bioconjugate techniques*. (Academic Press, San Diego, New York, Boston, 1996), pp. 785.

56. B. Bader *et al.*, Bioorganic synthesis of lipid-modified proteins for the study of signal transduction. *Nature* **403**, 223-226 (2000).

57. B. Bader, Bioorganic synthesis of lipid-modifed proteins for the study of signal transduction. *NATURE* **403**, 223-226 (2000).

58. P. E. Dawson, T. W. Muir, I. Clark-Lewis, S. B. Kent, Synthesis of proteins by native chemical ligation. *Science* **266**, 776-779 (1994).

59. T. W. Muir, Semisynthesis of proteins by expressed protein ligation. *Annu Rev Biochem* **72**, 249-289 (2003).

60. R. Hirata *et al.*, Molecular structure of a gene, VMA1, encoding the catalytic subunit of H(+)-translocating adenosine triphosphatase from vacuolar membranes of Saccharomyces cerevisiae. *J Biol Chem* **265**, 6726-6733 (1990).

61. P. M. Kane *et al.*, Protein splicing converts the yeast TFP1 gene product to the 69-kD subunit of the vacuolar H(+)-adenosine triphosphatase. *Science* **250**, 651-657 (1990).

62. S. Chong *et al.*, Single-column purification of free recombinant proteins using a self-cleavable affinity tag derived from a protein splicing element. *Gene* **192**, 271-281 (1997).

63. Z. Liu *et al.*, Structure of the branched intermediate in protein splicing. *Proceedings of the National Academy of Sciences of the United States of America* **111**, 8422-8427 (2014).

64. D. Gottlieb, C. Grunwald, C. Nowak, J. Kuhlmann, H. Waldmann, Intein-mediated in vitro synthesis of lipidated Ras proteins. *Chem Commun (Camb)*, 260-262 (2006).

65. S. Chong *et al.*, Protein splicing involving the Saccharomyces cerevisiae VMA intein. The steps in the splicing pathway, side reactions leading to protein cleavage, and establishment of an in vitro splicing system. *J Biol Chem* **271**, 22159-22168 (1996).

66. P. A. Boriack-Sjodin, S. M. Margarit, D. Bar-Sagi, J. Kuriyan, The structural basis of the activation of Ras by Sos. *Nature* **394**, 337-343 (1998).

67. D. Huster, Membrane Insertion of a Lipidated Ras Peptide Studied by FTIR, Solid-State NMR, and Neutron Diffraction Spectroscopy. *J Am Chem Soc.* **125**, 4070-4079 (2003).

68. A. Vogel *et al.*, Lipid Modifications of a Ras Peptide Exhibit Altered Packing and Mobility versus Host Membrane as Detected by 2H Solid-State NMR. *Journal of the American Chemical Society* **127**, 12263-12272 (2005).

69. S. Janosch *et al.*, Partitioning of dual-lipidated peptides into membrane microdomains: lipid sorting vs peptide aggregation. *J Am Chem Soc* **126**, 7496-7503 (2004).

70. N. M. Hooper, Detergent-insoluble glycosphingolipid/cholesterol-rich membrane domains, lipid rafts and caveolae (review). *Mol Membr Biol* **16**, 145-156 (1999).

71. S. Moffett, D. A. Brown, M. E. Linder, Lipid-dependent targeting of G proteins into rafts. *J Biol Chem* **275**, 2191-2198 (2000).

72. P. Scheiffele, M. G. Roth, K. Simons, Interaction of influenza virus haemagglutinin with sphingolipid-cholesterol membrane domains via its transmembrane domain. *The EMBO Journal* **16**, 5501-5508 (1997).

73. K. A. Melkonian, A. G. Ostermeyer, J. Z. Chen, M. G. Roth, D. A. Brown, Role of Lipid Modifications in Targeting Proteins to Detergent-resistant Membrane Rafts. Many raft proteins are acylated, while few are prenylated 10.1074/jbc.274.6.3910. *J. Biol. Chem.* **274**, 3910-3917 (1999).

74. E. R. Andrew, A. Bradbury, R. G. Eades, Nuclear Magnetic Resonance Spectra from a Crystal rotated at High Speed. *Nature* **182**, 1659-1659 (1958).

75. G. Reuther *et al.*, Structural Model of the Membrane-Bound C Terminus of Lipid-Modified Human N-Ras Protein. *Angewandte Chemie International Edition* **45**, 5387-5390 (2006).

76. G. Cornilescu, F. Delaglio, A. Bax, Protein backbone angle restraints from searching a database for chemical shift and sequence homology. *J Biomol NMR* **13**, 289-302 (1999).

77. A. Meister *et al.*, Insertion of lipidated Ras proteins into lipid monolayers studied by infrared reflection absorption spectroscopy (IRRAS). *Biophysical Journal* **91**, 1388-1401 (2006).

78. A. Meister, Insertion of Lipidated Ras Proteins into Lipid Monolayers Studied by Infrared Reflection Absorption Spectroscopy (IRRAS). *Biophysical Journal* **91**, 1388–1401 (2006).

79. F. Bringezu *et al.*, Membrane binding of a lipidated N-Ras protein studied in lipid monolayers. *European Biophysics Journal with Biophysics Letters* **36**, 491-498 (2007).

80. R. A. Dluhy, D. G. Cornell, In situ measurement of the infrared spectra of insoluble monolayers at the air-water interface. *The Journal of Physical Chemistry* **89**, 3195-3197 (1985).

81. R. Mendelsohn, G. Mao, C. R. Flach, Infrared reflection-absorption spectroscopy: principles and applications to lipid-protein interaction in Langmuir films. *Biochim Biophys Acta* **1798**, 788-800 (2010).

82. J. F. Hancock, R. G. Parton, Ras plasma membrane signalling platforms. *Biochem J* **389**, 1-11 (2005).

83. I. A. Prior *et al.*, GTP-dependent segregation of H-ras from lipid rafts is required for biological activity. *Nature Cell Biology* **3**, 368-375 (2001).

84. H. Niv, O. Gutman, Y. Kloog, Y. I. Henis, Activated K-Ras and H-Ras display different interactions with saturable nonraft sites at the surface of live cells. *Journal of Cell Biology* **157**, 865-872 (2002).

85. A. Vogel *et al.*, Interaction of the human N-Ras protein with lipid raft model membranes of varying degrees of complexity. *Biological Chemistry* **395**, 779-789 (2014).

86. G. Binnig, C. F. Quate, C. Gerber, Atomic force microscope. *Phys Rev Lett* **56**, 930-933 (1986).

87. D. J. Billingsley, W. A. Bonass, N. Crampton, J. Kirkham, N. H. Thomson, Single-molecule studies of DNA transcription using atomic force microscopy. *Phys Biol* **9**, 021001 (2012).

88. C. Nicolini *et al.*, Visualizing Association of N-Ras in Lipid Microdomains: Influence of Domain Structure and Interfacial Adsorption. *Journal of the American Chemical Society* **128**, 192-201 (2006).

89. A. Werkmuller, G. Triola, H. Waldmann, R. Winter, Rotational and Translational Dynamics of Ras Proteins upon Binding to Model Membrane Systems. *Chemphyschem* **14**, 3698-3705 (2013).

90. T. Forster, Intermolecular energy migration and fluorescence. *Ann Phys* **2**, 55-75 (1948).

91. J. R. Lakowicz, *Principles of Fluorescence Spectroscopy*. (Springer, ed. 3rd, 2010), pp. 954.

92. S. A. Hussain, An Introduction to Fluorescence Resonance Energy Transfer (FRET). *Science Journal of Physics* **2012**, (2012).

93. T. Förster, Transfer Mechanisms of Electronic Excitation Energy. *Radiation Research Supplement* **2**, 326-339 (1960).

94. E. L. Elson, E. Fried, J. E. Dolbow, G. M. Genin, Phase separation in biological membranes: integration of theory and experiment. *Annu Rev Biophys* **39**, 207-226 (2010).

95. M. Rao, S. Mayor, Use of Forster's resonance energy transfer microscopy to study lipid rafts. *Biochimica Et Biophysica Acta-Molecular Cell Research* **1746**, 221-233 (2005).

96. E. I. Goksu, J. M. Vanegas, C. D. Blanchette, W. C. Lin, M. L. Longo, AFM for structure and dynamics of biomembranes. *Biochim Biophys Acta* **1788**, 254-266 (2009).

97. M. T. Stöckl, A. Herrmann, Detection of lipid domains in model and cell membranes by fluorescence lifetime imaging microscopy. *Biochimica et Biophysica Acta (BBA) - Biomembranes* **1798**, 1444-1456 (2010).

98. P. Pathak, E. London, Measurement of Lipid Nanodomain (Raft) Formation and Size in Sphingomyelin/POPC/Cholesterol Vesicles Shows TX-100 and Transmembrane Helices Increase

Domain Size by Coalescing Preexisting Nanodomains But Do Not Induce Domain Formation. *Biophysical Journal* **101**, 2417-2425 (2011).

99. S. Chiantia, E. London, Sphingolipids and membrane domains: recent advances. *Handb Exp Pharmacol*, 33-55 (2013).

100. G. W. Feigenson, J. T. Buboltz, Ternary Phase Diagram of Dipalmitoyl-PC/Dilauroyl-PC/Cholesterol: Nanoscopic Domain Formation Driven by Cholesterol. *Biophysical Journal* **80**, 2775-2788 (2001).

101. R. S. Petruzielo, F. A. Heberle, P. Drazba, J. Katsaras, G. W. Feigenson, Phase behavior and domain size in sphingomyelin-containing lipid bilayers. *Biochim Biophys Acta* **1828**, 1302-1313 (2013).

102. A. G. Ayuyan, F. S. Cohen, Raft composition at physiological temperature and pH in the absence of detergents. *Biophys J* **94**, 2654-2666 (2008).

103. G. Kragol, M. Lumbierres, J. M. Palomo, H. Waldmann, Solid-phase synthesis of lipidated peptides. *Angew Chem Int Ed Engl* **43**, 5839-5842 (2004).

104. L. Brunsveld, J. Kuhlmann, H. Waldmann, Synthesis of palmitoylated Ras-peptides and proteins. *Methods* **40**, 151-165 (2006).

105. L. Brunsveld *et al.*, Lipidated Ras and Rab peptides and proteins - Synthesis, structure, and function. *Angewandte Chemie-International Edition* **45**, 6622-6646 (2006).

106. M. Volkert *et al.*, Synthesis and biological activity of photoactivatable N-ras peptides and proteins. *J Am Chem Soc* **125**, 12749-12758 (2003).

107. C. Rosenbaum, Solid phase synthesis of cyclic peptides by oxidative cyclative cleavage of an aryl hydrazide linker—synthesis of stylostatin 1. *Tetrahedron Letters* **42**, 5677–5680 (2001).

108. D. A. Brown, E. London, Functions of lipid rafts in biological membranes. *Annual Review of Cell and Developmental Biology* **14**, 111-136 (2003).

109. G. Triola, L. Brunsveld, H. Waldmann, Racemization-free synthesis of S-alkylated cysteines via thiol-ene reaction. *J Org Chem* **73**, 3646-3649 (2008).

110. M. Lumbierres, J. M. Palomo, G. Kragol, H. Waldmann, Solid-phase synthesis of palmitoylated and farnesylated lipopeptides employing the fluoride-labile PTMSEL linker. *Tetrahedron Letters* **47**, 2671-2674 (2006).

111. J. Gureasko *et al.*, Role of the histone domain in the autoinhibition and activation of the Ras activator Son of Sevenless. *Proceedings of the National Academy of Sciences of the United States of America* **107**, 3430-3435 (2010).

112. T. Connolly, P. J. Rapiejko, R. Gilmore, Requirement of Gtp Hydrolysis for Dissociation of the Signal Recognition Particle from Its Receptor. *Science* **252**, 1171-1173 (1991).

113. C. Lenzen *et al.*, in *Methods in Enzymology*. (Academic Press, 1995), vol. 255, pp. 95-109.

114. N. Kahya, D. Scherfeld, K. Bacia, B. Poolman, P. Schwille, Probing lipid mobility of raft-exhibiting model membranes by fluorescence correlation spectroscopy. *J Biol Chem* **278**, 28109-28115 (2003).

115. M. L. Frazier, J. R. Wright, A. Pokorny, P. F. Almeida, Investigation of domain formation in sphingomyelin/cholesterol/POPC mixtures by fluorescence resonance energy transfer and Monte Carlo simulations. *Biophys J* **92**, 2422-2433 (2007).

116. P. Pathak, E. London, Measurement of lipid nanodomain (raft) formation and size in sphingomyelin/POPC/cholesterol vesicles shows TX-100 and transmembrane helices increase domain size by coalescing preexisting nanodomains but do not induce domain formation. *Biophysical Journal* **101**, 2417-2425 (2011).

117. O. Bakht, P. Pathak, E. London, Effect of the structure of lipids favoring disordered domain formation on the stability of cholesterol-containing ordered domains (lipid rafts): Identification of multiple raft-stabilization mechanisms. *Biophysical Journal* **93**, 4307-4318 (2007).

118. A. A. Brian, H. M. McConnell, Allogeneic stimulation of cytotoxic T cells by supported planar membranes. *Proc Natl Acad Sci U S A* **81**, 6159-6163 (1984).

119. M. E. Fastenberg, H. Shogomori, X. Xu, D. A. Brown, E. London, Exclusion of a transmembrane-type peptide from ordered-lipid domains (rafts) detected by fluorescence quenching: extension of quenching analysis to account for the effects of domain size and domain boundaries. *Biochemistry* **42**, 12376-12390 (2003).

120. B. Rotblat *et al.*, Three separable domains regulate GTP-dependent association of H-ras with the plasma membrane. *Molecular and Cellular Biology* **24**, 6799-6810 (2004).

121. A. J. Garcia-Saez, S. Chiantia, P. Schwille, Effect of line tension on the lateral organization of lipid membranes. *J Biol Chem* **282**, 33537-33544 (2007).

122. T. Parasassi, E. Gratton, H. Zajicek, M. Levi, W. Yu, Detecting membrane lipid microdomains by two-photon fluorescence microscopy. *IEEE Eng Med Biol Mag* **18**, 92-99 (1999).

123. C. K. Haluska *et al.*, Combining fluorescence lifetime and polarization microscopy to discriminate phase separated domains in giant unilamellar vesicles. *Biophys J* **95**, 5737-5747 (2008).

124. D. Abankwa, A. A. Gorfe, J. F. Hancock, Mechanisms of Ras membrane organization and signaling: Ras on a rocker. *Cell Cycle* **7**, 2667-2673 (2008).

125. D. Abankwa *et al.*, A novel switch region regulates H-ras membrane orientation and signal output. *EMBO Journal* **27**, 727-735 (2008).

126. A. Vogel *et al.*, Interaction of the human N-Ras protein with lipid raft model membranes of varying degrees of complexity. *Biol Chem* **395**, 779-789 (2014).

127. C. Nicolini, Visualizing Association of N-Ras in Lipid Microdomains: Influence of Domain Structure and Interfacial Adsorption. *J. AM. CHEM. SOC.* **128**, 192-201 (2006).

128. M. J. Karnovsky, A. M. Kleinfeld, R. L. Hoover, R. D. Klausner, The concept of lipid domains in membranes. *J Cell Biol* **94**, 1-6 (1982).

129. F. Wunderlich, W. Kreutz, P. Mahler, A. Ronai, G. Heppeler, Thermotropic fluid goes to ordered "discontinuous" phase separation in microsomal lipids of Tetrahymena. An X-ray diffraction study. *Biochemistry* **17**, 2005-2010 (1978).

130. D. A. Brown, E. London, Functions of lipid rafts in biological membranes. *Annual Review of Cell and Developmental Biology* **14**, 111-136 (1998).

131. V. Kiessling, C. Wan, L. K. Tamm, Domain coupling in asymmetric lipid bilayers. *Biochimica et Biophysica Acta (BBA) - Biomembranes* **1788**, 64-71 (2009).

132. D. Lingwood, K. Simons, Lipid rafts as a membrane-organizing principle. *Science* **327**, 46-50 (2010).

133. M. Takeda, G. P. Leser, C. J. Russell, R. A. Lamb, Influenza virus hemagglutinin concentrates in lipid raft microdomains for efficient viral fusion. *Proc Natl Acad Sci U S A* **100**, 14610-14617 (2003).

134. M. Sargiacomo, M. Sudol, Z. Tang, M. P. Lisanti, Signal transducing molecules and glycosyl-phosphatidylinositol-linked proteins form a caveolin-rich insoluble complex in MDCK cells. *J Cell Biol* **122**, 789-807 (1993).

135. J. F. Hancock, Ras Proteins: Different Signals from Different Locations. *Nature Reviews Molecular Cell Biology* **4**, 373-385 (2003).

136. I. A. Prior, J. F. Hancock, Compartmentalization of Ras proteins. *J Cell Sci* **114**, 1603-1608 (2001).

137. L. Janosi, Z. L. Li, J. F. Hancock, A. A. Gorfe, Organization, dynamics, and segregation of Ras nanoclusters in membrane domains. *Proceedings of the National Academy of Sciences of the United States of America* **109**, 8097-8102 (2012).

138. R. Varma, S. Mayor, GPI-anchored proteins are organized in submicron domains at the cell surface. *Nature* **394**, 798-801 (1998).

139. A. Pralle, P. Keller, E. L. Florin, K. Simons, J. K. Horber, Sphingolipid-cholesterol rafts diffuse as small entities in the plasma membrane of mammalian cells. *J Cell Biol* **148**, 997-1008 (2000).

140. B. Ludolph, F. Eisele, H. Waldmann, Solid-phase synthesis of lipidated peptides. *J Am Chem Soc* **124**, 5954-5955 (2002).

141. A. A. Gorfe, M. Hanzal-Bayer, D. Abankwa, J. F. Hancock, J. A. McCammon, Structure and Dynamics of the Full-Length Lipid-Modified H-Ras Protein in a 1,2-Dimyristoylglycero-3-phosphocholine Bilayer. *J. Med. Chem.* **50**, 674-684 (2007).

142. S. L. Campbell-Burk, J. W. Carpenter, in *Small GTPases and Their Regulators, Part A: RAS Family,* W. E. Balch, C. J. Der, A. Hall, Eds. (Academic Press, 1995), pp. 3-13.

143. E. A. Kovrigina, A. R. Galiakhmetov, E. L. Kovrigin, Ras G domain lacks intrinsic propensity to form dimers. *Biophysical Journal* **109**, 1000-1008 (2015).

144. A. Hall, A. J. Self, The effect of Mg2+ on the guanine nucleotide exchange rate of p21N-ras. *J. Biol. Chem.* **261**, 10963-10965 (1986).

145. J. John *et al.*, Kinetics of interaction of nucleotides with nucleotide-free H-ras p21. *Biochemistry* **29**, 6058-6065 (1990).

146. J. N. Israelachvili, D. J. Mitchell, A model for the packing of lipids in bilayer membranes. *Biochim Biophys Acta* **389**, 13-19 (1975).

147. G. J. Schutz, G. Kada, V. P. Pastushenko, H. Schindler, Properties of lipid microdomains in a muscle cell membrane visualized by single molecule microscopy. *Embo J* **19**, 892-901 (2000).

148. S. Mayor, F. R. Maxfield, Insolubility and redistribution of GPI-anchored proteins at the cell surface after detergent treatment. *Mol Biol Cell* **6**, 929-944 (1995).

149. M. Hao, S. Mukherjee, F. R. Maxfield, Cholesterol depletion induces large scale domain segregation in living cell membranes. *Proc Natl Acad Sci U S A* **98**, 13072-13077 (2001).

150. F. J. Hutchinson, S. E. Francis, I. G. Lyle, M. N. Jones, The characterisation of liposomes with covalently attached proteins. *Biochim Biophys Acta* **978**, 17-24 (1989).

151. J. N. Israelachvili, D. J. Mitchell, Model for Packing of Lipids in Bilayer Membranes. *Biochimica Et Biophysica Acta* **389**, 13-19 (1975).

Appendix A Supplementary Tables and Figures

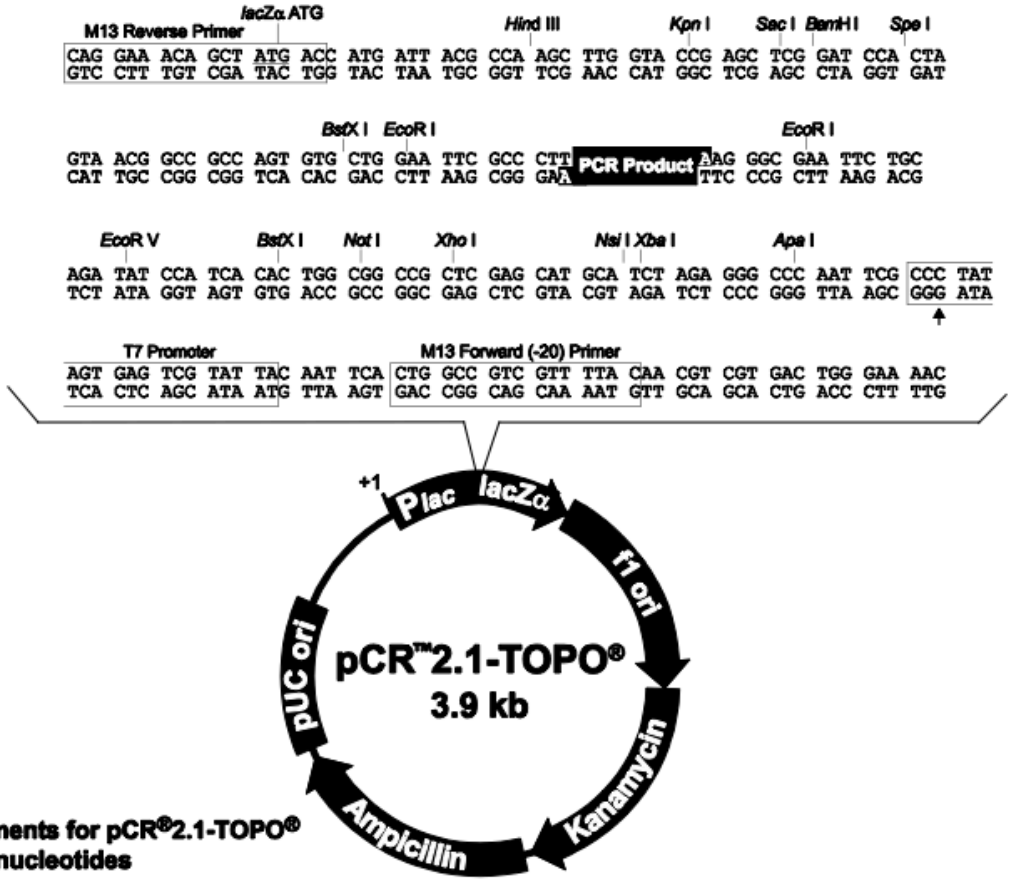

Figure 4-2 pCR 2.1-TOPO vector map. Image from www.neb.com

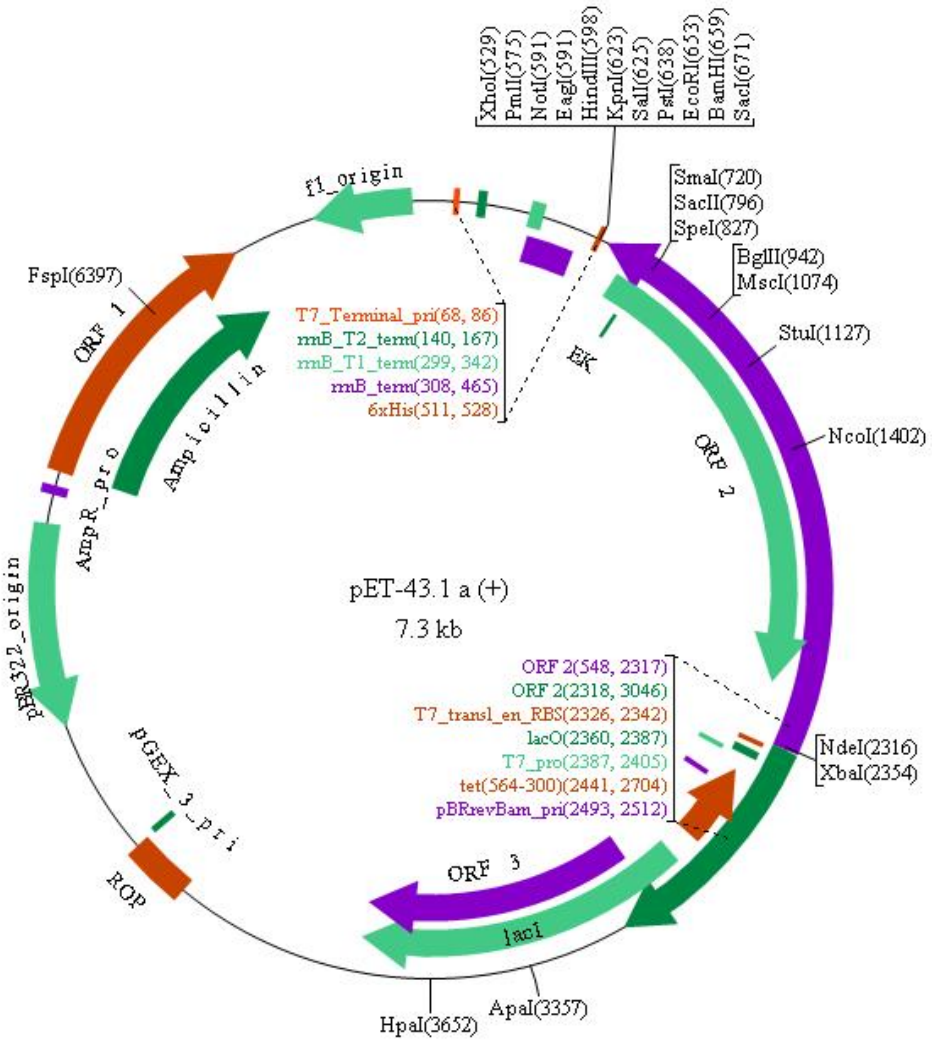

Figure 4-3 pET43.1a(+) vector map. Image from www.neb.com

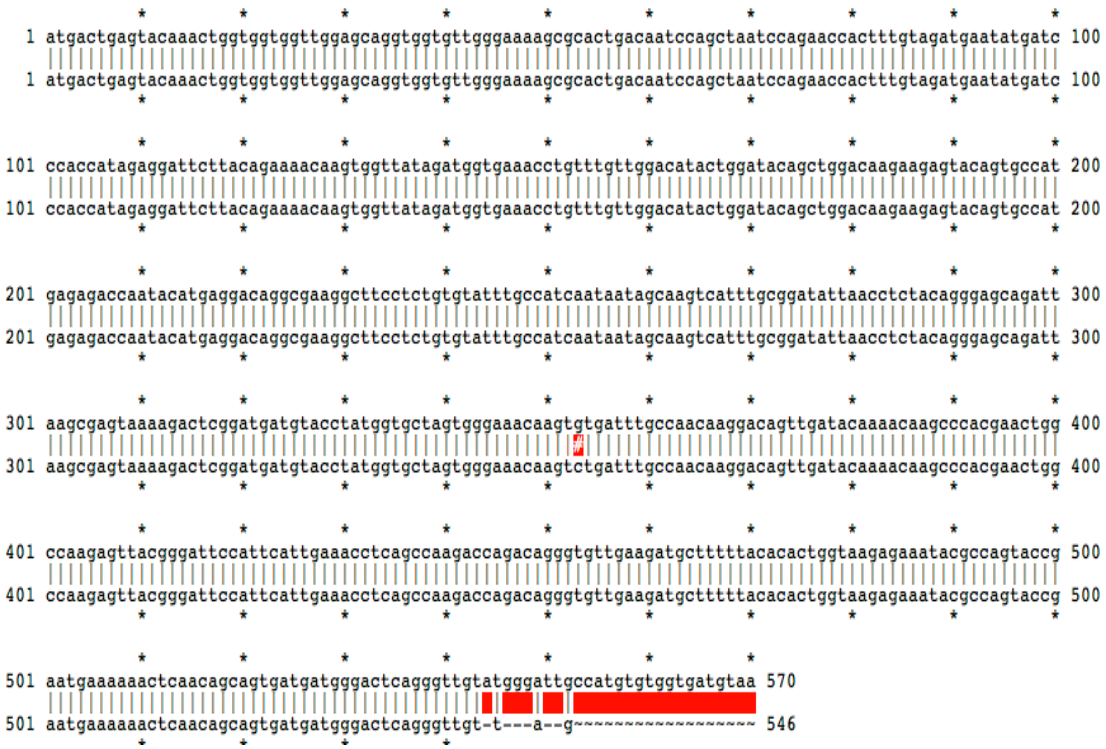

Figure 4-4 Sequence alignment of human *N*-Ras wild type protein (NCBI reference sequence NM_002524.4) (top) and *N*-RasC118S-181C construct (bottom)

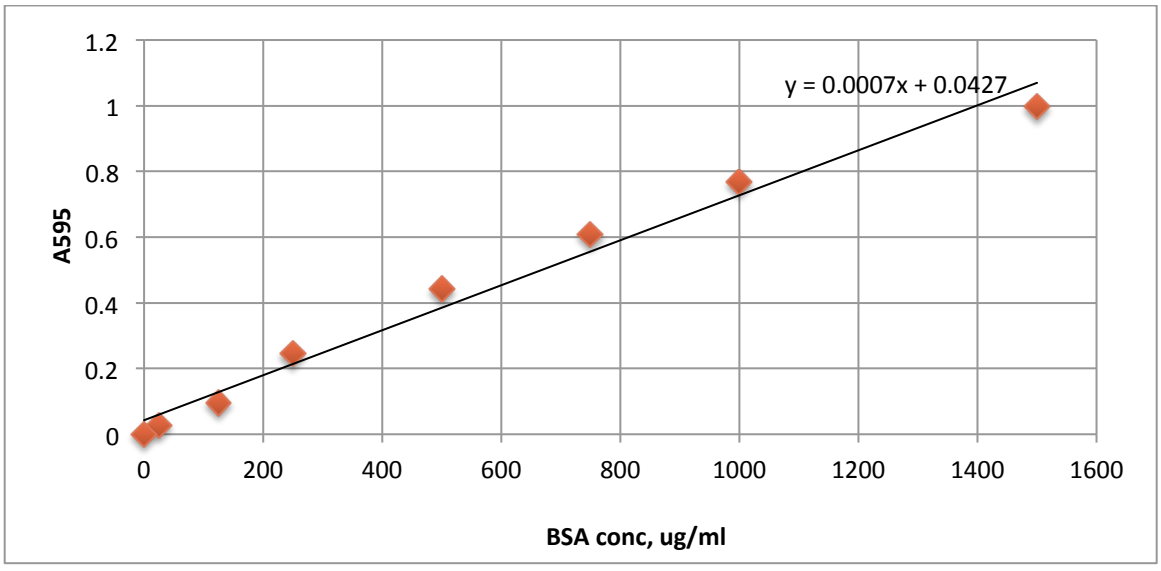

Figure 4-5 BSA calibration curve for 25-1500 µg/mL working range

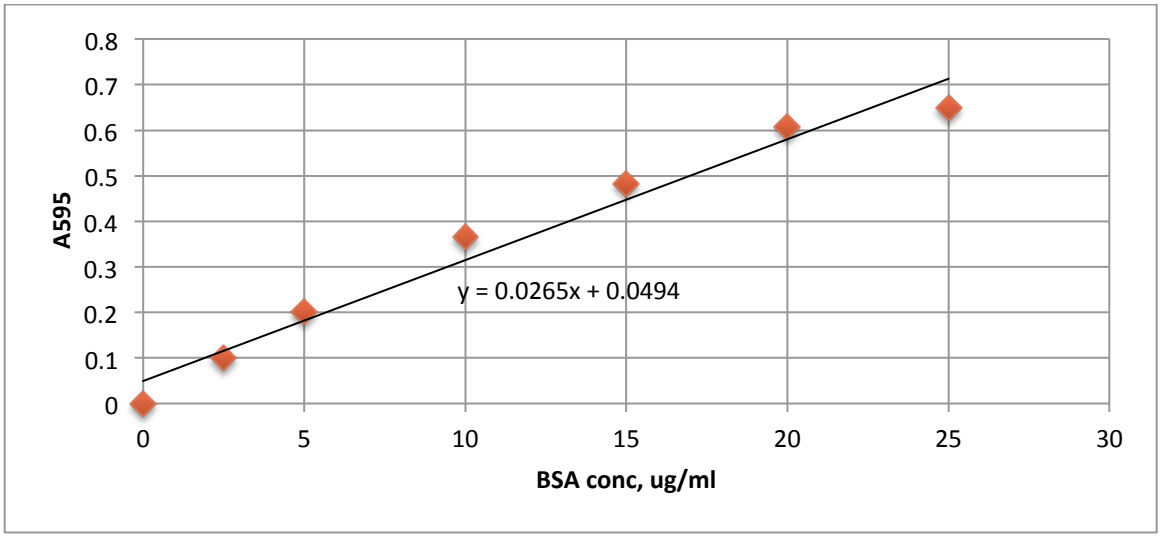

Figure 4-6 BSA calibration curve for 1-25 μg/mL working range

Appendix B Lifetimes data

Table 4-7 Lifetimes of free mant nucleotides

Nucleotide	1	2	3	4	Avg
MantGDP	4.17	4.34	4.43	4.29	4.31
MantGppNHp	4.18	4.24	4.5	3.68	4.15

Life Times of Mant Fluorophore in Ras Lipoprotein Samples

Standard deviations and number of replicates for each measurement are given in parentheses. FRET efficiency values and their standard deviation were calculated using Eq. 1 and Eq. 2.

Table 4-8 Life times of mant fluorophore in *N*-Ras lipoprotein samples loaded with mGDP and mGppNHp associated with homogeneous and lipid raft membranes

N-Ras•mGDP			
Lipid mix	Homogeneous LUVs	Raft LUVs	
Temperature	5 °C	5 °C	16 °C
Lifetime F_0, ns	*7.47* *(0.01, 4)*	*5.28* *(0.05, 4)*	5.16 (0.13, 2)
Lifetime F, ns	*6.45* *(0.04, 3)*	*5.29* *(0.02, 4)*	5.17 (0.15, 2)
FRET Efficiency	*0.137* *(0.005)*	*-0.002* *(0.010)*	*-0.002* *(0.04)*

N-Ras•mGppNHp			
Lipid mix	Homogeneous LUVs	Raft LUVs	
Temperature	5 °C	5 °C preparation 1	5°C preparation 2
Lifetime F_0, ns (τ_D)	*8.92* *(0.04, 4)*	*7.87* *(0.15, 4)*	*6.56* *(0.04, 2)*

Lifetime F, ns (τ_{DA})	*7.35* *(0.05, 3)*	*6.90* *(0.1, 4)*	*5.43* *(0.07, 2)*
FRET Efficiency	*0.176* *(0.007)*	*0.123* *(0.021)*	*0.172* *(0.012)*

Table 4-9 Life times of mant fluorophore in H-Ras "chimera" samples (*H*-Ras G-domain coupled with *N*-Ras *C*-terminal lipopeptide) loaded with mGDP and mGppNHp associated with homogeneous and lipid raft membranes

H-Ras_chimera•mGDP			
Lipid mix	Homogeneous LUVs	Raft LUVs	
Temperature	5 ^{o}C	5 ^{o}C	15 ^{o}C
Lifetime F_0, ns	*7.87* *(0.01, 4)*	*8.02* *(0.05, 4)*	7.63 (0.13, 4)
Lifetime F, ns	*6.76* *(0.04, 4)*	*5.55* *(0.02, 4)*	5.87 (0.24, 4)
FRET Efficiency	*0.139* *(0.005)*	*0.312* *(0.010)*	*0.23* *(0.04)*
H-Ras_chimera•mGppNHp			

Lipid mix	Homogeneous LUVs	Raft LUVs	
Temperature	5 °C	5 °C	16°C
Lifetime F_0, ns (τ_D)	*7.99* *(0.04, 4)*	*8.49* *(0.14, 4)*	*8.39* *(0.1, 4)*
Lifetime F, ns (τ_{DA})	*5.84* *(0.09, 4)*	*6.46* *(0.1, 4)*	*6.40* *(0.24, 4)*
FRET Efficiency	*0.27* *(0.007)*	*0.24* *(0.028)*	*0.24* *(0.022)*

Table 4-10 Life times of mant fluorophore in *N*-Ras lipoprotein samples loaded with mGDP and mGppNHp associated with homogeneous and lipid raft membranes at high temperatures

N-Ras•mGDP		
Lipid mix	Homogeneous LUVs	Raft LUVs
Temperature	37 °C	37 °C
Lifetime F_0, ns	*5.05 (0.12, 4)*	*3.63 (0.16, 4)*
Lifetime F, ns	*4.29 (0.15, 4)*	*3.57 (0.12, 4)*
FRET Efficiency	*0.15 (0.04)*	*0.02 (0.06)*

N-Ras•mGppNHp		
Lipid mix	Homogeneous LUVs	Raft LUVs
Temperature	37 °C	37 °C
Lifetime F_0, ns (τ_D)	*3.94* *(0.20, 4)*	*3.97* *(0.13, 4)*
Lifetime F, ns (τ_{DA})	*3.95* *(0.10, 3)*	*3.86* *(0.15, 4)*
FRET Efficiency	*0.01* *(0.06)*	*0.03* *(0.05)*

Table 4-11 Life times of mant fluorophore in *H*-Ras chimera lipoprotein samples loaded with mGDP and mGppNHp associated with homogeneous and lipid raft membranes at high temperatures

H-Ras•mGDP chimera							
Lipid mix	Homogeneous LUVs						
Temperature	10 °C	15 °C	20 °C	25 °C	30 °C	35 °C	40 °C
Lifetime F_0, ns	*7.33 (0.18, 4)*	*7.28 (0.20, 4*	*7.00 (0.28, 4*	*6.43 (0.06, 4*	*5.97 (0.09, 4*	*5.42 (0.16, 4*	*4.70 (0.30, 4*

Lifetime F, ns	*6.55 (0.07, 4)*	*6.38 (0.09, 4*	*5.95 (0.12, 4*	*5.74 (0.16, 4*	*5.21 (0.44, 4*	*4.95 (0.15, 4*	*4.53 (0.15, 4*
FRET Efficiency	*0.11 (0.02)*	*0.12 (0.03)*	*0.1 (0.04)*	*0.11 (0.03)*	*0.13 (0.07)*	*0.09 (0.04)*	*0.03 (0.07)*
H-Ras•mGDP chimera							
Lipid mix	Raft LUVs						
Temperature	10 °C	15 °C	20 °C	25 °C	30 °C	35 °C	40 °C
Lifetime F_0, ns	*7.38 (0.36, 4)*	*7.63 (0.17, 4*	*6.29 (0.29, 4*	*6.13 (0.10, 4*	*5.72 (0.59, 4*	*4.19 (0.70, 4*	*5.01 (0.70, 4*
Lifetime F, ns	*5.60 (0.38, 4)*	*5.87 (0.24, 4*	*5.44 (0.53, 4*	*4.71 (0.41, 4*	*5.31 (0.17, 4*	*4.66 (0.09, 4*	-
FRET Efficiency	*0.24 (0.06)*	*0.23 (0.04)*	*0.14 (0.09)*	*0.23 (0.07)*	*0.07 (0.10)*	*0.07 (0.19)*	-

H-Ras• mGppNHp chimera							
Lipid mix	Homogeneous LUVs						
Temperature	10 °C	15 °C	20 °C	25 °C	30 °C	35 °C	40 °C
Lifetime F_0, ns	*7.57 (0.34, 4)*	*7.63 (0.13, 4*	*7.57 (0.31, 4*	*7.03 (0.09, 4*	*5.84 (0.06, 4*	*4.66 (0.33, 4*	*3.97 (0.11, 4*

Lifetime F, ns	*5.74 (0.15, 4)*	*5.63 (0.12, 4*	*5.39 (0.12, 4*	*5.00 (0.18, 4*	*4.60 (0.18, 4*	*4.24 (0.13, 4*	*4.13 (0.04, 4*
FRET Efficiency	*0.24 (0.04)*	*0.26 (0.02)*	*0.29 (0.03)*	*0.29 (0.03)*	*0.21 (0.03)*	*0.09 (0.07)*	*0.04 (0.03)*
H-Ras• mGppNHp chimera							
Lipid mix	Raft LUVs						
Temperature	10 °C	15 °C	20 °C	25 °C	30 °C	35 °C	40 °C
Lifetime F_0, ns	*7.57 (0.34, 4)*	*7.63 (0.13, 4*	*7.57 (0.31, 4*	*7.03 (0.09, 4*	*5.84 (0.06, 4*	*4.66 (0.33, 4*	*3.97 (0.11, 4*
Lifetime F, ns	*5.74 (0.15, 4)*	*5.63 (0.12, 4*	*5.39 (0.12, 4*	*5.00 (0.18, 4*	*4.60 (0.18, 3*	*4.24 (0.13, 3*	*4.13 (0.04. 4)*
FRET Efficiency	*0.24 (0.04)*	*0.26 (0.02)*	*0.29 (0.03)*	*0.29 (0.03)*	*0.21 (0.03)*	*0.09 (0.07)*	*0.04 (0.03)*

Table 4-12 Life times of mant fluorophore in *N*-Ras lipoprotein samples loaded with mGDP associated with lipid raft membranes at 5 °C in experiment with the nucleotide exchange of the protein attached to membrane mimic

N-Ras•mGDP		
Lipid mix	Raft LUVs	
Temperature	5 °C before exchange	5 °C after exchange

Lifetime F_0, ns	*5.59* *(0.16, 4)*	*4.98* *(0.13, 4)*
Lifetime F, ns	*4.73* *(0.08, 4)*	*4.82* *(0.15, 4)*
FRET Efficiency	*0.16* *(0.05)*	*0.03* *(0.08)*

Appendix C Contribution of Non-Specific Binding of Mant-Nucleotides to LUV

In control experiments we used unlabeled homogenous LUVs. All conditions (elution buffer, flow rate, sample volume) were kept identical to avoid artifacts and make elution profiles comparable. The very first control sample contained a mixture of homogenous LUVs with Mant-GDP nucleotide incubated overnight. As expected, Mant-GDP was eluted in a small molecules range. Only based on elution profile we cannot exclude non-specific interaction of the nucleotide with LUV, therefore emission intensities of mant-group were compared (see below).

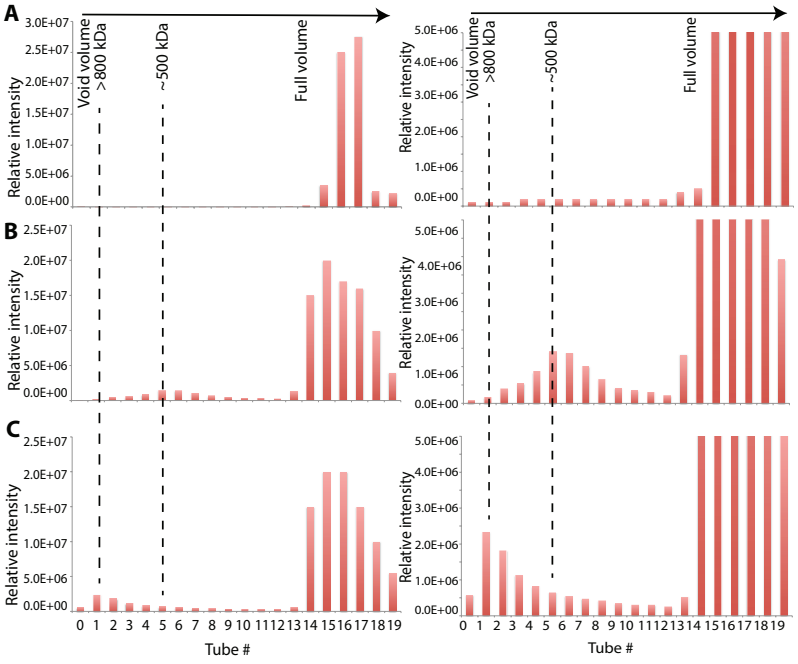

Figure 4-7 Relative intensity of mant-signal in elution tubes for control injections. A) homogeneous LUVs with Mant-GDP mixture; B) lipidated NRas-MantGDP; C) lipidated NRas-MantGDP with homogeneous LUVs

Second control sample represented by a lipidated N-Ras protein labeled with Mant-GDP in absence of LUVs. The protein was eluted at a molecular weight of approximately 500 kDa probably due to formation of aggregates.

Third control experiment represented an example reaction of lipidated protein with LUV. As illustrated in Figure 4-7, the relative intensity of mant-group is shifted towards high molecular weight suggesting the insertion of the lipidated protein into membrane mimic. Comparing elution profiles B and C we cannot exclude absence of lipidated Ras aggregates (500 kDa weight) in LUV-protein complex elution tubes, therefore the contribution of that fraction was estimated below.

Appendix D Contribution of Non-Specific Binding of Mant-Nucleotides to LUV

There is no evidence of specific interaction between the nucleotides and lipid vesicles, due to the difference in polarity. Therefore, the “passive diffusion” is not the case. However, if the molecule is small enough it may be “trapped” between the LUVs or absorbed at the surface of LUV and therefore travel along them during the elution. To estimate the contribution of this effect in our particular system both lipid mixtures were examined: homogeneous and raft LUVs. In addition, the amount of non-specifically bounded GDP and GppNHp mant-derivatives was estimated.

Mant-GDP/Homogeneous LUVs

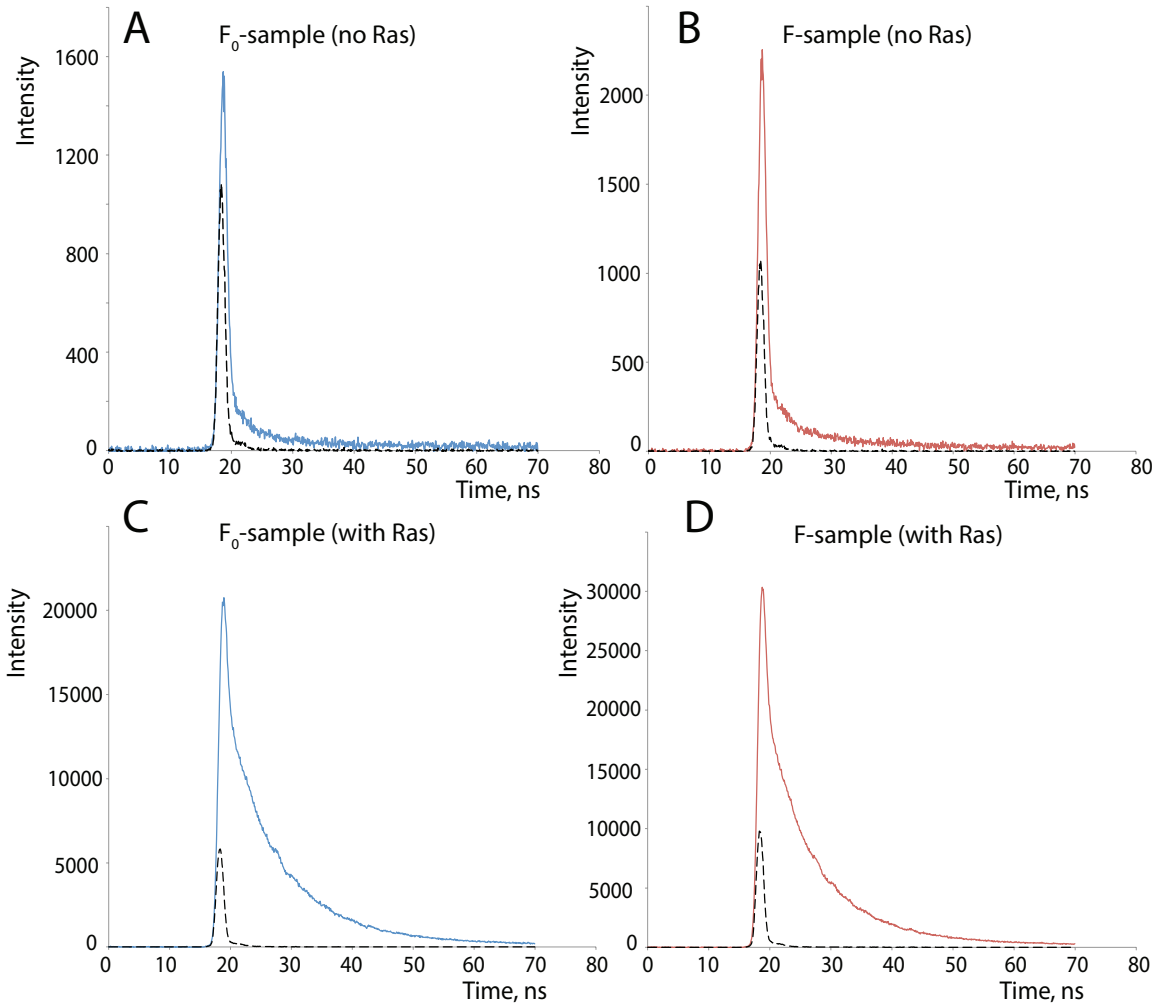

Figure 4-8 Test for MantGDP association with homogeneous LUVs. The decays for the following samples are pictured: A = F_0 sample in absence of lipidated NRas (F_0) t= 4.51ns (2.1%), B= F sample in absence of lipidated NRas (F) t=6.3 ns (2.2%), C= F_0 sample in presence of lipidated NRas (F_0-NRas) t=7.5 ns (27.1%), D = F sample in presence of lipidated NRas (F-NRas) t=6.5 ns (20.2%)

Mant- GDP /Raft LUVs

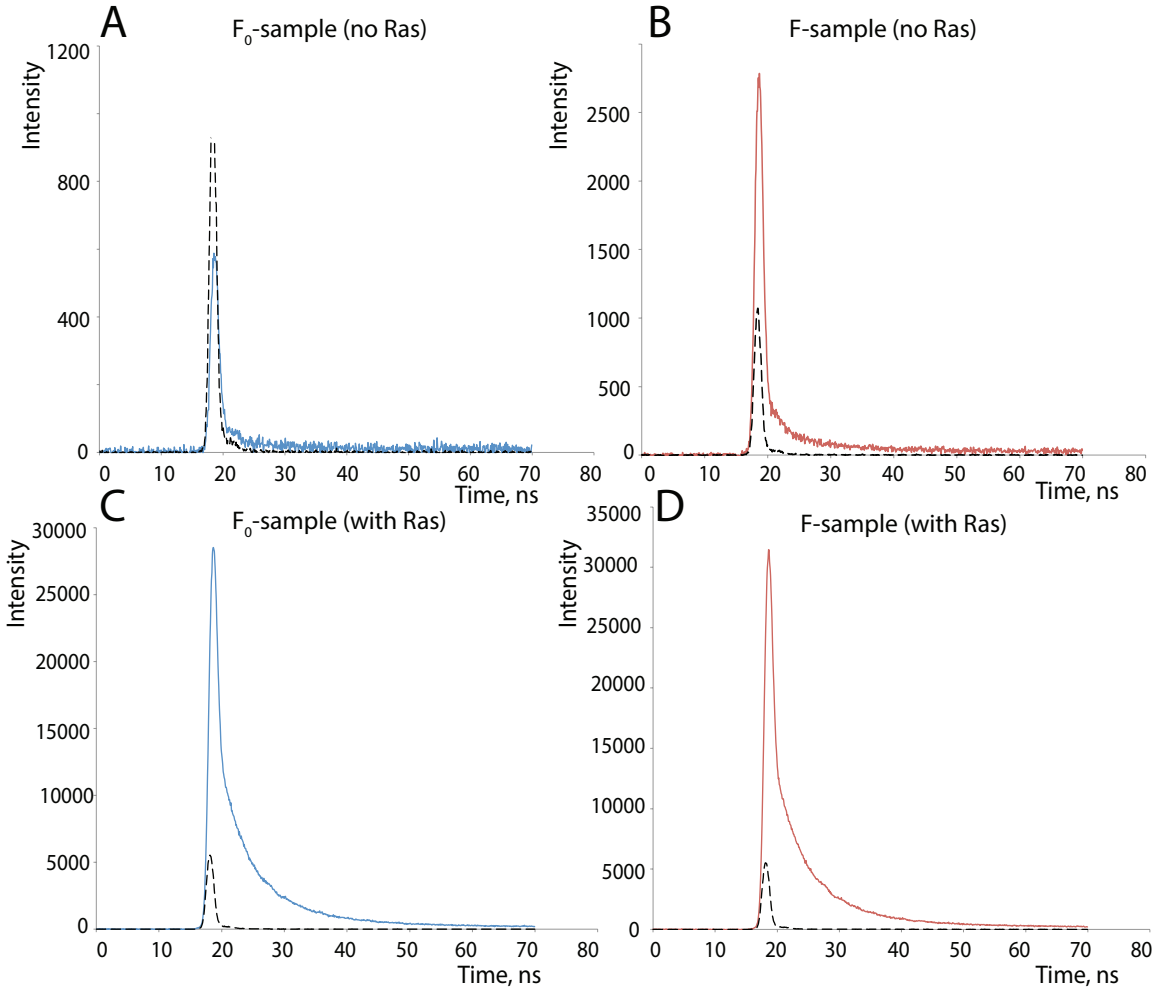

Figure 4-9 Test for MantGDP association with raft LUVs. The decays for the following samples are pictured: A = F_0 t=4.9 ns (1.7%), B= F t=4.7 ns (1.6%), C= F_0-NRas t=5.5 ns (17.8%), D = F-NRas t=5.5 ns (13.0%)

Mant- GppNHp /Homogeneous LUVs

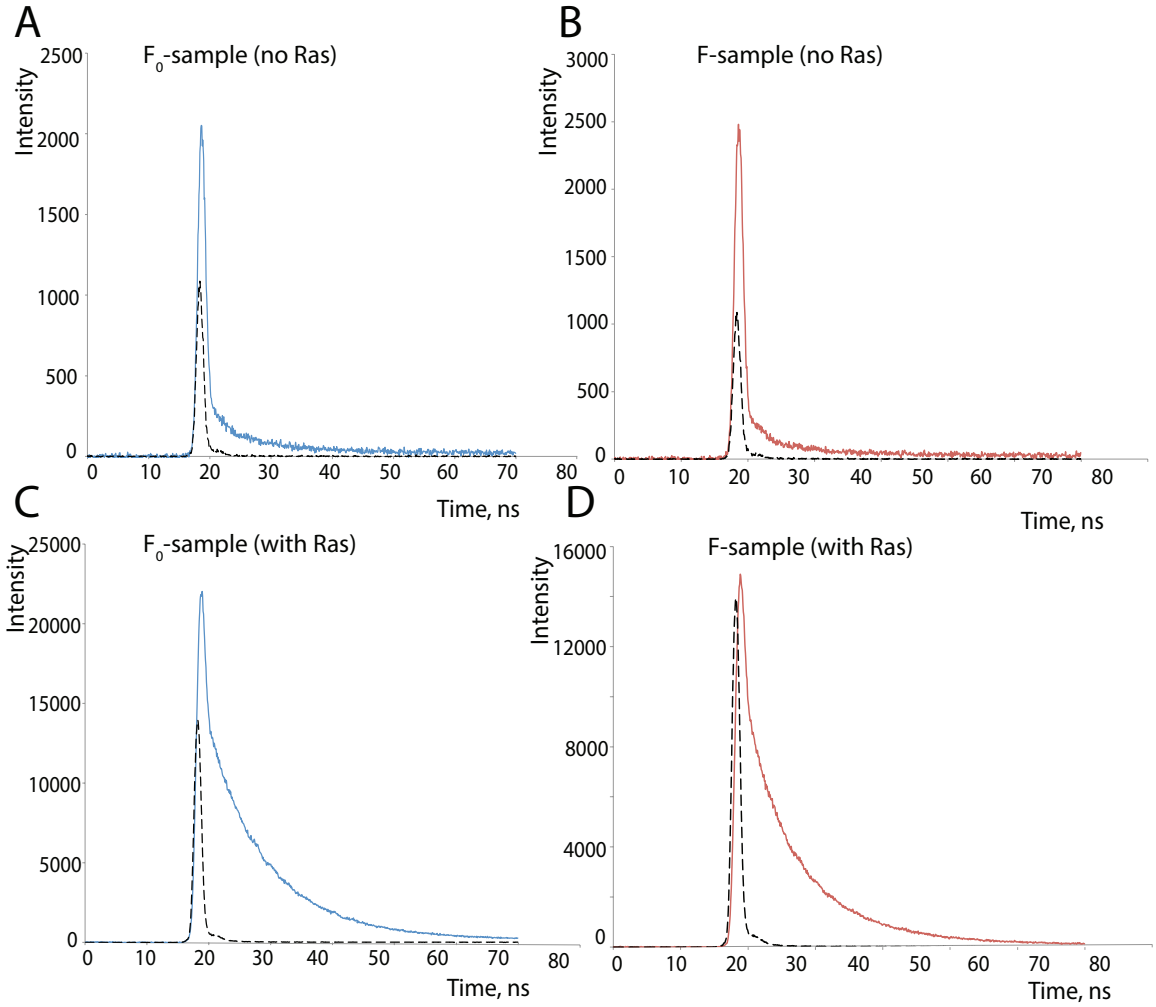

Figure 4-10 Test for MantGppNHp association with homogeneous LUVs. The decays for the following samples are pictured: A = F_0 t=7.1 ns (2.4%), B= F t=5.6 ns (1.6%), C= F_0-NRas t=8.9 ns (27.5%), D = F-NRas t=7.3 ns (35.9%)

Mant- GppNHp / Raft LUVs

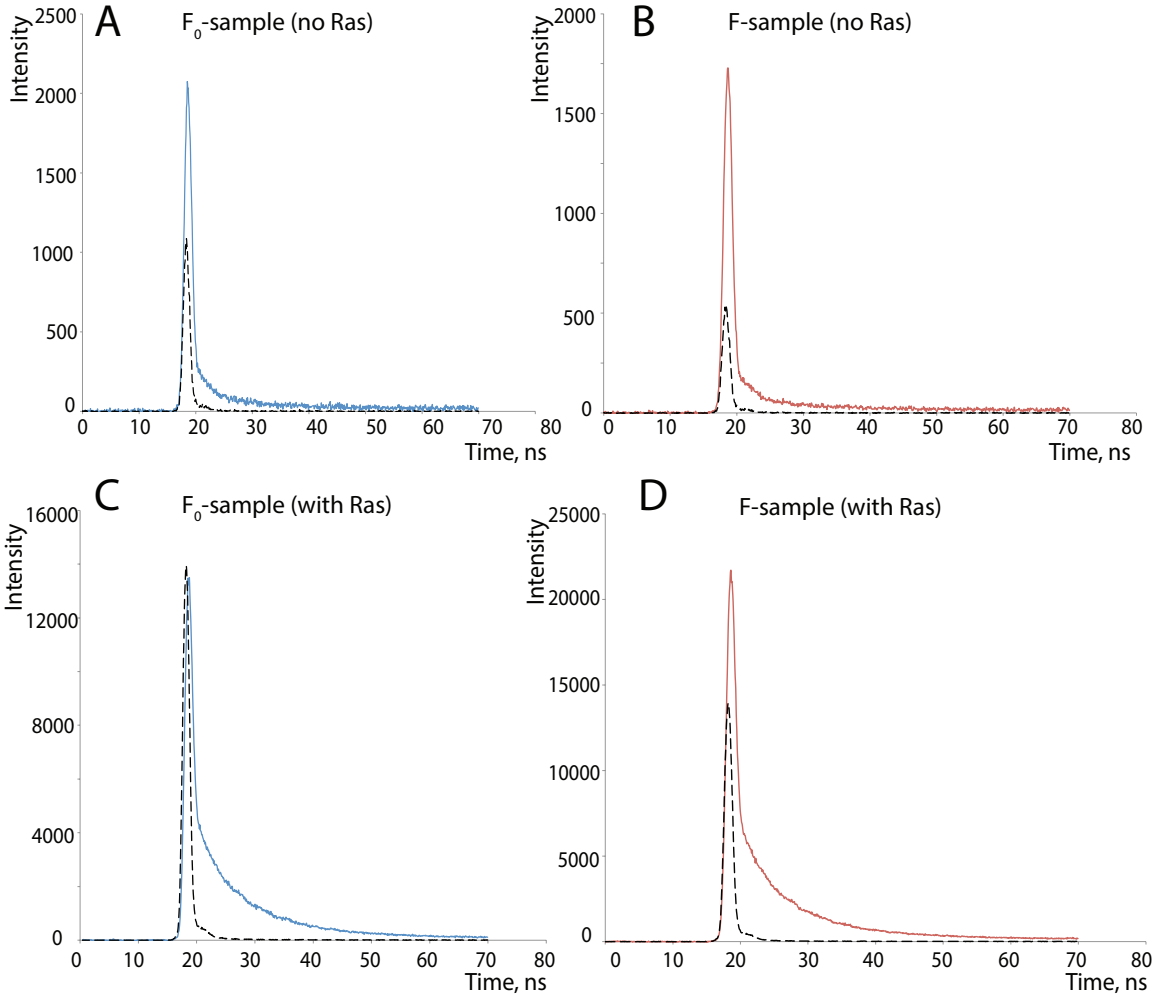

Figure 4-11 Test for MantGppNHp association with raft LUVs. The decays for the following samples are pictured: A = F_0 t=5.3 ns (1.8%), B= F t=6.2 ns (1.2%), C= F_0-NRas t=7.9 ns (10.1%), D = F-NRas t=6.9 ns (9.3%)

Conclusion: contribution of free Mant non-specifically bounded to LUVs is about 2%.

Appendix E Contribution of the Lipidated Protein Unassociated with LUVs

To estimate the percentage of mant signal from aggregated lipidated *N*-Ras non-associated with LUVs the emission intensities of mant-group in tubes corresponding to LUV fraction were compared. The contribution of scattering was taken into account by subtraction of a blank buffer trace from both traces.

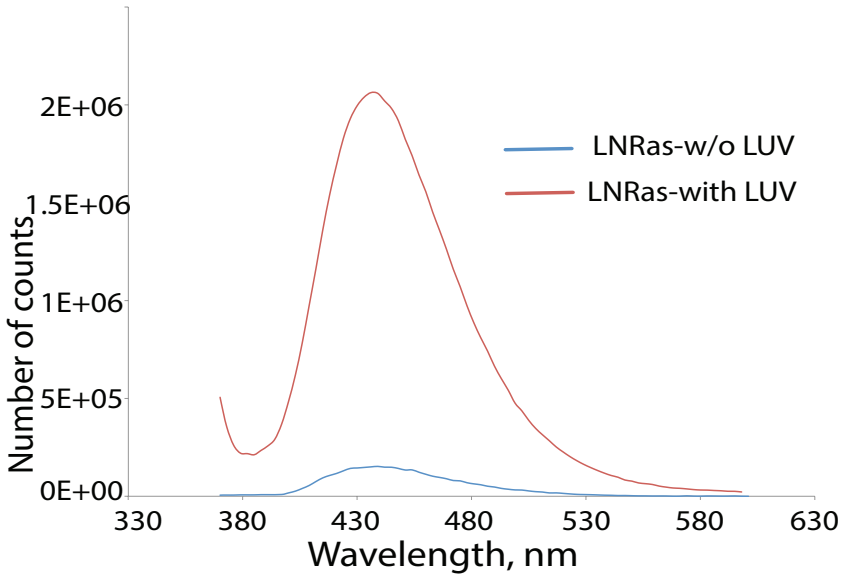

Figure 4-12 Emission intensity of mant in "LUV" tubes in protein-LUV mixture and protein-only solution

The percentage of LUV-unassociated mant was calculated as

%unassociated mant = $60000/2.1E+06$ = 2.8%.

Conclusion: contribution of Mant unassociated with LUVs in Ras-LUV samples is about 3%.

Appendix F Calculation of the Surface Density for Lipidated Peptide Added to LUVs

Using membrane size of 0.2 μm (known from an extruder membrane pore size), we estimated the radius of LUV as 100 nm;

Therefore LUV surface area = $4\pi r^2 = 12.6 * 10^4\ nm^2 = 0.126\ \mu m^2$

Surface area of the lipid (avg) = 0.7 nm^2 was estimated by Israelachvili and Mitchel (*146*);

Number of surface lipid per LUV $= 1.8 * 10^5\ lipids$

Number of peptide molecules per LUV =

$\frac{\%\ of\ peptide\ added}{100} * Number\ of\ surface\ lipids\ per\ LUV$

Surface density = $\frac{Number\ of\ molecules\ per\ LUV}{Surface\ area\ of\ LUV}$

% of peptide added	Number of molecules per LUVs	Surface density, molecules/ μ m^2
0.1%	180	1400
0.5%	890	7100

Appendix G Estimation of Number of Lipid Rafts per LUV

Size of the lipid raft is temperature-dependent. Pathak and London estimated that size of lipid raft changes form ~150 Å at 10°C to less than 40 Å at 45°C (*116*). For our calculations we used average radius of 100 Å (10 nm).

We assumed that the raft shape is circular and all have similar size, therefore

Area of lipid raft = $\pi \cdot r^2 = \pi * (10)^2 = 314$ nm^2;

Max possible number of rafts/LUV = LUV surface area / Area of raft = 400;

Rafts are expected to occupy approximately 10-40% of membrane (*147*), (*148*), (*149*) resulting in 20 – 75 rafts per LUV.

Appendix H Estimation of the Length of Lipid Raft Boundary

Assuming that lipid raft has a circular shape, the length of the boundary for one lipid raft is

$C = 2 \times \pi \times r = 62.8$ nm;

Using an average number of lipid rafts per LUV (50) we can estimate the total lipid raft boundary per one LUV as follows:

Total raft boundary = 50*C = 3140 nm = 3 μm;

Taking into account that lipidated peptide has 7 amino acids (0.8 nm per one amino acid), an estimated length of the peptidic part = 7 nm.

In this simple estimate we assumed that lipids anchor the peptide at the boundary and the peptide chain helps to shield hydrophobic mismatch of the thickness of raft and disordered phase from solvent.

Dividing the length of the boundary for one lipid raft by peptide length: 62.8/7 = maximum of 9 peptide molecules can possibly fit on lipid raft boundary;

0.1% peptide corresponds to 75 molecules; therefore 8 rafts (11% of the total boundary) will be occupied;

0.5% peptide = 375 molecules, therefore 42 rafts (85% of the total boundary) will be occupied.

Appendix F Calculation of the Protein Surface Density for Ras-LUV Complex

Calculation of total number of lipids per LUV followed Hutchinson et al. (*150*):

$$Ntotal = \frac{4\pi(d/2)^2 + 4\pi(d/2 - h)^2}{a}$$

where *d* is a diameter of LUV (known from an extruder membrane pore size), *h* is a thickness of the bilayer (~ 5nm), *a* is the lipid head group area (*a* for POPC is ~0.71 nm^2 (*146, 151*).

If *d* = 200 nm, then Ntot = 3.4×10^5 lipids;

Total number of LUVs per milliliter of liposome solution was calculated using the following equation:

$$N_{lipo} = \frac{M_{lipid} \times N_a}{N_{tot} \times 1000}$$

where *Na* is the Avogado Number (6.02×10^{23}), M_{lipid} is molar concentration of the lipid, N_{tot} is total number of lipids per LUV;

Molar concentration of lipid was determined using Rhod-DOPE absorbance in eluted fractions ($A_{Rhod\text{-}DOPE} = 0.054$, $C_{Rhod\text{-}DOPE} = 0.054/88{,}000 = 0.6$ μM).

Total lipid concentration = 0.6 μM / 0.02 = 30 μM;

Nlipo = 5.4×10^{13} liposomes/LUV

Number of lipidated Ras molecules was estimated using Bradford assay:

	Concentration measured, μ g/ml	Concentration, mol/L	Surface density, mol/ μ m^2,
homogeneous LUV sample	9 ±2	4.5×10^{-7}	40,000
raft LUV sample	3±2	1.5×10^{-7}	13,000

Appendix G Sequence alignment of *H*- and *N*-Ras isoforms

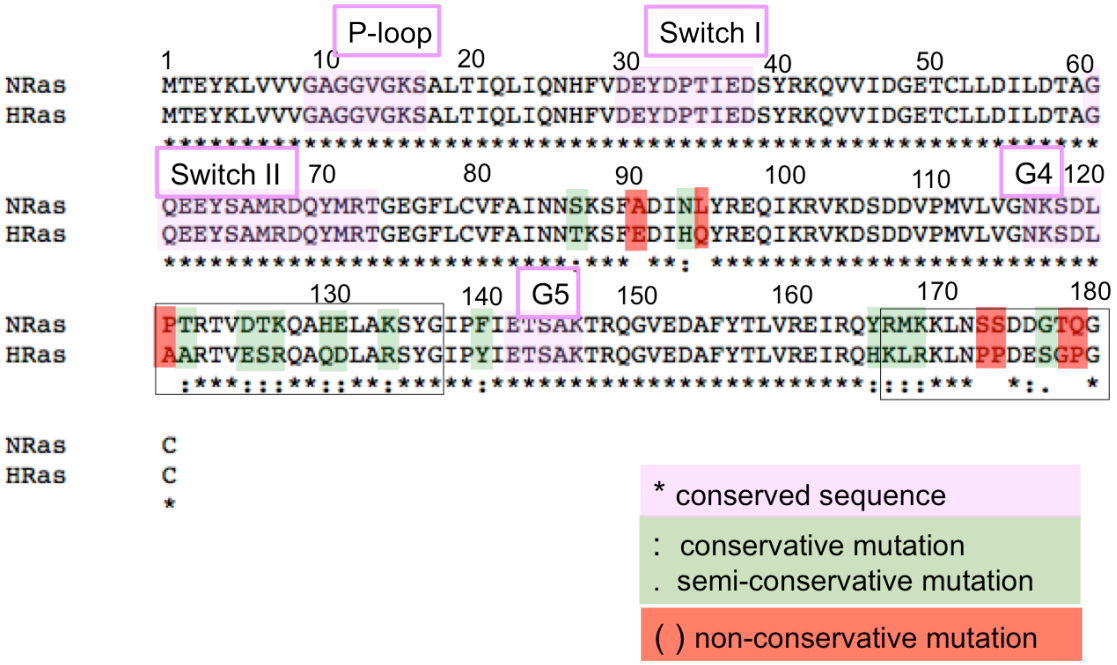

Catalytic domain represented by residues 1-166 and mostly conserved. Hypervariable region, which closely interact with membrane is different between all three isoforms (residues 167-188/189, black box). Sequence corresponding to helix α4 (black box, residues 121-137) is the second least conserved extended sequence stretch after the HVR.